Organic semiconductors, lead halide perovskites, and quantum dots: Interface engineering of multi-component, solution-processible semiconductors for optoelectronic device applications

---

A Dissertation presented to

the faculty of the School of Engineering and Applied Science and Physics

in partial fulfillment of the requirements for the degree of a

Doctor of Philosophy

in Chemical Engineering from the University of Virginia

Written by

Ashley M. Conley

Under the guidance of Dr. Joshua Choi and Dr. Gaurav Giri

November 30th, 2022

Abstract

Semiconductors are ubiquitous in modern life, existing as transistors in electronics, light emitting diodes in visual displays, and solar cells on houses and company rooftops. Scientists continue to push the limits of material properties to ameliorate the most technologically challenging problems facing humanity, such as climate change, the breakdown of Moore's law, and the continued need for affordable, widely-available technology for our expanding population. At the heart of semiconductor technology is the necessity to deeply understand and control material-dependent structure-property relationships. However, single-component materials can have trade-offs or intrinsic limitations that hinder further advancement. But with a plethora of semiconductors available, increasingly-clever design of multi-component, hybrid materials with complementary properties have proven instrumental in overcoming intrinsic limitations of single-phase materials.

In this work, we utilize organic semiconductors, three-dimensional perovskites, two-dimensional perovskites, and quantum dots to exploit their unique properties to enhance structure-property relationships. In this work, we first combine organic semiconductors with two-dimensional perovskites, and second, we incorporate quantum dot dopants in three-dimensional perovskites. In the first pairing, we leveraged the structural tunability of two-dimensional perovskites to finely control the crystal structure of a small molecule organic semiconductor, 6,13-bis(triisopropylsilylethynyl)pentacene (TIPS-pentacene), whose propensity to adopt multiple molecular packing motifs with highly-contrasting optoelectronic properties has been an ongoing challenge. Next, we studied singlet fission, an exciton multiplication process with applications in organic photovoltaics, of the perovskite-templated TIPS-pentacene structures to show that a key exciton separation process is enhanced by a factor greater than two when molecular packing

structural disorder is reduced. Finally, modeling of TIPS-pentacene/perovskite interfacial structures revealed that perovskite surfaces allow for closer packing of TIPS-pentacene molecules. In the second pairing, we doped three-dimensional perovskite with lead sulfide quantum dots to utilize the outstanding charge carrier mobility of three-dimensional perovskites with the quantum-confined, narrow band emission of the quantum dots for its application as scintillation X-ray detectors. We show that the light yield, a key performance metric for scintillators, of quantum-dot-doped perovskites is substantially improved compared to that reported for single-phase perovskites. These works motivate the interface engineering of hybrid semiconductor material systems to control structural-optoelectronic properties.

Table of Contents

Abbreviations key

Small molecule	SMol
Organic semiconductor	OSC
6,13-bis(triisopropylsilylethynyl)pentacene	TIPS-pentacene
Two-dimensional	2D
Three-dimensional	3D
Quantum dot	QD
Singlet fission	SF
Self-assembled monolayers	SAMs
Photoluminescence	PL
Transient absorption	TA
Species-associated differential spectra	SADS
Molecular dynamics	MD
Grazing incidence X-ray diffraction	GIXD
Atomic number	Z
Mega-electron volt	MeV
Photomultiplier tube	PMT
Near infrared	NIR
Lead halide perovskite	LHP
Cesium lead chloride	$CsPbCl_3$
Methylammonium lead bromide	$MAPbBr_3$
Valence band	VB
Conduction band	CB

Acknowledgements

I'd like to thank my advisors, Dr. Joshua Choi and Dr. Gaurav Giri, for their guidance, kindness, freedom, and support. During my time at University of Virginia, I wanted to try many things, such as service roles for the labs, for the department, and outreach. While research is arguably most important to a PhD student, they supported all of my endeavors, even when they took time away from lab work. Without the opportunities to pursue other interests, I couldn't have kept up my enthusiasm for research. I also greatly appreciate their efforts to let me to work at my own pace and in my own way, while also being readily available when I needed help. I feel very lucky to have had two fantastic advisors. I would also like to extend thanks to my committee members, Dr. Bill Epling, Dr. Chris Paolucci, and Dr. Seung-Hun Lee, for their guidance and time during this pivotal moment in my life. Finally, a special thank you to Dr. Paolucci for all the impromptu mentoring for my projects and dissertation as well as for a great collaboration.

Next, I have to thank members of the Choi and Giri groups. First, my senior graduate students/mentors, Alex Chen, Stephanie Guthrie, Luke Huelsenbeck, Matt Alpert, were incredibly kind, patient, hard-working and generous with their time while they taught me everything about the lab. Next, my peers, Steve Jung, Natalie Smith, and Prince Verma, Kate Dagnall, and Lucy Yoon, were so fun to work with. I couldn't have been surrounded with a better group of people while we all figured out how to survive in the lab, give presentations, and, you know, complain about our struggles. I have to give a special shout out to Steve, who was literally my rock, the first person I shared my joy and struggles with, and who I will miss dancing with in the lab and making absolutely ridiculous videos with (plus pranks and drama). Finally, I am so thankful for those who came after I started to get the hang of things, Ephraiem Sarabamoun, Meagan Phister, Sammy Fieser, Ankit Dhakal, Randi Herath, and YK Choi. I can't express how inspiring it has been watching them grow into independent researchers and take the reins of their projects. I have cherished our time together, and while I am sad to close this chapter, I am confident they will do great things along their own PhD journeys. Last but not least, I enjoyed working with the brilliant

Grayson Johnson, the oracle if you will, who had the best friendly insult jokes and helped me aspire to get my PhD just so he can no longer hold it over my head that he has one and I don't. In all, the people who have come through the Giri and Choi research labs are intelligent, kind, wonderful people that I will miss greatly.

I'd like to thank all of the graduate students in the chemical engineering department for being awesome, approachable, hilarious people that made coming to work fun. Some of my favorite memories are from our themed happy hours, the progressive's parties, Friendsgivings, secret Santas, and more. Now, for some special shoutouts. Patrick McCormick was a great friend, and my go-to drinking buddy at happy hours, social events, holidays, and more. Hosting in-person happy hours with Yiran Wang was a great experience as we picked out food, accidently didn't order enough potstickers and freaked out, carefully selected great beer. I had a blast working with Mark Banoon to create the best virtual happy hours during COVID era, where we converted the department into cartoons or played games on zoom. Rhea Braun was an excellent partner in (safety) crime when we served on the chemical engineering department safety committee to make sure the graduate student perspective was being represented well and included in safety objectives.

Let's be honest here. I wouldn't have been able to navigate this whole PhD thing without the one and only, Jennifer Davis. She is an organized, cheerful, hardworking person, and I wouldn't have survived without her. She was always kind and easy to talk to, as someone who works in the front office but also as a friend. I will miss stopping by unannounced to catch up and chit chat.

And I wouldn't have made it without my close friends. Silvia is a real one, let me tell you, and she was the first person I turned to for celebrations or for when something went wrong or just because. I couldn't have made it through without our venting sessions, our trips to Nashville, our complaints about this whole life thing, or our wine/baking/parties. Then there's Alesha Hahn, my hardworking, cut the crap best friend. Even all the way in Cali, she helped me through difficult life experiences before and during graduate school and has been an inspiration to me for as long as I can remember. My friend Patricia Capone was my undergraduate research buddy, my line dancing buddy, and still a close friend even after she worked her tail off in medical school. Talking with her through the hardships was invaluable and I am continually inspired by her grit, perseverance,

and kindness. Then there's the group of friends that came out of nowhere and changed my life forever, Shawn, Beverly, Will, Catie, Gabby, Macee, Vadar, Jess, Morgan, Steve (Nate), Hudson, Peter, Tom, Nathan, and others. Words can't describe how wonderful, bright, and beautiful these people are, both inside and outside, and how deeply blessed I feel to have them in my lives. The memories we have made dancing, laughing, and being silly as heck these last three years are so fun that it almost feels unfair. Last but not least, Chris and Shael Welton. Escaping Charlottesville to hang out in Ruckersville to play corn hole and pool, eat fantastic food prepared by the Best Chef Ever (Shael) all while drinking fancy cocktails, celebrating holidays together has been absolutely awesome. We started off as COVID friends, and from our first hangout, our friendship grew so fast that it feels like we have known each other forever. I couldn't have made it through without their support, heart-to-heart conversations, and advice.

Now, I have to thank my awesome, supportive, understanding family. Over the years, I have realized how lucky I am to have them. We Conleys are stubborn, we fight and make up, we fight hard for our friends, are loyal to the end, and we love each other deeply. I would like to especially thank my mom, Patricia Conley-Winston and my brother, Jonathon Conley. While I was here at UVA, they have cheered me on every step of the way, from my passing quals to watching my proposal on zoom to supporting me during my defense. I faced many challenges during my time in Virginia, from hardships in graduate school, to personal relationships, to emotionally difficult life changes, and then finally through my transition out of graduate school and into the workforce. I would not been able to make it through without their continued love and support as well as our visits and memory making in both Ohio and Virginia. And I don't know what I would do without them.

Gladys Hawkins was my grandmother. She wasn't here for my PhD years; however, I could not have reached this far if it weren't for her. She propped me up from a very young age, always looking out for me and giving me what I needed. College wasn't a popular choice in my family, and I didn't even know what college was until my teachers started asking about it my junior year. But Gladys saw that I was made for college, that I thrived in school, and that I was different. I may not have been skilled with my hands, but I could do math and I worked hard. I was almost locked

out of college for financial reasons, but that sure as heck was not going to happen on her watch. Unbeknownst to me, she had been scheming on my behalf and she helped me make it to my first year of college. We lost Grandma Gladys before the end of my first year, but her influence lives on. I wrote a poem about her after her passing, which has aged well given this pivotal point in my life. I've held onto the fire to succeed that started in high school, that burned brighter after her passing, and has followed me all the way up to get this PhD. Since I'm afforded some space in this document for my own interests, I'd like to publish it here.

I wouldn't be who I am today / if she wouldn't have been there to show me the way / She kept my head high, didn't let me let go / Because of her I won't stop until I reach the sky / She said "you've got what it takes, I know you can do it" / She gave me that push / now I'm going to go through with it / I wouldn't be who I am today, if it wasn't for the beautiful and loving Gladys Mae.

I'd also like to extend thanks to my two sweet pets, my dog Rutherford and my cat Ralphie. Rutherford has been especially supportive in times of great stress. When I feel overwhelmed, he swoops into his emotional support dog mode with his ears back, eyes focused, and his little behind right in my lap. Even little Ralphie seems to know when to give a little bit of support.

Finally, Chris Henson, the kindest, funniest, most generous, brilliant, and hardworking person I have ever met. He has propped me up, protected me, been my fiercest fighter, my loudest cheerleader (what goes around…), and has been an incredibly loving companion. He has seen me at my absolute best and complete worst, and he has loved me unconditionally all the same. He knows me inside and out like the back of his hand and somehow, he is quite literally my biggest fan, which means more to me than he knows. Getting a PhD is hard and it can take much sacrifice. Countless times I've floundered, felt like I was never going to make it through, had a few breakdowns, had my worldview flipped upside down, gone through a career path crisis, health scares/changes, had life-changing experiences, traveled to new places, and so much more. I experienced physical ramifications of extreme stress and overworking, and when I needed help, he was always right there. Thanks to him, I never had to face the challenges and hardships alone. Nothing that I have accomplished would be worth it without him right here beside me. I attribute my success and perseverance to the love of my life, Chris Henson.

About the author

Ashley Conley went to high school at Thomas Worthington, where she was a cheerleader and a clarinet player in the ensemble band. At age 16, she began working at Bob Evans five days a week to start saving money for college. Her favorite subject had always been Math, but after taking AP chemistry, she was motivated to major in Chemistry in college.

Ashley went to University of Tampa her first year of college, then transferred to Columbus State Community College her second year before finally settling at The Ohio State University. She continued her major in Chemistry and minored in Mathematics. However, upon completing the requirements for the mathematics minor, she felt deeply sad to discontinue math courses. So, she decided to follow the curriculum to get a Dual degree, one in Chemistry and one in Applied Mathematics. During her time in college, she developed interests in renewable energy, sustainability, health, and nutrition.

Ashley continued to work through college to support herself and finance her schooling. She worked at Bob Evans for a total of 7 years and worked at Gallo's Taproom for 1 year. While being a server was difficult, tedious, exhausting work, Ashley enjoyed every moment of the breakfast and dinner rushes. She willingly took all the party tables and had regular customers that requested to sit in her section. She worked hard and fast to turn over tables as efficiently as possible without sacrificing service quality. Here, she learned patience, kindness, and the value in staying humble. In addition to being a waitress, she took on a second job as a teaching assistant for the mathematics department at Ohio State during her senior years. She taught college pre-algebra for one semester and precalculus for two semesters. She wrote lesson plans, made and graded quizzes, and taught on a chalkboard for two classes of 30 students twice a week. Here, she discovered her love for teaching and mentoring. As evidenced by her performance reviews from students, her enthusiasm and love for mathematics was so tangible that it rubbed off on her students who historically hated math. As someone who struggled herself in her coursework, Ashley relished the opportunity to provide the kind, constructive feedback that her students needed to succeed in her classes. Teaching at The Ohio State University is one of her most cherished experiences.

Ashley did research for the Harris-Paul research groups in the Chemistry department with many other undergraduate researchers. Here, she was challenged to be independent right from the beginning, as she didn't have an official mentor to guide her. While this was a hardship for her,

she learned to be resilient and to press forward in the face of adversity and uncertainty. She presented her work at the Denman research forum, and after presenting to an employee from Battelle, she was offered an internship. Sadly, it paid half as much as her income waiting tables, and she could not afford to take it. However, this boosted her confidence in her abilities and she became emboldened in lab to explore and try new things. Through her lab work and presentations, she discovered her love for the nitty gritty nature of research and deep understanding of scientific principles.

Ashley then pursued graduate school, which was a perfect fit for her. Ashley was looking for something new to study to expand her horizons outside of her fundamental science degrees in Chemistry and Mathematics. She applied to engineering programs in hopes she could do more application-based research. She decided to go to the University of Virginia, where she joined the research groups of Gaurav Giri and Joshua Choi to research a plethora of semiconductors and elucidate their structure-property relationships. Ashley had her sights set on an academic career route starting at 16 years old when she started saving for college, and 13 years later, she graduated with a PhD in Chemical Engineering. A dream that her younger self never thought possible, Ashley will be starting her position at First Solar as a Development Engineer doing research and development of cadmium telluride solar cells.

Chapter 1: Introduction to Semiconductor Materials

1.1 Introduction to Organic Semiconductors

1.1.1 Small molecule organic semiconductors

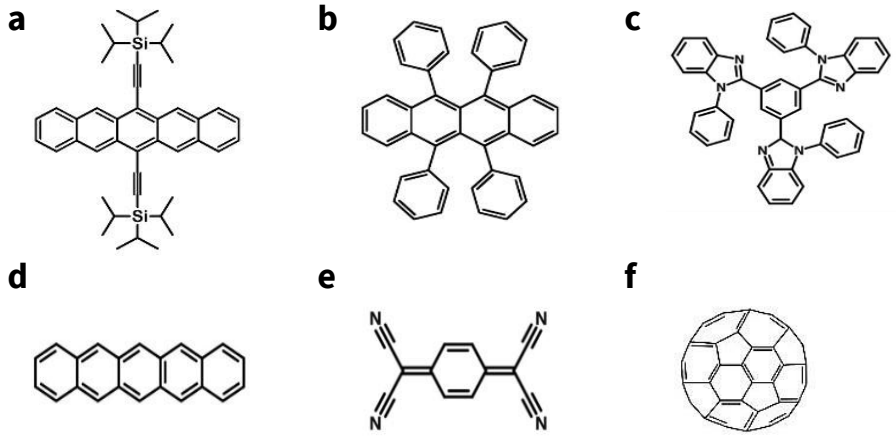

Figure 1.1. Examples of small molecule organic semiconductors. **(a)** TIPS-pentacene **(b)** Rubrene **(c)** TPBi: 2,2',2''-(1,3,5-Benzinetriyl)-tris(1-phenyl-1-H-benzimidazole) **(d)** pentacene **(e)** TCNQ: 7,7,8,8-Tetracyanoquinodimethane **(f)** C_{60}: (C60-Ih)[5,6]fullerene.

A collective interest across disciplines for the use of organic semiconductors in electronic and optoelectronic devices began in the 1990s.[1–3] Pentacene, C_{60}, rubrene, and other benchmark OSCs have charge transport capabilities competitive with amorphous and polycrystalline silicon[1,4–9] while also allowing for the possibility for mechanically flexible and lightweight devices. Popular and high-performing acene-based and oligomer small molecule (SMol) organic semiconductors (OSCs) are shown in **Fig. 1.1**. Charge carriers hop from molecule-to-molecule through π-conjugated systems and π-π stacking. Many OSCs are solution processible, which means that they can be fabricated continuously on manufacturing scales through roll-to-roll thin film fabrication methods. Solution-processable OSCs, such as 6,13-bis(triisopropylsilylethynyl) pentacene (TIPS-pentacene), are desirable because thin films are deposited from solution at low

temperatures. Solution-processable OSCs are recognized in academia and industry as particularly valuable for their ability to be used for high-throughput, large-area fabrication, and thus inexpensive mass production.[10] Using solution processing methods, lightweight, flexible optoelectronic devices such as display technologies, wearable electronics, and bioelectronics can be realized.[11,12]

1.1.2 Applications of organic semiconductors

Organic semiconductors have been widely studied for their use in electronic and optoelectronic devices such as organic light emitting diodes, field effect transistors, and solar cells.[11,13–25] Organic semiconductors are advantageous over conventional silicon-based devices in applications that require mechanical flexibility and/or large area devices.[26] Organic semiconductor

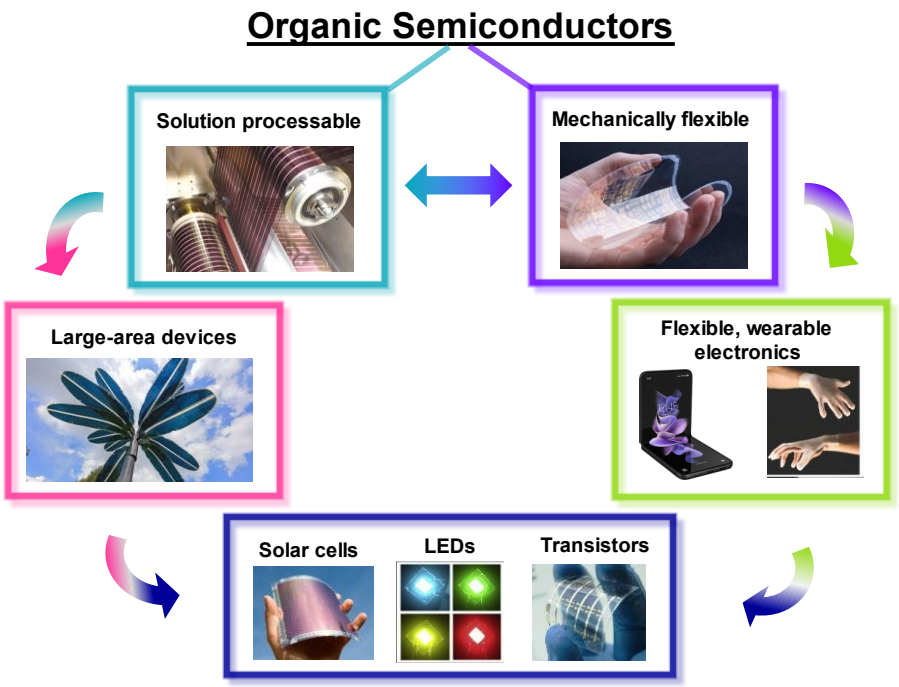

Figure 1.2. Schematic of the two main beneficial properties of organic semiconductors, solution processibility and mechanical flexibility, with examples of device applications. [ref. 19-25].

materials entered the industrial markets with the first OLED TV from Sony in 2004,[27] with OFETs being employed in flexible OLED screen displays[28] and the creation of organic solar cells with efficiencies rivaling amorphous silicon solar cells.[29] Unlike conventional silicon solar cells, commercialized organic solar cells are adaptable to numerous surfaces and can be created in a variety of shapes for pragmatic or recreational purposes such as windows or artistic solar trees in 2015 from OPVIUS.[20] Even with the commercialization of organic semiconductor materials, companies and countries around the world continue to push the limits of these technologies in terms of efficiency and performance; according to a research report in April 2020 from the Advance Market Analytics of the Global Organic Solar Cells Market, the market is predicted to double in size due to the benefits of organic solar cells and the shift in demand towards clean energy.[30]

1.1.3 Charge transport mechanism

Charge transport occurs via intermolecular interactions via out-of-plane p-orbital overlapping, called π-π stacking, with neighboring molecules. Face-to-face stacking occurs when there is direct π-π stacking, as shown in **Fig. 1.3a**. However, π-π stacking can still occur with slight intermolecular offsetting, which is referred to as slip-stacking and is shown in **Fig. 1.3b**. In the solid state, these molecules are organized in 3D space in a crystalline structure. Depending on the long-range molecular ordering, different π-π stacking configurations are possible. Three example configurations for an acene-based molecule composed of more than one ring is shown in **Fig. 1.3c-e**. Face-to-edge stacking results in minimal p-orbital overlap, and thus charge transport is severely hindered. In a lamellar stacking configuration, molecules exhibit face-to-face π-stacking which results in one-dimensional charge transport. Finally, a brick-wall stacking configuration which

includes a convolution of face-to-face and slipped π-stacking allows for two-dimensional transport.

1.1.4 Challenges

As with all materials, small molecule organic semiconductors come with their own inherent limitations and challenges. Organic semiconductor molecules organize in the solid state according to weak Van der Waals forces rather than a more stronger bonding motif such as covalent bonding. A direct consequence of this weak bonding is that many SMol-OSCs adopt multiple molecular packing motifs, known as polymorphs, which are similar in energy but differ in their charge transport capabilities by orders of magnitude.[31–33] To further add complexity to these systems, the molecular packing and macroscopic properties of the final solid-state film is acutely sensitive to

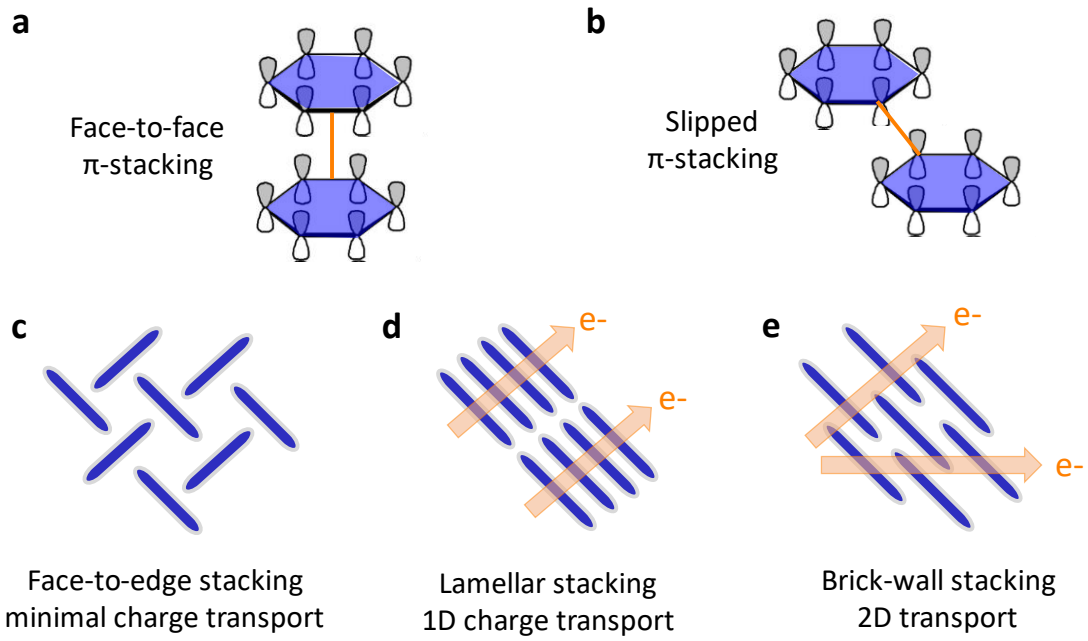

Figure 1.3. Schematic of out-of-plane p-orbital overlapping with **a)** face-to-face and **b)** slipped stacking. The depictions of different molecular packing motifs with **c)** face-to-edge, **d)** lamellar, and **e)** brick-wall stacking and their respective directional charge transport.

the deposition method, solvent, concentration, substrate roughness, substrate functionalization, temperature, and other processing parameters.[9,12,31,34–40] Depending on the stability of the deposited molecular packing structure, this molecular packing may change over time or with changing temperature if a more thermodynamically stable structure is available. Polymorphism may be viewed as an inherent disadvantage yet can also be another handle of manipulation for the optimization of devices. In both respects, controlling the polymorphism of organic semiconductors is essential to achieving consistent, reliable performances.

1.2 Introduction to Lead Halide Perovskites

1.2.1 Three-dimensional (3D) perovskites

Lead halide perovskites are a class of materials with the general formula ABX_3, where A is a small organic cation, B is divalent metal, and X is a halide. Perovskites are of great interest in the research community due to their exceptional optoelectronic properties with applications in solar cells, photodetectors, light emitting diodes, scintillators, and more.[41–50] The bandgap and optical properties of perovskites can be tuned via changes to its composition.[51–53] Perovskites exhibit excellent light absorption whereby all visible light is absorbed within a few hundred nanometers of material.[54] Perovskites were discovered to be defect tolerant, meaning that charge carriers exhibit long

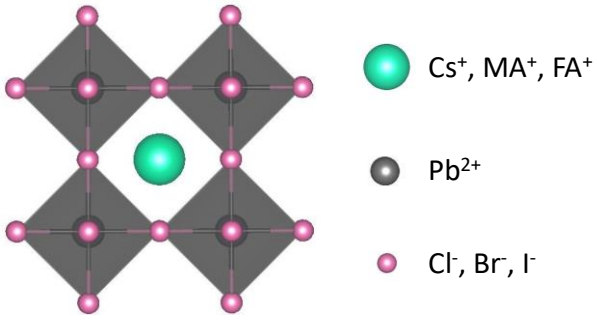

Figure 1.4. Crystal structure of three-dimensional perovskites composed of a monovalent cation such as cesium (Cs^+), methylammonium (MA^+), or formamidinium (FA^+), a divalent metal such as lead (Pb^{2+}), and a halide anion, such as chlorine (Cl^-), bromine (Br^-), or iodine (I^-).

lifetimes and diffusion lengths even in polycrystalline thin films.[55] These materials have an added benefit in that they are solution processable at room temperature, allowing for inexpensive fabrication on the order of minutes with the possibility of large area devices.[56] Since the first perovskite solar cell was made in 2009 with an efficiency of less than 4%,[57] perovskite solar cell efficiencies reached more than 25% after only a decade of intense research,[58–61] making perovskite solar cell technology directly competitive with single crystalline solar cell technology which has been studied for more than 60 years. Perovskites captured the attention of researchers around the world due to these desirable properties and high solar cell efficiencies using devices that are a fraction of the thickness of conventional silicon solar cells.

1.2.2 Two-dimensional (2D) perovskites

The dimensionality of perovskites (i.e. 3D or 2D) can be altered by incorporating a large organic cation and adjusting the stoichiometry of the perovskite precursors in solution; the result is a layered structure with a number (n) of two-dimensional sheets of inorganic corner-sharing

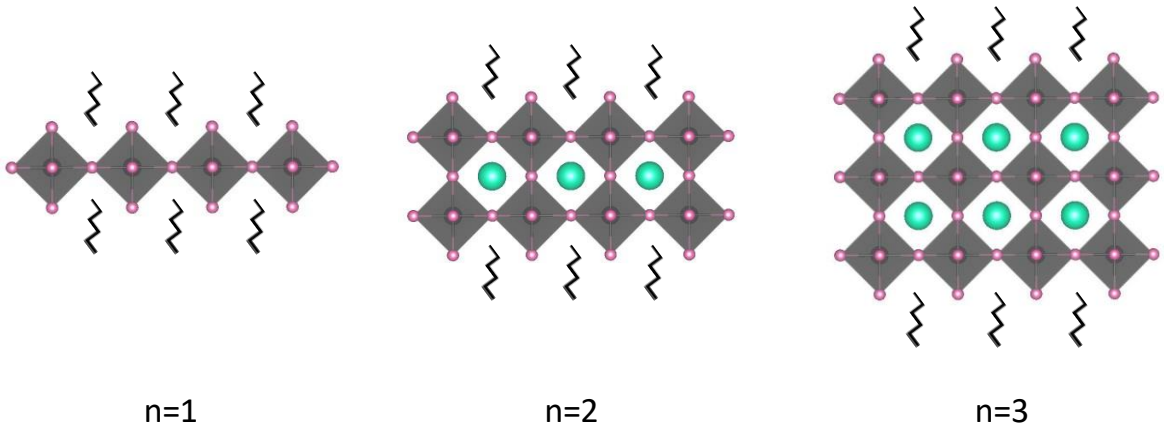

Figure 1.5. The layering structure of two-dimensional perovskites with n=1, n=2, and n=3 layers. Octahedra sheets are broken up with bulky organic cations.

octahedra separated by bulky organic cations. The structures of one-layer (n = 1), two-layer (n=2), and three-layer (n=3) two-dimensional perovskites is shown in **Fig. 1.5.**

While 3D perovskites have excellent charge transport mobilities and solar cell performance, 2D perovskites have lower charge carrier mobilities and efficiencies but have substantially enhanced stability.[62,63] The bulky organic cation incorporation provides a stable structure with resistance against moisture and light degradation. As a result, 2D perovskite solar cells have lower solar cell efficiencies but provide stable power conversion efficiencies over time.[63] Recently in 2021, Shi et al used 2D perovskites as a hydrophobic capping layer in a 3D perovskite solar cell and achieved high efficiency of 21.4%, which retained 83% of its value under conditions of 1 sun illumination, elevated temperature, and 80 percent relative humidity after 600 hours.[64] Just the next year, a method was developed for room temperature epitaxial welding of 3D and 2D perovskites,[65] sparking more interest in combining the complementary properties of the two perovskite materials.

1.3 Introduction to quantum dots

1.3.1 What is a quantum dot?

Quantum dots are nanomaterials whose physical size dimensions are of the scale 10^{-9} meters (i.e. nanometer). Semiconductors are generally characterized by an energetic bandgap arising from its composition and solid-state structure. When a semiconductor is excited by light, a coulombically-bound electron-hole pair is formed. Due to electrostatic attraction between the negatively-charged electron and positively-charged hole, they orbit around one

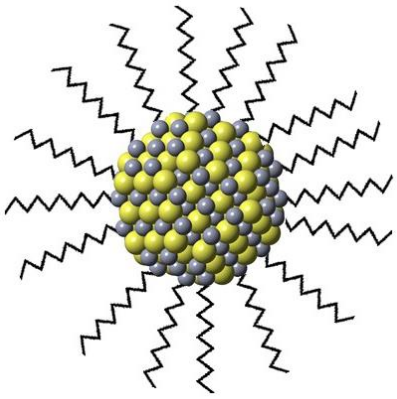

Figure 1.6. Depiction of a lead sulfide quantum dot that is capped with long chain ligands.

another within a certain diameter, called the Bohr radius, which is material-dependent. However, when the physical dimensions of the material are reduced to less than this Bohr radius, as is the case for quantum dots, semiconductor properties begin to differ from those of the bulk phase or large particles.[66] **Fig. 1.6** depicts a quantum dot with a lead sulfide core that is capped with long chain ligands. Dimensions of the quantum dot core are typically two to ten nanometers, which is approximately ten to fifty atoms. The electrons become confined to a small physical space, resulting in interesting and strange behavior leading to unexpected effects with respect to their optoelectronic properties.[66]

1.3.2 Relationship between quantum dot size, bandgap, and emission

One such property is the relationship between quantum dot size and bandgap. As the electron is confined to a small nanoparticle, the electron adopts a quantum wave function that fits within the borders of the nanoparticle volume, resulting in the formation of quantized energy levels.[66,67] As the size of the nanoparticle decreases, the lowest energy for excitation of the electron increases. As a result, the absorption of the quantum dots and emission wavelength via radiative relaxation of the electron to the ground state is dependent on the quantum dot size. The relationship between quantum dot size, bandgap (E_g), and the emission wavelength is shown in **Fig. 1.7**. As the quantum dot size increases, the bandgap decreases until the quantum dot no longer exhibits quantum confinement and approaches the bandgap of the bulk semiconductor material. The emission wavelength of the quantum dot red-shifts with increasing quantum dot size, and thus quantum dots are materials with tunable emission. Because the electron-hole pair is confined to the quantum dot core, high luminescence efficiencies have been observed with narrow emission

linewidths for monodisperse quantum dot populations with finely-controlled size distribution.[68] Once the quantum dots are formed, they can be self-assembled into three-dimensional superlattices to further manipulate material properties.[69] Quantum dots have been employed in a variety of devices, such as lasers, solar cells, transistors, and light emitting diodes.[70–74]

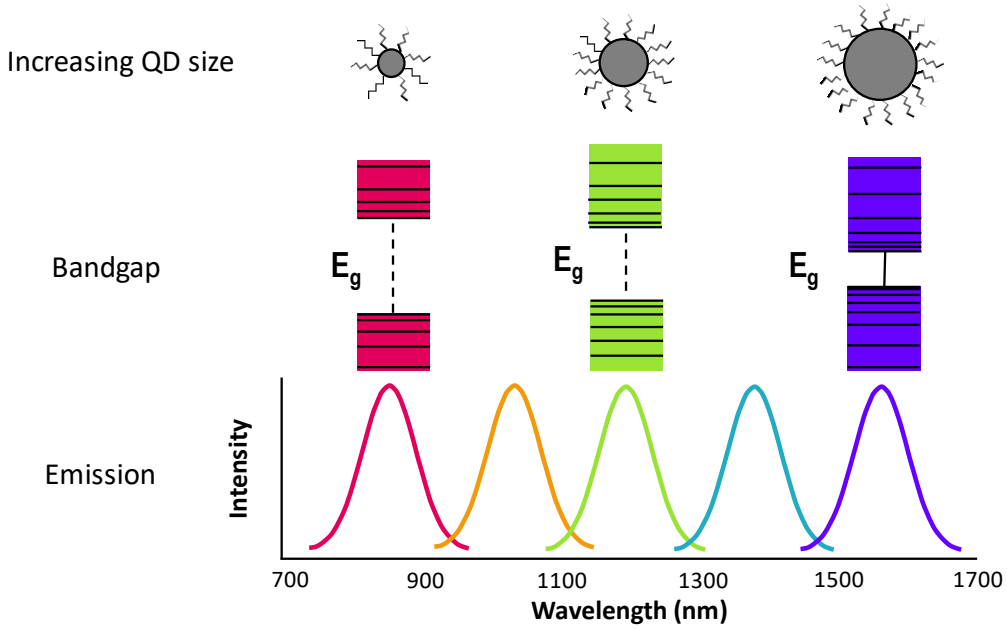

Figure 1.7. Schematic showing the relationship between the lead sulfide quantum dot size, bandgap (E_g), and the emission wavelength.

1.4 Combining different classes of semiconductors to alter material properties

1.4.1 The usefulness of designing hybrid materials

As discussed above, it is clear that single phase materials of organic semiconductors, three-dimensional perovskites, two-dimensional perovskites, and quantum dots all have unique structure-property relationships. Organic semiconductor properties are affected by structural variations that may be introduced during fabrication or arising from processing conditions.

Perovskite optical properties are more acutely sensitive to the composition itself, such as which or what blend of halides are incorporated in the structure or the choice or blend of organic cations. When the dimensionality of perovskites is reduced to a 2D structure, quantum confinement of the electron-hole pair further alters the optoelectronic properties. For quantum dots, the optical properties can be tuned based on the size of the semiconductor core and surface termination.

The focus of this works is not to optimize properties of each of these materials; rather, we aim to combine different materials to take advantage of intrinsic properties of each or to use one material to alter the properties of another. The careful design of hybrid materials with complementary properties has proven instrumental in overcoming shortcomings of single-phase materials. Quantum dots have been combined with perovskite materials to capitalize on charge mobilities of perovskites with the narrow, quantum-confined emission of quantum dots.[75] These perovskite-quantum dot material systems have been applied to infrared emitters[76] and solar cells.[71,77] The charge carrier ability of quantum dots is seriously hindered when capped with saturated carbon-based long chain ligands, such as lead oleate, and so researchers formulated methods to cap the quantum dot with perovskites, which increases the charge transport mobilities and allows for the application of quantum dots in solar cells.[78] Perovskites have also been used as capping agents for quantum dots to increase their stability in solution and ambient conditions so that the quantum dots can be stored as inks for more than 20 months and still be used in optoelectronic devices.[79] Perovskite materials have been fabricated into quantum dots themselves.[80,81] Even more striking, small molecule organic semiconductors have been covalently bound to perovskite quantum dots to pass charge carriers from the perovskite to the organic semiconductor to undergo singlet fission, an exciton multiplication process.[82] The combination of

complex material systems provides endless opportunities to optimize, manipulate, overcome, and extrapolate semiconductor material properties.

1.4.2 Dissertation Overview

In this piece, we combine organic semiconductors with two-dimensional perovskites, and then three-dimensional perovskites with atomic and quantum dot dopants. In the first pairing, we demonstrate that the structural tunability of two-dimensional perovskites can be used to finely control the crystal structure of a small molecule organic semiconductor that is well-known for its many potential structures. We proceed to show that a key singlet fission process of the perovskite-templated organic semiconductor structures is enhanced when the overall crystalline disorder is reduced. In the next project, we dope three-dimensional perovskite with a rare-Earth metal and show that the light emission produced from X-ray excitation of the polycrystalline composite material is competitive with conventional materials without the need for single crystal processing methods. Lastly, we doped three-dimensional perovskites with quantum dots to utilize the outstanding charge carrier mobility of perovskite with the quantum-confined, narrow band emission of quantum dots to show that light emission produced from X-ray excitation is greatly enhanced compared to that reported for single-phase perovskites.

1.5 References

(1) D. J. Gundlach; Y. Y. Lin; T. N. Jackson; S. F. Nelson; D. G. Schlom. Pentacene Organic Thin-Film Transistors-Molecular Ordering and Mobility. *IEEE Electron Device Letters* **1997**, *18* (3), 87–89. https://doi.org/10.1109/55.556089.

(2) Garnier, F.; Horowitz, G.; Peng, X.; Fichou, D. An All-Organic "soft" Thin Film Transistor with Very High Carrier Mobility. *Advanced Materials* **1990**, *2* (12), 592–594. https://doi.org/10.1002/adma.19900021207.

(3) Horowitz, G. Organic Semiconductors for New Electronic Devices. *Advanced Materials* **1990**, *2* (6–7), 287–292. https://doi.org/10.1002/adma.19900020604.

(4) Takeya, J.; Yamagishi, M.; Tominari, Y.; Hirahara, R.; Nakazawa, Y.; Nishikawa, T.; Kawase, T.; Shimoda, T.; Ogawa, S. Very High-Mobility Organic Single-Crystal Transistors with in-Crystal Conduction Channels. *Appl. Phys. Lett.* **2007**, *90* (10), 102120. https://doi.org/10.1063/1.2711393.

(5) Kelley, T. W.; Boardman, L. D.; Dunbar, T. D.; Muyres, D. V.; Pellerite, M. J.; Smith, T. P. High-Performance OTFTs Using Surface-Modified Alumina Dielectrics. *J. Phys. Chem. B* **2003**, *107* (24), 5877–5881. https://doi.org/10.1021/jp034352e.

(6) Shtein, M.; Mapel, J.; Benziger, J. B.; Forrest, S. R. Effects of Film Morphology and Gate Dielectric Surface Preparation on the Electrical Characteristics of Organic-Vapor-Phase-Deposited Pentacene Thin-Film Transistors. *Appl. Phys. Lett.* **2002**, *81* (2), 268–270. https://doi.org/10.1063/1.1491009.

(7) Li, H.; Duan, Y.; Coropceanu, V.; Bredas, J.-L. Electronic Structure of the Pentacene–Gold Interface: A Density-Functional Theory Study. *Organic Electronics* **2009**, *10* (8), 1571–1578. https://doi.org/10.1016/j.orgel.2009.09.003.

(8) Zhu, X.; Zhang, X.; Huang, L.; Wang, Z.; Chi, L. Improving the Performance of TIPS-Pentacene Thin Film Transistors via Interface Modification. *Chemical Research in Chinese Universities* **2018**, *34* (1), 151–154. https://doi.org/10.1007/s40242-017-7122-x.

(9) Virkar, A.; Mannsfeld, S.; Oh, J. H.; Toney, M. F.; Tan, Y. H.; Liu, G.; Scott, J. C.; Miller, R.; Bao, Z. The Role of OTS Density on Pentacene and C60 Nucleation, Thin Film Growth, and Transistor Performance. *Advanced Functional Materials* **2009**, *19* (12), 1962–1970. https://doi.org/10.1002/adfm.200801727.

(10) Sheats, J. R. Manufacturing and Commercialization Issues in Organic Electronics. *Journal of Materials Research* **2004**, *19* (7), 1974–1989. https://doi.org/10.1557/JMR.2004.0275.

(11) White, M. S.; Kaltenbrunner, M.; Głowacki, E. D.; Gutnichenko, K.; Kettlgruber, G.; Graz, I.; Aazou, S.; Ulbricht, C.; Egbe, D. A. M.; Miron, M. C.; Major, Z.; Scharber, M. C.; Sekitani, T.; Someya, T.; Bauer, S.; Sariciftci, N. S. Ultrathin, Highly Flexible and Stretchable PLEDs. *Nature Photonics* **2013**, *7* (10), 811–816. https://doi.org/10.1038/nphoton.2013.188.

(12) Giri, G.; Li, R.; Smilgies, D.-M.; Li, E. Q.; Diao, Y.; Lenn, K. M.; Chiu, M.; Lin, D. W.; Allen, R.; Reinspach, J.; Mannsfeld, S. C. B.; Thoroddsen, S. T.; Clancy, P.; Bao, Z.; Amassian, A. One-Dimensional Self-Confinement Promotes Polymorph Selection in Large-Area Organic Semiconductor Thin Films. *Nat Commun* **2014**, *5*, 3573. https://doi.org/10.1038/ncomms4573.

(13) Sirringhaus, H. 25th Anniversary Article: Organic Field-Effect Transistors: The Path Beyond Amorphous Silicon. *Advanced Materials* **2014**, *26* (9), 1319–1335. https://doi.org/10.1002/adma.201304346.

(14) Arias, A. C.; MacKenzie, J. D.; McCulloch, I.; Rivnay, J.; Salleo, A. Materials and Applications for Large Area Electronics: Solution-Based Approaches. *Chem. Rev.* **2010**, *110* (1), 3–24. https://doi.org/10.1021/cr900150b.

(15) Li, Y.; Ji, D.; Liu, J.; Yao, Y.; Fu, X.; Zhu, W.; Xu, C.; Dong, H.; Li, J.; Hu, W. Quick Fabrication of Large-Area Organic Semiconductor Single Crystal Arrays with a Rapid Annealing Self-Solution-Shearing Method. *Scientific Reports* **2015**, *5* (1), 13195. https://doi.org/10.1038/srep13195.

(16) Verreet, B.; Heremans, P.; Stesmans, A.; Rand, B. P. Microcrystalline Organic Thin-Film Solar Cells. *Advanced Materials* **2013**, *25* (38), 5504–5507. https://doi.org/10.1002/adma.201301643.

(17) Lloyd, M. T.; Anthony, J. E.; Malliaras, G. G. Photovoltaics from Soluble Small Molecules. *Materials Today* **2007**, *10* (11), 34–41. https://doi.org/10.1016/S1369-7021(07)70277-8.

(18) Hasegawa, T.; Takeya, J. Organic Field-Effect Transistors Using Single Crystals. *Science and Technology of Advanced Materials* **2009**, *10* (2), 024314. https://doi.org/10.1088/1468-6996/10/2/024314.

(19) Williams, M. Printed Organic Solar Cells and LED.

(20) OPVIUS Energizing Surfaces. http://www.opvius.com/.

(21) Cross, David. J. Analyzing the Effectiveness of Flexible Solar Cells.

(22) Miao, Y.; Yin, M. Recent Progress on Organic Light-Emitting Diodes with Phosphorescent Ultrathin (<1nm) Light-Emitting Layers. *iScience* **2022**, *25* (2), 103804. https://doi.org/10.1016/j.isci.2022.103804.

(23) Gorman, M. IMEC Creates Flexible Microprocessor with Organic Semiconductors -- Computational Clothing Right around the Corner.

(24) Fuentes-Hernandez/, C. Top-Gate Organic Field-Effect Transistor with Bilayer Gate Insulator. *Georgia Institute of Technology*.

(25) Muth, J. T.; Vogt, D. M.; Truby, R. L.; Mengüç, Y.; Kolesky, D. B.; Wood, R. J.; Lewis, J. A. Embedded 3D Printing of Strain Sensors within Highly Stretchable Elastomers. *Advanced Materials* **2014**, *26* (36), 6307–6312. https://doi.org/10.1002/adma.201400334.

(26) Liu, K.; Ouyang, B.; Guo, X.; Guo, Y.; Liu, Y. Advances in Flexible Organic Field-Effect Transistors and Their Applications for Flexible Electronics. *npj Flexible Electronics* **2022**, *6* (1), 1. https://doi.org/10.1038/s41528-022-00133-3.

(27) Smith, B. *OLED: A Story of Patience, Perseverance, and Innovation*; LG Electronics, 2019. https://www.lg.com/uk/lg-magazine/brand-story/the-history-of-the-oled-tv.

(28) Kymissis, I. OFET Applications. In *Organic Field Effect Transistors: Theory, Fabrication and Characterization*; Kymissis, I., Ed.; Springer US: Boston, MA, 2009; pp 1–6. https://doi.org/10.1007/978-0-387-92134-1_7.

(29) Zhao, W.; Li, S.; Yao, H.; Zhang, S.; Zhang, Y.; Yang, B.; Hou, J. Molecular Optimization Enables over 13% Efficiency in Organic Solar Cells. *J. Am. Chem. Soc.* **2017**, *139* (21), 7148–7151. https://doi.org/10.1021/jacs.7b02677.

(30) Advance Market Analytics. *Organic Solar Cells Market Is Expected to Double Its Market Size in Upcoing Years : Dyesol, Heliatek, SIgma-Aldrich*; Press Release; 2020. https://www.marketwatch.com/press-release/organic-solar-cells-market-is-expected-to-double-its-market-size-in-upcoming-years-dyesol-heliatek-sigma-aldrich-2020-04-21?mod=mw_quote_news (accessed 2020-06-03).

(31) Diao, Y.; Lenn, K. M.; Lee, W.-Y.; Blood-Forsythe, M. A.; Xu, J.; Mao, Y.; Kim, Y.; Reinspach, J. A.; Park, S.; Aspuru-Guzik, A.; Xue, G.; Clancy, P.; Bao, Z.; Mannsfeld, S. C. B. Understanding Polymorphism in Organic Semiconductor Thin Films through Nanoconfinement. *J. Am. Chem. Soc.* **2014**, *136* (49), 17046–17057. https://doi.org/10.1021/ja507179d.

(32) D. Gupta; M. Katiyar; Deepak. Effect of Pentacene Thickness on Organic Thin Film Transistors: Role of Pentacene/Insulator Interface. In *2007 International Workshop on Physics of Semiconductor Devices*; 2007; pp 594–596. https://doi.org/10.1109/IWPSD.2007.4472587.

(33) Wang, X.; Garcia, T.; Monaco, S.; Schatschneider, B.; Marom, N. Effect of Crystal Packing on the Excitonic Properties of Rubrene Polymorphs. *CrystEngComm* **2016**, *18* (38), 7353–7362. https://doi.org/10.1039/C6CE00873A.

(34) Desiraju, G. R. Cryptic Crystallography. *Nature Materials* **2002**, *1* (2), 77–79. https://doi.org/10.1038/nmat726.

(35) Guthrie, S. M.; Smilgies, D.-M.; Giri, G. Controlling Polymorphism in Pharmaceutical Compounds Using Solution Shearing. *Crystal Growth & Design* **2018**, *18* (2), 602–606. https://doi.org/10.1021/acs.cgd.7b01686.

(36) Li, Y.; Wan, J.; Smilgies, D.-M.; Bouffard, N.; Sun, R.; Headrick, R. L. Nucleation and Strain-Stabilization during Organic Semiconductor Thin Film Deposition. *Nature Scientific Reports* **2016**, *6* (1), 32620. https://doi.org/10.1038/srep32620.

(37) Giri, G.; Park, S.; Vosgueritchian, M.; Shulaker, M. M.; Bao, Z. High-Mobility, Aligned Crystalline Domains of TIPS-Pentacene with Metastable Polymorphs Through Lateral Confinement of Crystal Growth. *Advanced Materials* **2013**, *26* (3), 487–493. https://doi.org/10.1002/adma.201302439.

(38) Giri, G.; Verploegen, E.; Mannsfeld, S. C. B.; Atahan-Evrenk, S.; Kim, D. H.; Lee, S. Y.; Becerril, H. A.; Aspuru-Guzik, A.; Toney, M. F.; Bao, Z. Tuning Charge Transport in Solution-Sheared Organic Semiconductors Using Lattice Strain. *Nature* **2011**, *480*, 504.

(39) Diao, Y.; Tee, B. C.-K.; Giri, G.; Xu, J.; Kim, D. H.; Becerril, H. A.; Stoltenberg, R. M.; Lee, T. H.; Xue, G.; Mannsfeld, S. C. B.; Bao, Z. Solution Coating of Large-Area Organic Semiconductor Thin Films with Aligned Single-Crystalline Domains. *Nature Materials* **2013**, *12*, 665.

(40) Fusella, M. A.; Schreiber, F.; Abbasi, K.; Kim, J. J.; Briseno, A. L.; Rand, B. P. Homoepitaxy of Crystalline Rubrene Thin Films. *Nano Lett.* **2017**, *17* (5), 3040–3046. https://doi.org/10.1021/acs.nanolett.7b00380.

(41) Tan, H.; Jain, A.; Voznyy, O.; Lan, X.; García de Arquer, F. P.; Fan, J. Z.; Quintero-Bermudez, R.; Yuan, M.; Zhang, B.; Zhao, Y.; Fan, F.; Li, P.; Quan, L. N.; Zhao, Y.; Lu, Z.-H.; Yang, Z.; Hoogland, S.; Sargent, E. H. Efficient and Stable Solution-Processed Planar Perovskite Solar Cells via Contact Passivation. *Science* **2017**, *355* (6326), 722. https://doi.org/10.1126/science.aai9081.

(42) Gao, X.-X.; Luo, W.; Zhang, Y.; Hu, R.; Zhang, B.; Züttel, A.; Feng, Y.; Nazeeruddin, M. K. Stable and High-Efficiency Methylammonium-Free Perovskite Solar Cells. *Advanced Materials* **2020**, *32* (9), 1905502. https://doi.org/10.1002/adma.201905502.

(43) Min, H.; Lee, D. Y.; Kim, J.; Kim, G.; Lee, K. S.; Kim, J.; Paik, M. J.; Kim, Y. K.; Kim, K. S.; Kim, M. G.; Shin, T. J.; Il Seok, S. Perovskite Solar Cells with Atomically Coherent Interlayers on SnO2 Electrodes. *Nature* **2021**, *598* (7881), 444–450. https://doi.org/10.1038/s41586-021-03964-8.

(44) Jing, H.; Peng, R.; Ma, R.-M.; He, J.; Zhou, Y.; Yang, Z.; Li, C.-Y.; Liu, Y.; Guo, X.; Zhu, Y.; Wang, D.; Su, J.; Sun, C.; Bao, W.; Wang, M. Flexible Ultrathin Single-Crystalline Perovskite Photodetector. *Nano Lett.* **2020**, *20* (10), 7144–7151. https://doi.org/10.1021/acs.nanolett.0c02468.

(45) Ahmadi, M.; Wu, T.; Hu, B. A Review on Organic–Inorganic Halide Perovskite Photodetectors: Device Engineering and Fundamental Physics. *Advanced Materials* **2017**, *29* (41), 1605242. https://doi.org/10.1002/adma.201605242.

(46) Li, C.; Wang, H.; Wang, F.; Li, T.; Xu, M.; Wang, H.; Wang, Z.; Zhan, X.; Hu, W.; Shen, L. Ultrafast and Broadband Photodetectors Based on a Perovskite/Organic Bulk Heterojunction for Large-Dynamic-Range Imaging. *Light: Science & Applications* **2020**, *9* (1), 31. https://doi.org/10.1038/s41377-020-0264-5.

(47) He, Y.; Hadar, I.; Kanatzidis, M. G. Detecting Ionizing Radiation Using Halide Perovskite Semiconductors Processed through Solution and Alternative Methods. *Nature Photonics* **2022**, *16* (1), 14–26. https://doi.org/10.1038/s41566-021-00909-5.

(48) Wang, N.; Cheng, L.; Ge, R.; Zhang, S.; Miao, Y.; Zou, W.; Yi, C.; Sun, Y.; Cao, Y.; Yang, R.; Wei, Y.; Guo, Q.; Ke, Y.; Yu, M.; Jin, Y.; Liu, Y.; Ding, Q.; Di, D.; Yang, L.; Xing, G.; Tian, H.; Jin, C.; Gao, F.; Friend, R. H.; Wang, J.; Huang, W. Perovskite Light-Emitting Diodes Based on Solution-Processed Self-Organized Multiple Quantum Wells. *Nature Photonics* **2016**, *10* (11), 699–704. https://doi.org/10.1038/nphoton.2016.185.

(49) Chen, Q.; Wu, J.; Ou, X.; Huang, B.; Almutlaq, J.; Zhumekenov, A. A.; Guan, X.; Han, S.; Liang, L.; Yi, Z.; Li, J.; Xie, X.; Wang, Y.; Li, Y.; Fan, D.; Teh, D. B. L.; All, A. H.; Mohammed, O. F.; Bakr, O. M.; Wu, T.; Bettinelli, M.; Yang, H.; Huang, W.; Liu, X. All-Inorganic Perovskite Nanocrystal Scintillators. *Nature* **2018**, *561* (7721), 88–93. https://doi.org/10.1038/s41586-018-0451-1.

(50) Dagnall, K. A.; Conley, A. M.; Yoon, L. U.; Rajeev, H. S.; Lee, S.-H.; Choi, J. J. Ytterbium-Doped Cesium Lead Chloride Perovskite as an X-Ray Scintillator with High Light Yield. *ACS Omega* **2022**, *7* (24), 20968–20974. https://doi.org/10.1021/acsomega.2c01712.

(51) Kovalenko, M. V.; Protesescu, L.; Bodnarchuk, M. I. Properties and Potential Optoelectronic Applications of Lead Halide Perovskite Nanocrystals. *Science* **2017**, *358* (6364), 745–750. https://doi.org/10.1126/science.aam7093.

(52) Gholipour, S.; Saliba, M. Chapter 1 - Bandgap Tuning and Compositional Exchange for Lead Halide Perovskite Materials. In *Characterization Techniques for Perovskite Solar Cell Materials*; Pazoki, M., Hagfeldt, A., Edvinsson, T., Eds.; Elsevier, 2020; pp 1–22. https://doi.org/10.1016/B978-0-12-814727-6.00001-3.

(53) Protesescu, L.; Yakunin, S.; Bodnarchuk, M. I.; Krieg, F.; Caputo, R.; Hendon, C. H.; Yang, R. X.; Walsh, A.; Kovalenko, M. V. Nanocrystals of Cesium Lead Halide Perovskites (CsPbX3, X = Cl, Br, and I): Novel Optoelectronic Materials Showing Bright Emission with Wide Color Gamut. *Nano Lett.* **2015**, *15* (6), 3692–3696. https://doi.org/10.1021/nl5048779.

(54) Liu, D.; Gangishetty, M. K.; Kelly, T. L. Effect of CH3NH3PbI3 Thickness on Device Efficiency in Planar Heterojunction Perovskite Solar Cells. *J. Mater. Chem. A* **2014**, *2* (46), 19873–19881. https://doi.org/10.1039/C4TA02637C.

(55) Steirer, K. X.; Schulz, P.; Teeter, G.; Stevanovic, V.; Yang, M.; Zhu, K.; Berry, J. J. Defect Tolerance in Methylammonium Lead Triiodide Perovskite. *ACS Energy Lett.* **2016**, *1* (2), 360–366. https://doi.org/10.1021/acsenergylett.6b00196.

(56) Chen, A. Z.; Shiu, M.; Ma, J. H.; Alpert, M. R.; Zhang, D.; Foley, B. J.; Smilgies, D.-M.; Lee, S.-H.; Choi, J. J. Origin of Vertical Orientation in Two-Dimensional Metal Halide

Perovskites and Its Effect on Photovoltaic Performance. *Nature Communications* **2018**, *9* (1), 1336. https://doi.org/10.1038/s41467-018-03757-0.

(57) Kojima, A.; Teshima, K.; Shirai, Y.; Miyasaka, T. Organometal Halide Perovskites as Visible-Light Sensitizers for Photovoltaic Cells. *J. Am. Chem. Soc.* **2009**, *131* (17), 6050–6051. https://doi.org/10.1021/ja809598r.

(58) *Best Research Cell-Efficiencies Chart - NREL*; National Renewable Energy Laboratory. https://www.nrel.gov/pv/cell-efficiency.html.

(59) Sahli, F.; Werner, J.; Kamino, B. A.; Bräuninger, M.; Monnard, R.; Paviet-Salomon, B.; Barraud, L.; Ding, L.; Diaz Leon, J. J.; Sacchetto, D.; Cattaneo, G.; Despeisse, M.; Boccard, M.; Nicolay, S.; Jeangros, Q.; Niesen, B.; Ballif, C. Fully Textured Monolithic Perovskite/Silicon Tandem Solar Cells with 25.2% Power Conversion Efficiency. *Nature Materials* **2018**, *17* (9), 820–826. https://doi.org/10.1038/s41563-018-0115-4.

(60) Lee, M. M.; Teuscher, J.; Miyasaka, T.; Murakami, T. N.; Snaith, H. J. Efficient Hybrid Solar Cells Based on Meso-Superstructured Organometal Halide Perovskites. *Science* **2012**, *338* (6107), 643. https://doi.org/10.1126/science.1228604.

(61) Chen, J.; Cai, X.; Yang, D.; Song, D.; Wang, J.; Jiang, J.; Ma, A.; Lv, S.; Hu, M. Z.; Ni, C. Recent Progress in Stabilizing Hybrid Perovskites for Solar Cell Applications. *Journal of Power Sources* **2017**, *355*, 98–133. https://doi.org/10.1016/j.jpowsour.2017.04.025.

(62) Krishna, A.; Gottis, S.; Nazeeruddin, M. K.; Sauvage, F. Mixed Dimensional 2D/3D Hybrid Perovskite Absorbers: The Future of Perovskite Solar Cells? *Advanced Functional Materials* **2019**, *29* (8), 1806482. https://doi.org/10.1002/adfm.201806482.

(63) Tsai, H.; Nie, W.; Blancon, J.-C.; Stoumpos, C. C.; Asadpour, R.; Harutyunyan, B.; Neukirch, A. J.; Verduzco, R.; Crochet, J. J.; Tretiak, S.; Pedesseau, L.; Even, J.; Alam, M. A.; Gupta, G.; Lou, J.; Ajayan, P. M.; Bedzyk, M. J.; Kanatzidis, M. G.; Mohite, A. D. High-Efficiency Two-Dimensional Ruddlesden–Popper Perovskite Solar Cells. *Nature* **2016**, *536* (7616), 312–316. https://doi.org/10.1038/nature18306.

(64) Shi, W.; Ye, H. Efficient and Stable Perovskite Solar Cells with a Superhydrophobic Two-Dimensional Capping Layer. *J. Phys. Chem. Lett.* **2021**, *12* (16), 4052–4058. https://doi.org/10.1021/acs.jpclett.1c01036.

(65) Zhu, Z.; Zhu, C.; Yang, L.; Chen, Q.; Zhang, L.; Dai, J.; Cao, J.; Zeng, S.; Wang, Z.; Wang, Z.; Zhang, W.; Bao, J.; Yang, L.; Yang, Y.; Chen, B.; Yin, C.; Chen, H.; Cao, Y.; Gu, H.; Yan, J.; Wang, N.; Xing, G.; Li, H.; Wang, X.; Li, S.; Liu, Z.; Zhang, H.; Wang, L.; Huang, X.; Huang, W. Room-Temperature Epitaxial Welding of 3D and 2D Perovskites. *Nature Materials* **2022**. https://doi.org/10.1038/s41563-022-01311-4.

(66) Reed, M. A. Quantum Dots. *Scientific American* **1993**, *268* (1), 118–123.

(67) Kouwenhoven, L.; Marcus, C. Quantum Dots. *Physics World* **1998**, *11* (6), 35. https://doi.org/10.1088/2058-7058/11/6/26.

(68) Murray, C. B.; Norris, D. J.; Bawendi, M. G. Synthesis and Characterization of Nearly Monodisperse CdE (E = Sulfur, Selenium, Tellurium) Semiconductor Nanocrystallites. *J. Am. Chem. Soc.* **1993**, *115* (19), 8706–8715. https://doi.org/10.1021/ja00072a025.

(69) Murray, C. B.; Kagan, C. R.; Bawendi, M. G. Self-Organization of CdSe Nanocrystallites into Three-Dimensional Quantum Dot Superlattices. *Science* **1995**, *270* (5240), 1335–1338. https://doi.org/10.1126/science.270.5240.1335.

(70) Gong, X.; Yang, Z.; Walters, G.; Comin, R.; Ning, Z.; Beauregard, E.; Adinolfi, V.; Voznyy, O.; Sargent, E. H. Highly Efficient Quantum Dot Near-Infrared Light-Emitting Diodes. *Nature Photonics* **2016**, *10* (4), 253–257. https://doi.org/10.1038/nphoton.2016.11.

(71) Yang, Z.; Fan, J. Z.; Proppe, A. H.; Arquer, F. P. G. de; Rossouw, D.; Voznyy, O.; Lan, X.; Liu, M.; Walters, G.; Quintero-Bermudez, R.; Sun, B.; Hoogland, S.; Botton, G. A.; Kelley, S. O.; Sargent, E. H. Mixed-Quantum-Dot Solar Cells. *Nature Communications* **2017**, *8* (1), 1325. https://doi.org/10.1038/s41467-017-01362-1.

(72) Dai, X.; Deng, Y.; Peng, X.; Jin, Y. Quantum-Dot Light-Emitting Diodes for Large-Area Displays: Towards the Dawn of Commercialization. *Advanced Materials* **2017**, *29* (14), 1607022. https://doi.org/10.1002/adma.201607022.

(73) Kagan, C. R. Flexible Colloidal Nanocrystal Electronics. *Chem. Soc. Rev.* **2019**, *48* (6), 1626–1641. https://doi.org/10.1039/C8CS00629F.

(74) Park, Y.-S.; Roh, J.; Diroll, B. T.; Schaller, R. D.; Klimov, V. I. Colloidal Quantum Dot Lasers. *Nature Reviews Materials* **2021**, *6* (5), 382–401. https://doi.org/10.1038/s41578-020-00274-9.

(75) Rakshit, S.; Piatkowski, P.; Mora-Seró, I.; Douhal, A. Combining Perovskites and Quantum Dots: Synthesis, Characterization, and Applications in Solar Cells, LEDs, and Photodetectors. *Advanced Optical Materials* **2022**, *n/a* (n/a), 2102566. https://doi.org/10.1002/adom.202102566.

(76) Ning, Z.; Gong, X.; Comin, R.; Walters, G.; Fan, F.; Voznyy, O.; Yassitepe, E.; Buin, A.; Hoogland, S.; Sargent, E. H. Quantum-Dot-in-Perovskite Solids. *Nature* **2015**, *523* (7560), 324–328. https://doi.org/10.1038/nature14563.

(77) Hosokawa, H.; Tamaki, R.; Sawada, T.; Okonogi, A.; Sato, H.; Ogomi, Y.; Hayase, S.; Okada, Y.; Yano, T. Solution-Processed Intermediate-Band Solar Cells with Lead Sulfide Quantum Dots and Lead Halide Perovskites. *Nature Communications* **2019**, *10* (1), 43. https://doi.org/10.1038/s41467-018-07655-3.

(78) Zhang, X.; Zhang, J.; Phuyal, D.; Du, J.; Tian, L.; Öberg, V. A.; Johansson, M. B.; Cappel, U. B.; Karis, O.; Liu, J.; Rensmo, H.; Boschloo, G.; Johansson, E. M. J. Inorganic CsPbI3 Perovskite Coating on PbS Quantum Dot for Highly Efficient and Stable Infrared Light Converting Solar Cells. *Advanced Energy Materials* **2018**, *8* (6), 1702049. https://doi.org/10.1002/aenm.201702049.

(79) Bederak, D.; Sukharevska, N.; Kahmann, S.; Abdu-Aguye, M.; Duim, H.; Dirin, D. N.; Kovalenko, M. V.; Portale, G.; Loi, M. A. On the Colloidal Stability of PbS Quantum Dots Capped with Methylammonium Lead Iodide Ligands. *ACS Appl. Mater. Interfaces* **2020**, *12* (47), 52959–52966. https://doi.org/10.1021/acsami.0c16646.

(80) Ling, X.; Yuan, J.; Ma, W. The Rise of Colloidal Lead Halide Perovskite Quantum Dot Solar Cells. *Acc. Mater. Res.* **2022**, *3* (8), 866–878. https://doi.org/10.1021/accountsmr.2c00081.

(81) Zhao, Q.; Hazarika, A.; Chen, X.; Harvey, S. P.; Larson, B. W.; Teeter, G. R.; Liu, J.; Song, T.; Xiao, C.; Shaw, L.; Zhang, M.; Li, G.; Beard, M. C.; Luther, J. M. High Efficiency Perovskite Quantum Dot Solar Cells with Charge Separating Heterostructure. *Nature Communications* **2019**, *10* (1), 2842. https://doi.org/10.1038/s41467-019-10856-z.

(82) Lu, H.; Chen, X.; Anthony, J. E.; Johnson, J. C.; Beard, M. C. Sensitizing Singlet Fission with Perovskite Nanocrystals. *J. Am. Chem. Soc.* **2019**, *141* (12), 4919–4927. https://doi.org/10.1021/jacs.8b13562.

Chapter 2: Controlling the crystal structure of an organic semiconductor, TIPS-pentacene, using tunable, crystalline two-dimensional perovskite interfaces

Contributors: Ashley M. Conley, Stephanie Guthrie, Alex Chen, Kevin Stone, Joshua J. Choi, and Gaurav Giri

This chapter is in preparation for a manuscript submission.

2.1 Abstract

Organic semiconductors are becoming increasingly competitive with conventional amorphous silicon due to their solution processability at room temperature, which allows for inexpensive, high-throughput fabrication of lightweight, flexible devices. An inherent disadvantage of organic semiconductors is their propensity to adopt multiple molecular packing motifs which yield highly-contrasting charge transport and optoelectronic properties. Also affected is singlet fission, an exciton multiplication process, that has the potential to break the Shockley-Queisser limit with profound implications for next generation solar cells. Six interface-stabilized molecular packing structures of TIPS-pentacene, an organic semiconductor, were isolated via solution deposition and subsequent thin film relaxation on two-dimensional lead halide perovskites, which act as highly-ordered self-assembled monolayers with tunable ligand density and modifiable ligands. Using grazing incidence X-ray diffraction, distinct crystal structures with incremental changes in the (101) plane spacing were revealed, spanning an astonishingly small range of 0.12 Angstroms. We show that using ordered interfaces, phase purity is greatly enhanced. This work motivates using a plethora of combinations of two-dimensional perovskite structures and organic small molecules to control structural-optoelectronic properties using interface engineering.

2.2 Introduction

Controlling structure-property relationships of organic semiconductors (OSCs) s is vital for their commercialization in organic light emitting diodes, organic field effect transistors, and organic solar cells. Small molecule OSCs often adopt multiple molecular packing motifs and varying morphologies which are difficult to control and have extensive effects on solid-state properties (electronic, thermodynamic, mechanical, and kinetic).[1–3] As a result, molecular packing crystal structure directly impacts device performance. Minute changes in molecular packing can affect the π-orbital overlap between molecules, which can result in alterations of optical properties and orders of magnitude changes in electronic transport properties.[4,5] One such property is singlet fission, an exciton multiplication process that occurs via interactions arising from π-orbital overlap. Singlet fission has been observed in multiple prominent OSC molecules and can be highly sensitive to molecular packing.[6–10] For some molecules, external quantum efficiencies have surpassed 100% in singlet fission-based tandem solar cells by alleviating thermalization losses, providing an opportunity to exceed the Shockley-Queisser limit of single-junction solar cells.[11–13] Molecular packing and morphological changes to an organic crystal have been shown to alter singlet fission rates, triplet exciton transport, and triplet state lifetimes, and therefore control of these crystalline properties are necessary for control of singlet fission properties.[8,14,15]

It is difficult to control the molecular packing of organic molecular crystals, as these crystal structures form through nonselective Van der Waals forces and electrostatic interactions, and the resulting structures are often similar in energy. Unsurprisingly, molecular packing is acutely sensitive to parameters such as deposition method, temperature, solvent, substrate, self-assembled monolayers, speed of deposition, and postdeposition processing. For example, thermodynamically stable, metastable, and strain-stabilized structures of the prototypical organic semiconductor 6,13-

bis(triisopropylsilylethynyl)pentacene (TIPS-pentacene) as well as other small molecules have been isolated using a wide range of solution deposition techniques such as solution shearing,[16–19] spin coating,[20] and capillary pen writing deposition.[21] These structures have exhibited varying electronic and optical properties. Metastable crystal packing structures can offer enhanced properties, but ultimately suffer from a lack of stability whereby over time, conversion to a thermodynamically stable structure occurs. Interestingly, Diao, et al. isolated the five most commonly referenced molecular packing structures of TIPS-pentacene, yet also computationally found a relatively flat energetic landscape for the crystal structures and discovered numerous other potential energy minima, akin to metabasins, corresponding to other structures not yet observed experimentally.[5] Given all these complications, controlling the molecular packing of organic semiconductors is a multifaceted problem facing the field of crystal engineering, and new methods to control crystallization would be beneficial to the field.

Substrate functionalization using self-assembled monolayers (SAMs) has been used to control molecular orientation, morphology, crystallization kinetics, and crystal grain size.[22–24] Using SAMs, charge transport mobilities of polycrystalline OSCs rivaling that of their single crystal counterparts have been achieved,[22,25–27] highlighting the utility of interface engineering in enhancing solid-state properties. Further, pentacene and C_{60} thin films grown on more-ordered (i.e. higher density) octadecylsilane SAMs exhibited higher mobilities, by factors of 3 and 8, respectively, than those on disordered (i.e. lower density) SAMs.[27] However, tunability of SAM ligand density is limited due to an inherent lack of long-range ordering arising from non-specific reaction sites when SAM molecules attach to silicon surfaces, restricting their use to systematically control molecular packing.

In this work, we demonstrate precise control over the molecular packing of TIPS-pentacene and isolate six phase-pure structures using crystalline interfaces. While perovskites are a class of materials of great scientific significance,[28–33] we exploit their structural tunability as surfaces for OSC crystallization. To overcome ligand density limitations of traditional SAMs, we use one-layer two-dimensional (2D) lead halide perovskites (**Fig. 2.1a**) whose composition can be altered to modify the ligand molecule and ligand density by up to 30 percent.

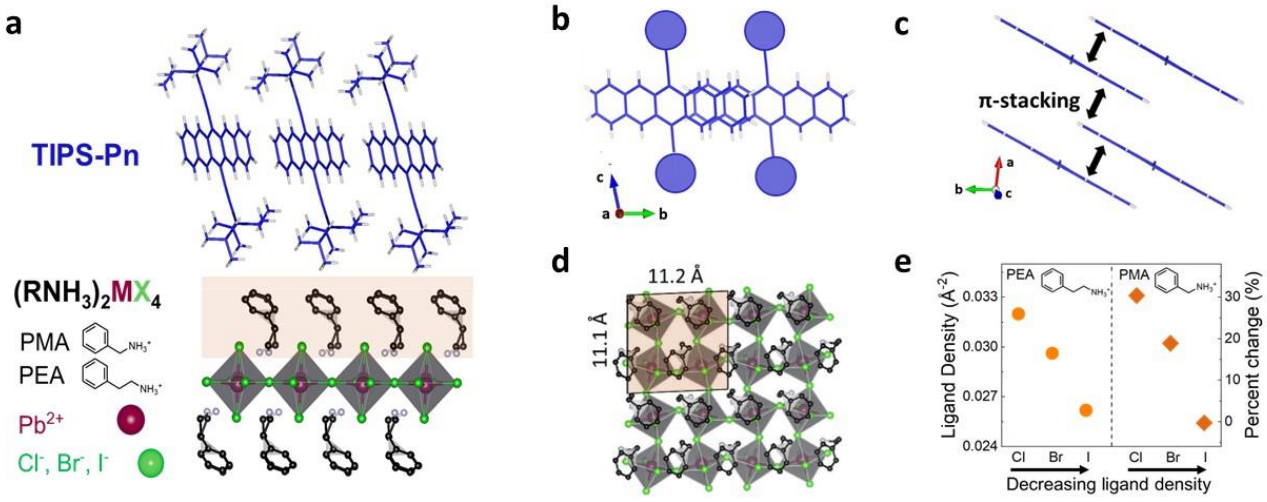

Figure 2.1. Bilayer thin films of TIPS-pentacene and 2D perovskite. **a)** Schematic of one-layer two-dimensional perovskite and TIPS-pentacene interface. **b)** Depiction of the TIPS-pentacene molecular offset of pentacene backbones as viewed down the a-axis crystallographic direction. **c)** Schematic π-π stacking distances between TIPS-pentacene molecules (black arrows). Variations in (101) plane spacing will result in changes in both the π-stacking and molecular offset, which dictate overall intermolecular interactions. **d)** The ligand-terminated perovskite surface of PEA_2PbCl_4 in the a-b plane showing the number of ligands per a-b area. **e)** Calculated ligand densities of perovskites with varying ligand and halide composition and their respective relative changes in ligand density.

2.3 Organic semiconductor-perovskite thin film fabrication and characterization

2.3.1 Fabrication of bilayer thin films

The bilayer thin film fabrication scheme can be found in **Fig. 2.2**. 2D perovskite thin films were fabricated using dynamic spin coating from a perovskite precursor solution followed by thermal annealing at 100° C. TIPS-pentacene thin films were deposited directly onto perovskite surfaces using a solution deposition technique known as solution shearing.[19,34] Though a wide range of crystal morphologies and molecular packings, both metastable and thermodynamically stable, have been obtained by varying solution shearing deposition parameters,[17,18,35] solution shearing deposition conditions were held constant in this study while varying only the 2D lead halide perovskite interfaces. TIPS-pentacene/perovskite thin films were solvent vapor annealed in toluene to alleviate strain and relax TIPS-pentacene thin films to their thermodynamically stable structures, as previously executed.[17]

2.3.2 Using 2D perovskites as crystalline, tunable templates for crystallization

By selecting perovskites with one-layer dimensionality, perovskite thin films preferentially crystallize in horizontal orientation with periodic ligand termination on the thin film surface. Horizontal orientation (parallel to the substrate) of the lead-halide octahedra sheets was confirmed

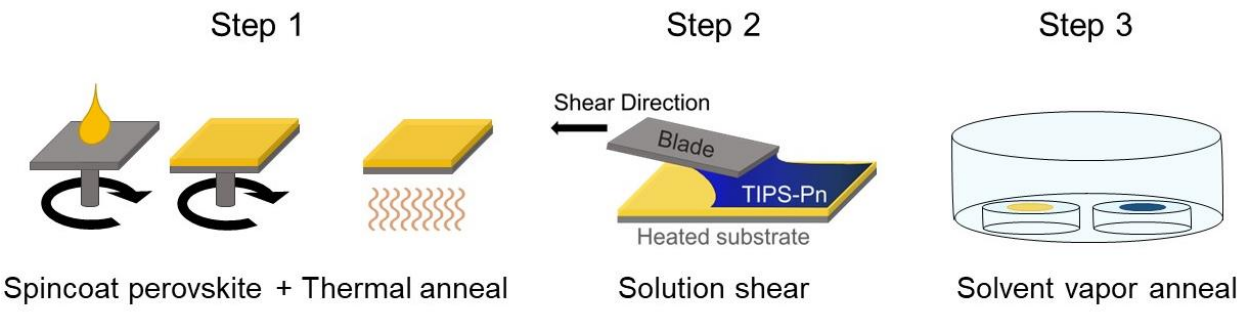

Figure 2.2. Solution processing diagram of TIPS-pentacene/perovskite bilayer thin films.

by fitting diffraction peaks with published unit cell parameters for each perovskite (**Fig. 2.3**). The surface chemistry of 2D perovskites was altered in two ways: changing the halide composition tuned ligand density from 0.025 to 0.033 $Å^{-2}$ (32 percent relative increase) (**Fig. 2.1d-e**), and altering the cation precursors changed the organic ligand terminating the surface. Ligand density was calculated using published unit cell parameters (Table 2.1). Utilizing a perovskite composition with chlorine and iodine results in higher and lower ligand density, respectively. We used phenylmethylammonium (PMA) and phenylethylammonium (PEA) ligands to modify surface chemistry. PEA forms a long-range π-stacking network while PMA ligands are more isolated, resulting in different ligand orientations and leading us to expect changes in surface energies.[36,37]

2D perovskite	a-b surface area ($Å^2$)	Ligands per a-b surface area	Ligand density (ligand/$Å^2$)	Area per ligand ($Å^2$/ligand)
[37]PMA_2PbCl_4	60.43	2	0.0331	30.22
[36]PEA_2PbCl_4	125.04	4	0.0320	31.26
[38]PMA_2PbBr_4	66.17	2	0.0302	33.09
[39]PEA_2PbBr_4	135.05	4	0.0296	33.76
[40]PMA_2PbI_4	78.66	2	0.0254	39.33
[38]PEA_2PbI_4	76.38	2	0.0262	38.19

Supplementary Table 2.1. Calculated ligand densities for 2D perovskites using structures with lattice parameters as previously characterized in the literature.

In order to use 2D perovskites as templates for organic semiconductor crystallization, their stability against toluene solvent exposure in the form of solution shearing directly on the surface followed by solvent vapor exposure during solvent vapor annealing was studied. Diffraction patterns for the perovskite thin films before TIPS-pentacene thin film deposition, after TIPS-pentacene deposition from a toluene solution, and after solvent vapor annealing in toluene for one

hour are shown in **Fig. 2.4**. Absorbance spectra before after toluene exposure is shown in **Fig. 2.5**. Diffraction patterns show strong diffraction peaks for 2D perovskites at each processing step and the strong characteristic absorption was preserved, indicating that no structural changes occurred, orientation was unchanged, and high crystallinity was retained after the solution deposition of TIPS-pentacene and solvent vapor annealing.

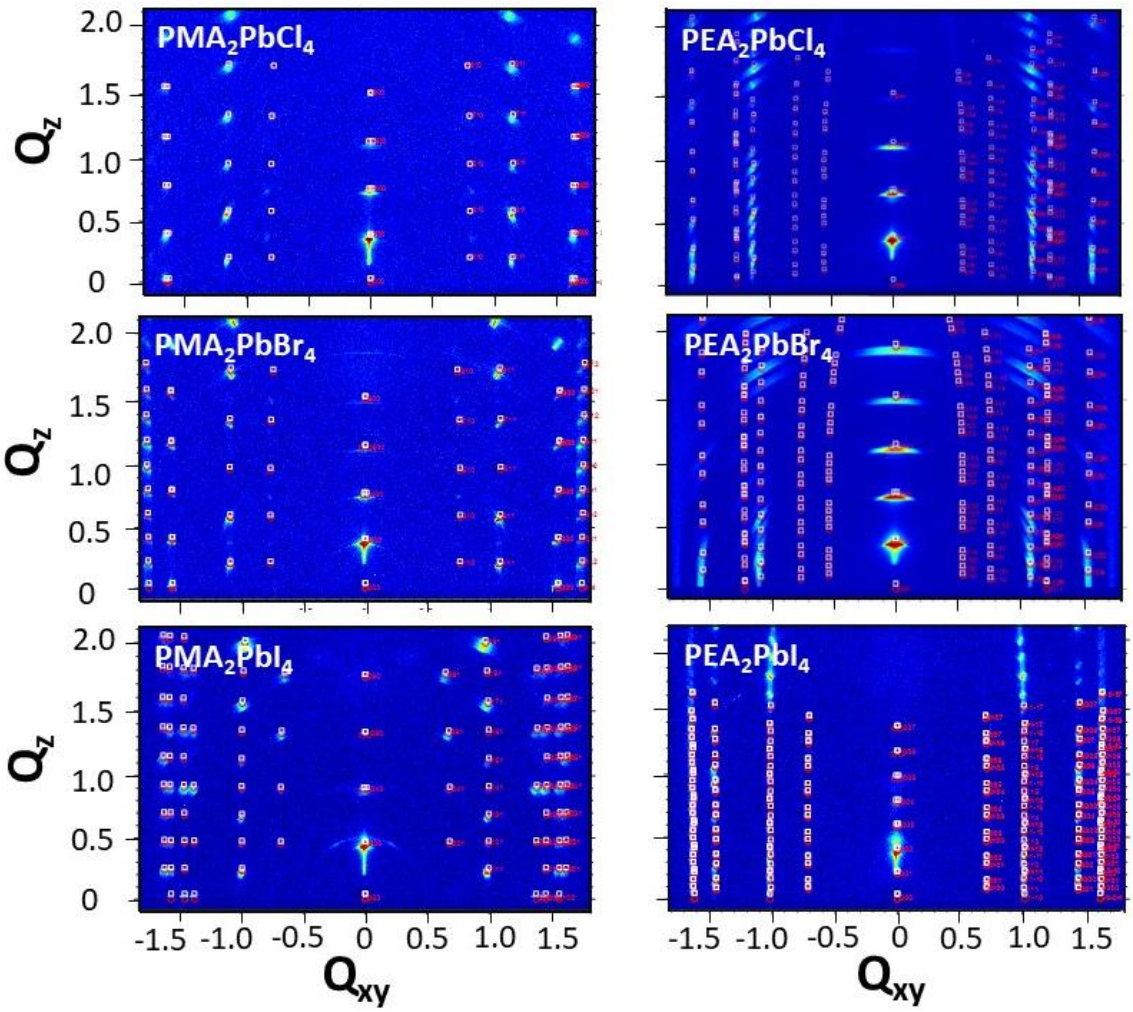

Figure 2.3. Diffraction patterns of 2D perovskite thin films. Peak indexing was performed using GIXSGUI software and using previously published 2D perovskite structures. Perovskite octahedra sheets were shown to be horizontally oriented with respect to the silicon substrate with the long crystallographic axis orthogonal to the substrate, showing that organic ligands terminated the perovskite thin film surfaces.

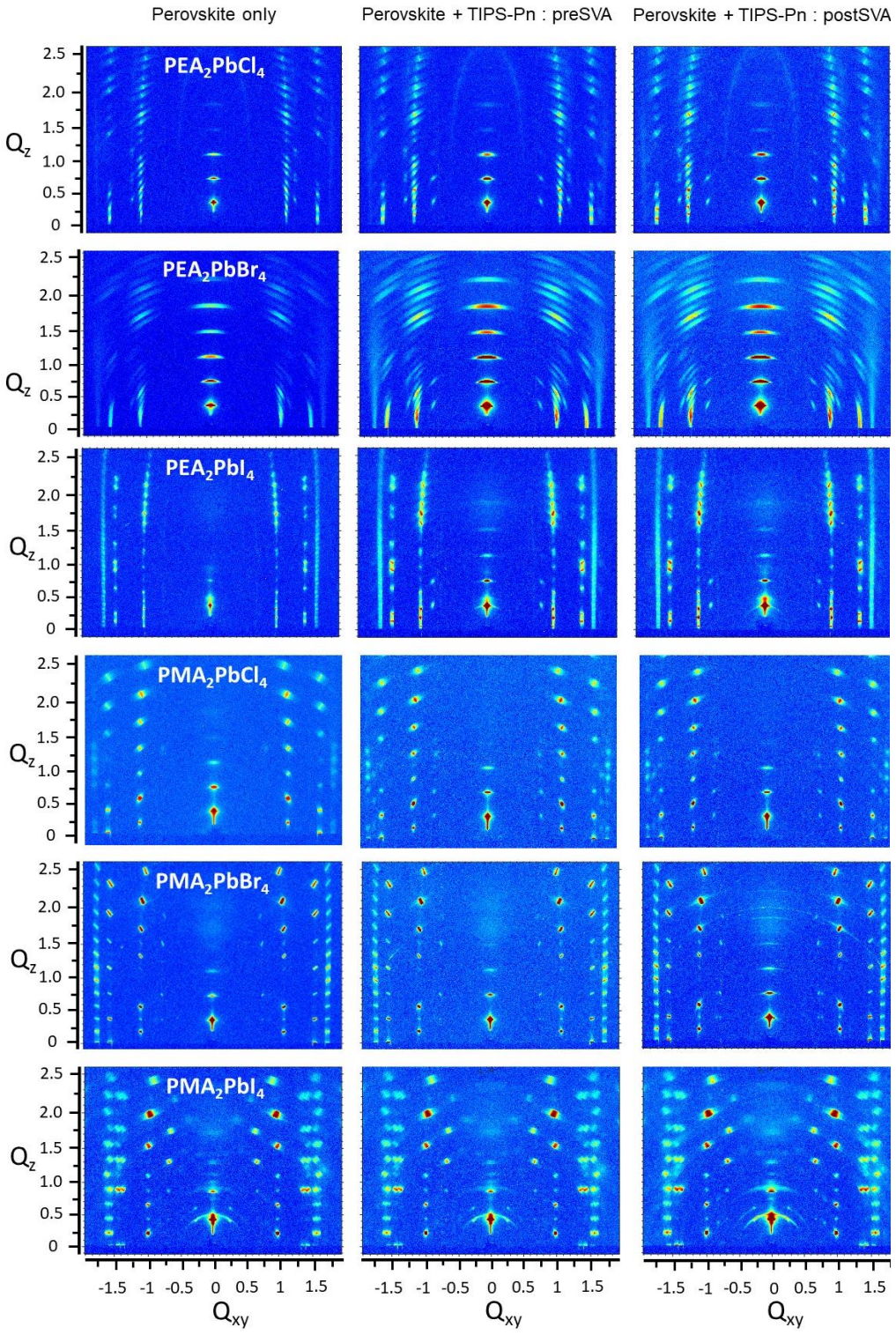

Figure 2.4. Diffraction patterns of 2D perovskite control samples and bilayer perovskite and TIPS-pentacene samples before and after solvent vapor annealing in toluene. No changes in the 2D perovskite diffraction patterns after the solution deposition of TIPS-pentacene and solvent vapor annealing was observed, indicating that the crystal structure of the 2D perovskites was not affected by TIPS-pentacene solution processing conditions with toluene solvent.

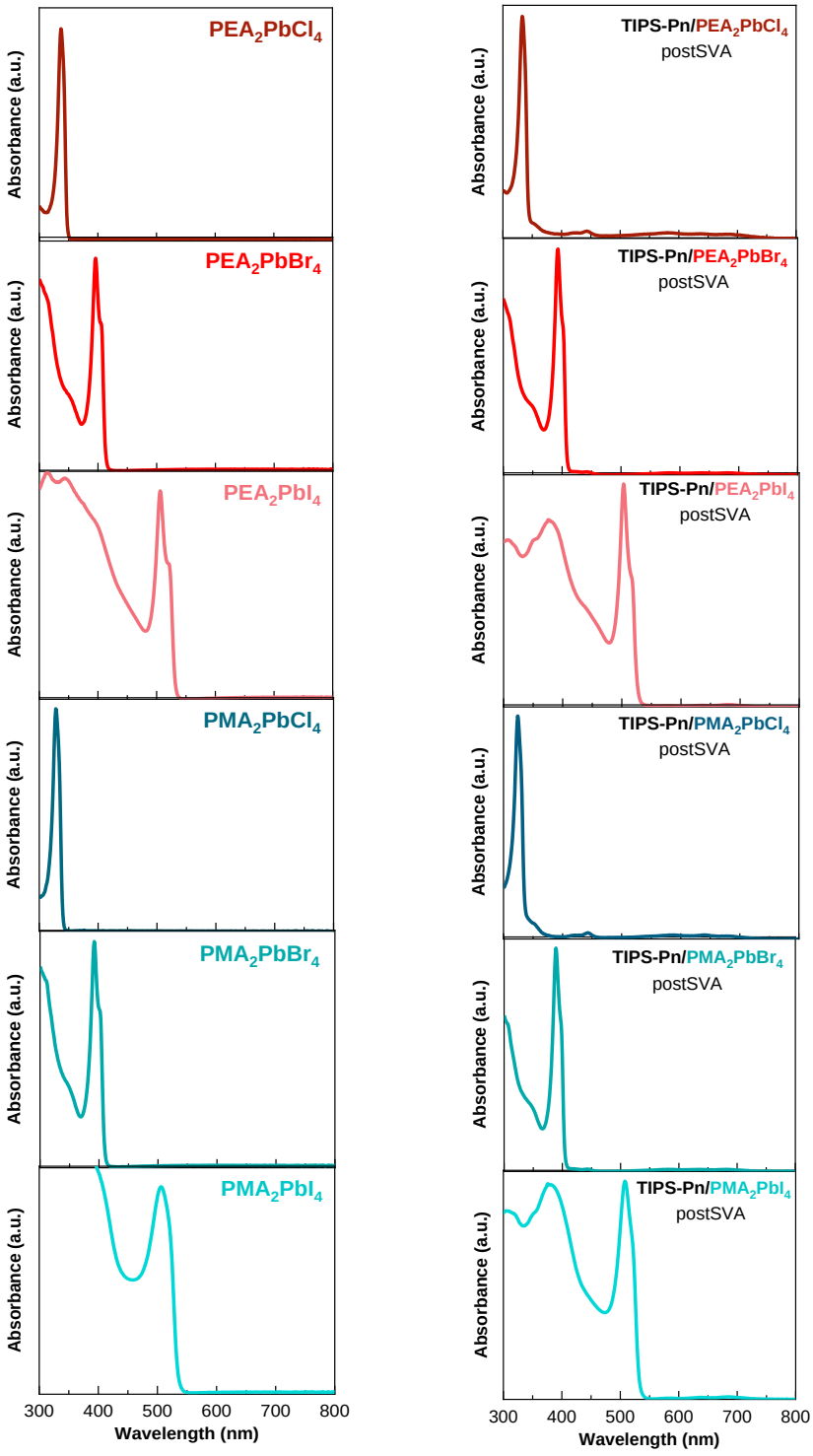

Figure 2.5. Absorbance spectra of 2D perovskites thin films before and after the deposition of TIPS-pentacene from solution in toluene followed by one hour of solvent vapor annealing in toluene. The sharp perovskite onset absorption peak is retained after TIPS-pentacene deposition and post deposition processing.

2.4 Structural characterization of molecular packing structures of TIPS-pentacene

2.4.1 TIPS-pentacene thin film morphology

Polarized optical microscopy showed similar morphologies of TIPS-pentacene thin films regardless of perovskite surface (**Fig. 2.6**). Thin films consisted of long crystalline grains aligned in the solution shearing direction (white arrows), as observed using 90^{o} rotation under polarized light with crystals being hundreds of microns in length and tens of microns in width (**Fig. 2.7**). TIPS-pentacene morphology and crystal alignment were conserved after solvent vapor annealing, indicating that no secondary nucleation and growth occurred (**Fig. 2.8**). Because optoelectronic

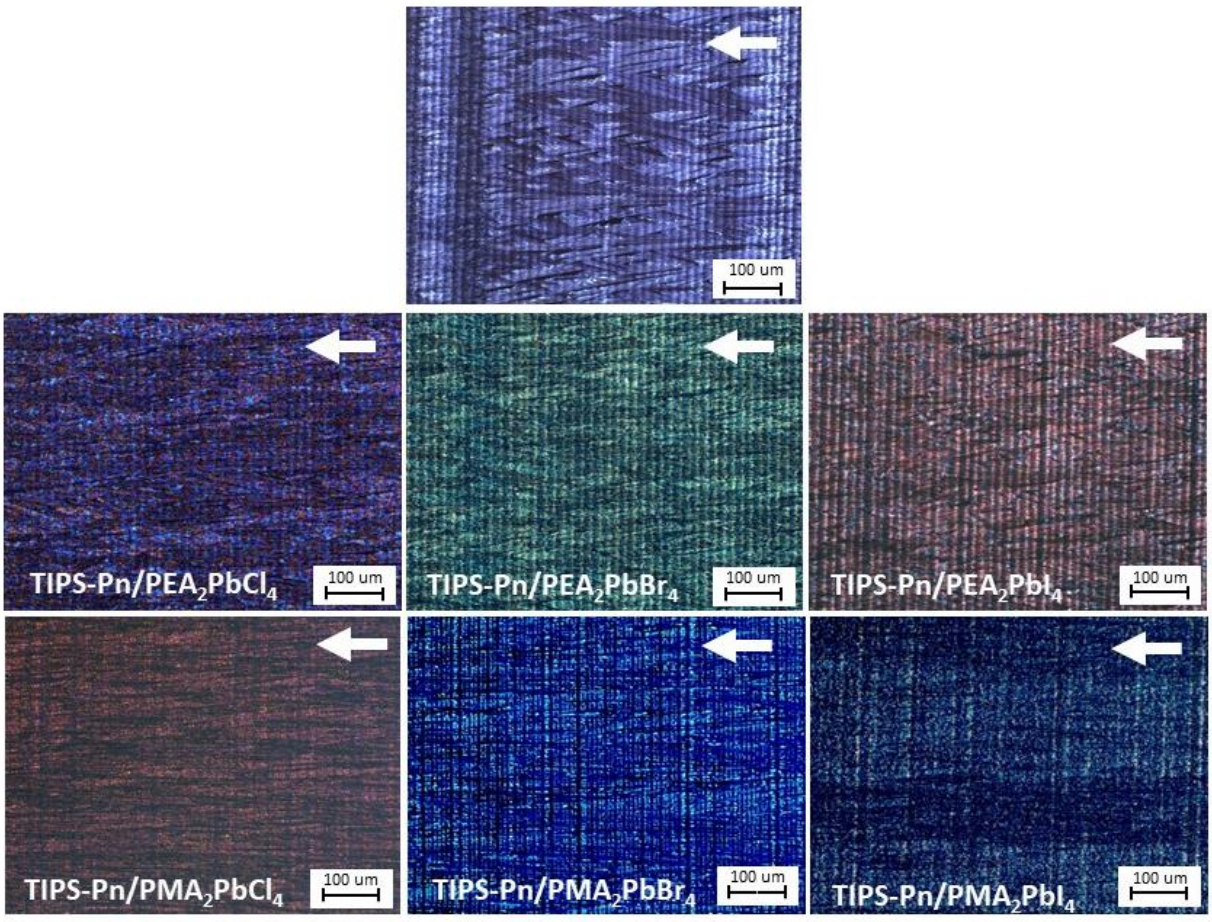

Figure 2.6. Cross-polarized images of TIPS-pentacene thin films after solvent vapor annealing for one hour in toluene vapor on 2D perovskite surfaces. Crystals remain aligned in the shearing direction regardless of perovskite surface.

properties are influenced by both molecular packing and morphology, identical morphologies obtained in this study allow an opportunity to determine the effect of molecular packing and phase purity on optoelectronic properties without morphological variation.

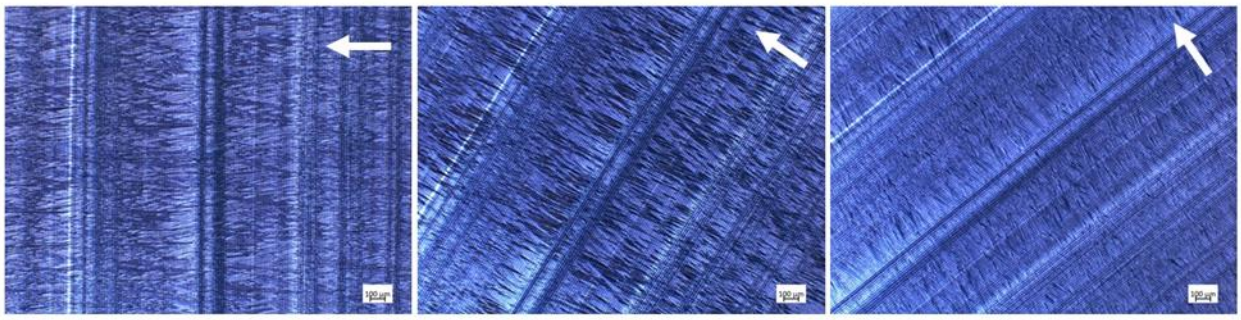

Figure 2.7. Cross-polarized images of TIPS-pentacene thin films with rotation. Crystalline domains grow in the direction of translation of the shearing blade, resulting in highly aligned thin films. Upon rotation of the thin films, there is uniform brightness over the entirety of the film, indicating that crystals are of the same domain and orientation.

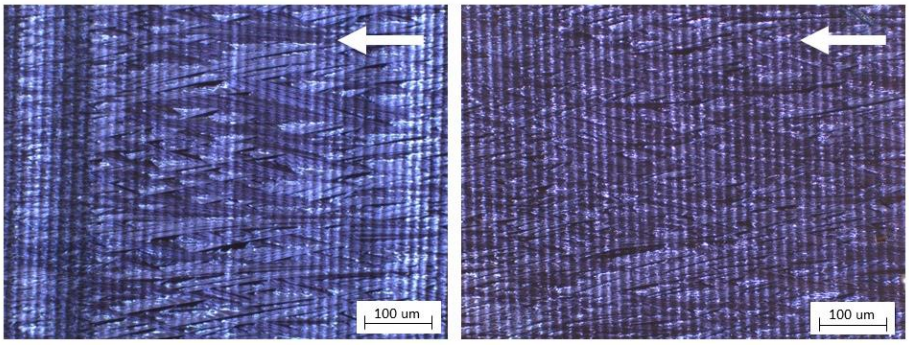

Figure 2.8. Cross-polarized images of TIPS-pentacene thin films before (left) and after (right) solvent vapor annealing for one hour in toluene vapor. Solvent vapor annealing provided a pathway for relaxation of TIPS-pentacene thin films to relieve any strain and/or kinetically trapped structures, yielding thermodynamically stable thin films at room temperature.

2.4.2 Thickness of TIPS-pentacene thin films

Stylus profilometry in conjunction with UV-vis spectroscopy was used to quantify the thicknesses of TIPS-pentacene thin films. TIPS-pentacene thin films were prepared with a constant concentration of 8 milligrams per milliliter with varying speeds of the shearing blade to alter thin film thickness. Within the evaporative regime, termed the Landau-Levich regime, lower shearing blade speeds creates thicker thin films.[34] As the shearing blade speed is increased, thinner films are created. The selected shearing conditions are within the evaporative regime, as previously

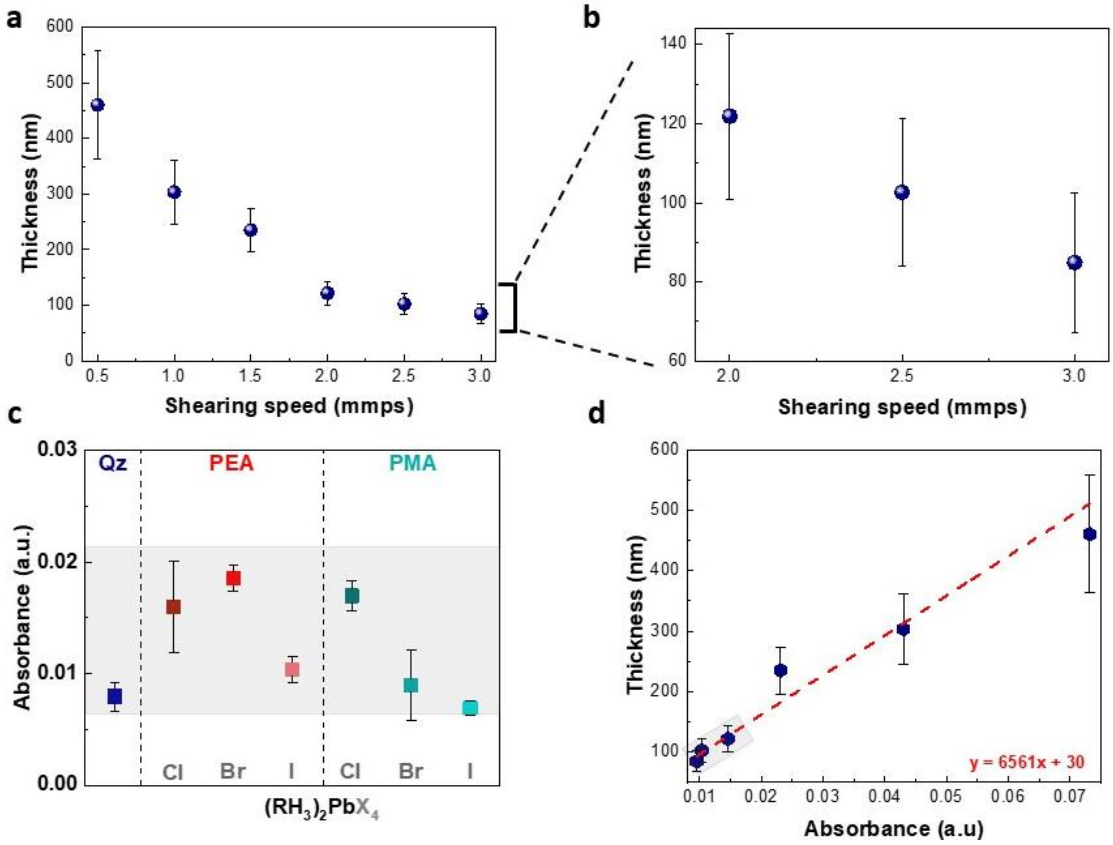

Figure 2.9. a) Thickness of TIPS-pentacene thin films versus solution shearing speed. **b)** Zoom in on the thicknesses of TIPS-pentacene thin films when deposited at higher solution shearing speeds. **c)** The absorbance values of TIPS-pentacene when deposited on quartz and different 2D perovskite surfaces. **d)** Thickness of TIPS-pentacene thin films versus absorbance values. The gray region shows the range in absorbance values observed for TIPS-pentacene when deposited on different 2D perovskite surfaces. The thicknesses of TIPS-pentacene thin films with different perovskite surfaces are 110 ± 30 nm.

reported[34] and can be seen by the negative correlation between shearing speed and thin film thickness in **Fig. 2.9a-b**. Because TIPS-pentacene thin films are deposited on different perovskite thin films, TIPS-pentacene thicknesses could not be measured directly with profilometry. The absorbances of TIPS-pentacene thin films with varying thicknesses was measured to construct a calibration curve which was then used to correlate absorbance with thin film thickness (**Fig 2.9c-d**). Using this analysis, the thicknesses of TIPS-pentacene thin films when deposited on perovskites was determined to be 110 ± 30 nm.

2.4.2 Crystal structure analysis via grazing incidence X-ray diffraction

Grazing incidence X-ray diffraction was used to determine the influence of perovskite ligand and ligand density on the molecular packing of TIPS-pentacene. Due to anisotropy of TIPS-pentacene thin films, diffraction patterns were collected with the incident X-ray beam along the shearing direction and with 90° rotation with respect to the shearing direction to observe the (101) and (011) crystallographic planes, respectively (**Fig. 2.10b-c**). TIPS-pentacene diffraction patterns are qualitatively and quantitatively (Table 2.2) consistent with the published Form I molecular packing structure of TIPS-pentacene, as reported by Diao et al.[5]

	This study Q_{xy} (Å^{-1})	**Form I Q_{xy} (Å^{-1})**	**Form Ib Q_{xy} (Å^{-1})**	**Form IIb Q_{xy} (Å^{-1})**	**Form III Q_{xy} (Å^{-1})**
(101) plane	0.821	0.82	0.83	0.86	0.90
(011) plane	0.802	0.81	0.80	0.775	0.77

Table 2.2. Comparison of the Q_{xy} values of the TIPS-pentacene (101) and (011) planes for the TIPS-pentacene control (solution sheared on silicon) and the published Form I, Form Ib, Form IIb, and Form III as characterized by Diao et al [ref. 5]. The TIPS-pentacene structure isolated in this study best matches the Form I molecular packing.

	This study d-spacing (Å)	Form I d-spacing (Å)	This study Q ($Å^{-1}$) - control	This study Q ($Å^{-1}$) - min	This study Q (Å) - max	Form I Q (Å)
(101) plane	7.00 ± 0.06	6.98	0.898 ± 0.08	0.890	0.904	0.900
(011) plane	6.49 ± 0.02	6.34	0.967 ± 0.03	0.962	0.970	0.991

Table 2.3. Comparison of the d-spacing and Q values of the (101) and (011) planes in this study and the published Form I molecular packing of TIPS-pentacene as characterized by Diao et al [ref. 5]. The Q-values of control corresponds to the TIPS-pentacene films deposited in silicon while the Q-min and Q-max values correspond to the range observed on the 2D perovskite surfaces.

The highest and lowest TIPS-pentacene (101) plane spacing values obtained from interfacing with perovskites were 7.05 Å and 6.95 Å for the (101) plane, and 6.53 Å and 6.48 Å for the (011) plane. While all structures are within the Form I family, the (101) and (011) plane spacings of TIPS-pentacene were uniquely influenced by perovskite surfaces. Perovskite surfaces induced peak shifts in the (101) plane from lower Q-values (bottom left) to higher Q-values (upper right) (**Fig. 2.10a**). These perovskite-templated TIPS-pentacene structures exhibited discrete (101) plane spacings ranging from 6.95 A to 7.06 A (~1.6% change). Untemplated TIPS-pentacene exhibited an average (101) plane spacing of 7.00 ± 0.06 Å, which has a significantly larger standard deviation relative to perovskite-templated structures (**Fig. 2.10d)**. This indicates poor control over TIPS-pentacene molecular packing and more structural variation when deposited on silicon. In contrast, TIPS-pentacene molecular packing was finely-tuned using perovskite surfaces with varying ligand and ligand density, as evidenced by discrete spacings with substantially lower standard deviations.

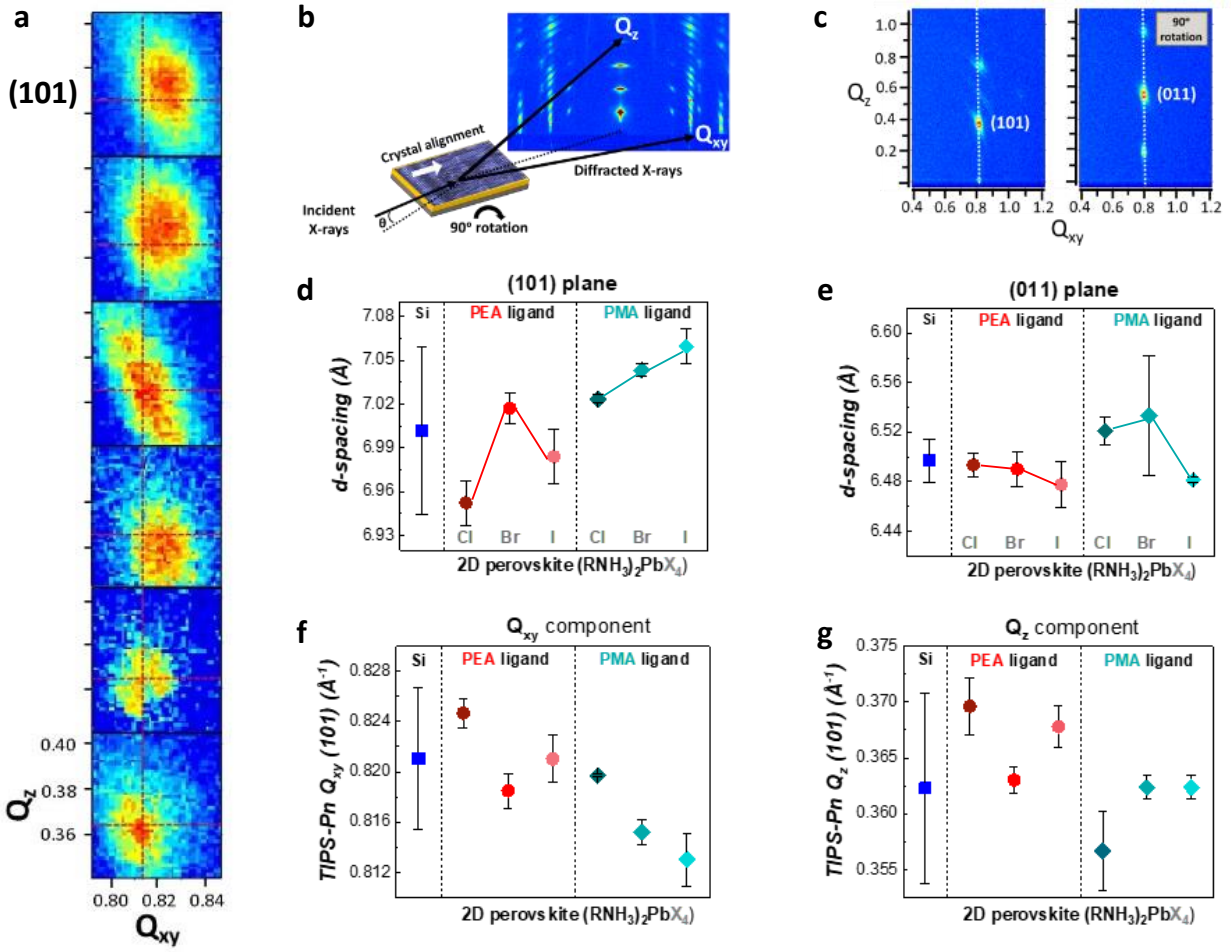

Figure 2.10. Crystal structure analysis of TIPS-pentacene (101) and (011) diffraction peaks using grazing incidence X-ray diffraction (GIXD). **a)** Incremental peak shift of the TIPS-pentacene (101) plane from lower Q (bottom) to higher Q (top) was observed on different 2D perovskite surfaces. **b)** Depiction of GIXD technique with incoming X-rays parallel to crystal alignment in TIPS-pentacene thin films. **c)** Diffraction pattern showing the (101) and (011) plane peaks when X-ray beam is parallel to crystal alignment and with 90° rotation, respectively. **d)** (101) and **e)** (011) plane spacings of TIPS-pentacene on perovskite surfaces with varying ligand and ligand density. **f)** The Q_{xy} component of the (101) plane showing variation along the a-axis of the unit cell which is closely related to the π-stacking direction. **g)** The Q_z component of the (101) plane suggesting variation in the tilting of the c-axis.

Perovskite-templated structures exhibited high phase purity with reduced structural disorder. The (011) plane of untemplated TIPS-pentacene was observed concomitantly with a second peak that is separated in Q_z. This feature has been attributed to degenerate peaks with similar d-spacings.[5,41] For perovskite-templated TIPS-pentacene structures, this degeneracy was removed, which is consistent with increased ordering in these systems. Only minor variations in (011) plane spacings were observed (**Fig. 2.10e**), indicating that TIPS-pentacene molecular packing changes occurred mostly along the a-axis of the unit cell (i.e. (101) plane) rather than the b-axis. These results show that TIPS-pentacene molecular packing can be finely-tuned using tunable, crystalline surfaces beyond the control of deposition of TIPS-pentacene on a silicon substrate.

While unit cell parameters for TIPS-pentacene molecular packings could not be obtained due to too few independent Bragg peaks (i.e., without perovskite peaks overlapping), analysis of Q_{xy} and Q_z components of the Q-vector in reciprocal space for (101) peaks provide qualitative information about relative changes to the unit cell. As shown in **Fig. 2.10f**, perovskite-templated structures exhibited discrete Q_{xy} components that provided unique contributions to Q-vector and is representative of changes to the a-axis length of the unit cell, which is closely related to the π-stacking direction.[5,21] The overall change in Q_{xy} for perovskite-templated samples was 1.7% and high variability was observed again for untemplated TIPS-pentacene. Upon inspection of the Q_z components of the (101) peak (Fig. 2g), distinct Q_z values were observed for perovskite-templated samples (**Fig. 2.10g**), possibly suggesting changes in the tilt of the c-axis with respect to the ab-plane.

No trend in TIPS-pentacene (101) plane spacing and ligand density was observed. For PEA perovskites, the TIPS-pentacene (101) plane spacing increases with halides in the order Cl<I<Br

while ligand density increases in the order I<Br<Cl. For PMA-terminated perovskites, (101) plane spacing increases in the order Cl<Br<I. Without a clear correlation to ligand density, these results suggest that no direct lattice matching is taking place. Interestingly, perovskites with similar ligand density but different ligand molecule (e.g. PEA_2PbCl_4 and PMA_2PbCl_4), induced different (101) d-spacings of TIPS-pentacene. Taken together, these observations suggest that both ligand and halide selection contribute to defining the electrostatic interaction at the interface.

Because perovskite-templated structures were relaxed (i.e. strain-free) using solvent vapor annealing, final structures are thermodynamically stable with their distinctions stemming from unique interfacial interactions for each TIPS-pentacene/perovskite pairing. The nonspecific structure formation as evidenced by increased structural variation in untemplated samples is consistent with there being no particular energetic minimum when interfaced with silicon. The thicknesses of TIPS-pentacene thin films are 110 + 30 nm, demonstrating that TIPS-pentacene/perovskite interactions are significant enough to propagate into the bulk of the film and still yield phase pure structures.

2.5 Conclusion

Small molecule organic semiconductors, such as TIPS-pentacene, adopt different molecular packing structures with varying optoelectronic properties stemming from differences in intermolecular interactions. However, controlling the molecular packing of small molecules is difficult. Molecular packing is acutely sensitive to deposition method, concentration solvent, temperature, and other parameters. Here, we show that the molecular packing of TIPS-pentacene can be finely tuned via the solution deposition on crystalline, ordered surfaces. We isolated six unique molecular packing structures using six two-dimensional lead halide perovskites, which have modifiable ligand molecules and ligand density. Structural disorder in TIPS-pentacene thin films is reduced substantially by interfacing with 2D perovskites relative to deposition on unfunctionalized silicon. Attempts to use traditional self-assembled monolayers to influence packing have stopped short of ligand density tunability. We provide an easy-to-adopt method to reduce structural disorder using tunable, crystalline interfaces, 2D perovskites, which are simple and fast to fabricate. Perovskite-templating could prove advantageous in other small molecule applications where even modest amounts of disorder can severely hinder device functionality. The number of molecule-perovskite combinations are extensive, making the perovskite-templating method generalizable to application-based and fundamental studies to elucidate structure-property relationships via the fine tuning of crystalline structures.

2.6 Materials and Methods

Materials. The following 2D perovskite precursor reagents were purchased from Sigma Aldrich: lead chloride ($PbCl_2$, 99.999% trace metals analysis), lead bromide ($PbBr_2$, 99.999% trace metals analysis), phenylmethylammonium chloride (PMACl, MQ200), phenylmethylammonium bromide (PMABr, ≥98%), phenylmethylammonium iodide (PMAI, ≥98%), phenylethylammonium chloride (PEACl, ≥98%), phenylethylammonium bromide (PEABr, ≥98%), phenylethylammonium iodide (PEAI, ≥98%), 6,13-Bis(triisopropylsilylethynyl)pentacene (TIPS-pentacene, ≥99%), N-N-dimethylacetamide (DMAc, anhydrous, 99.8%), dimethyl sulfoxide (DMSO, anhydrous, ≥99.9%) and toluene (anhydrous, ≥99.5%). Lead iodide (PbI_2, 99.9985%) was purchased from Alfa Aesar.

Substrate preparation. Silicon and quartz substrates were cleaned sequentially via sonification in detergent water, high purity water, isopropyl alcohol, and acetone for 8 minutes each. The slides were then dried using air followed by UV ozone treatment for 15 minutes.

Lead halide perovskite solution preparation. All perovskite precursor solutions were prepared with empirical formula A_2PbX_4 (A = PMA, PEA) (X = Cl, Br, I) with a concentration of 0.375 M with respect to lead. A 0.375 M solution of **$(PMA)_2PbCl_4$** was prepared by dissolving 0.375 M of $PbCl_2$ and 0.75 M of PMACl using DMSO as the solvent. A 0.375 M solution of **$(PEA)_2PbCl_4$** was prepared by dissolving 0.375 M of $PbCl_2$ and 0.75 M of PEACl using DMSO as the solvent. A 0.375 M solution of **$(PMA)_2PbBr_4$** was prepared by dissolving 0.375 M of $PbBr_2$ and 0.75 M of PMABr using DMAc as the solvent. A 0.375 M solution of **$(PEA)_2PbBr_4$** was prepared by dissolving 0.375 M of $PbBr_2$ and 0.75 M of PEABr using DMAc as the solvent. A 0.375 M solution

of **$(PMA)_2PbI_4$** was prepared by dissolving 0.375 M of PbI_2 and 0.75 M of PMAI using DMAc as the solvent. A 0.375 M solution of **$(PEA)_2PbI_4$** was prepared by dissolving 0.375 M of PbI_2 and 0.75 M of PEAI using DMAc as the solvent. Solutions were allowed to stir overnight.

Lead halide perovskite thin film fabrication. Perovskite precursor solutions were dynamically spin coated on clean substrates at 4500 rpm for 60 seconds. Thin films were then thermally annealed at 100^o C for 5 minutes.

TIPS-pentacene thin film fabrication. A solution of 8 mg/mL of TIPS-pentacene in toluene was prepared. An aliquot (15 uL) of TIPS-pentacene solution was solution sheared on top of the silicon, quartz, and silicon/perovskite, quartz/perovskite substrates at a blade speed of 2.5 mmps with a stage temperature of 90^o C. Thin films were kept on the heated stage for an additional 30 seconds to ensure complete solvent removal within the thin films. Solution shearing deposition conditions were held constant while varying only the perovskite ligand and ligand density.

Thin Film Characterization using polarized optical microscopy. A Zeiss Axio A.1 Microscope was utilized to observe morphology of TIPS-pentacene and TIPS-pentacene/perovskite thin films. Optical images were collected at 5x and 20x magnification under cross-polarized light.

Thickness measurements of thin films using stylus profilometry. A DektakXT stylus profilometer was used to quantify the thickness of the thin films with a stylus force of 5 mg.

Grazing incidence X-ray diffraction (GIXD). Diffraction patterns were collected at the SLAC National Accelerator Laboratory on the 11-3 beamline. Incident X-rays with an energy of 12.7 keV penetrated thin films while housed in a helium chamber at an angle of 0.15^{o} with respect to the substrate. Diffraction patterns were collected with the incident X-ray beam along the shearing direction and with a 90^{o} rotation with respect to the shearing direction. Data was collected using a two-dimensional Rayonix MX225 CCD area detector. Diffraction patterns were analyzed using a Matlab toolbox developed by Zhang Jiang called Grazing-incidence X-ray Scattering User interface (GIXSGUI).[42]

2.7 Contributions

Ashley Conley conducted structural measurements and performed analysis. Alex Chen and Stephanie Guthrie did preliminary work to determine feasibility of the project. Kevin Stone aided in the taking of grazing incidence X-ray diffraction measurements at SLAC. Gaurav Giri and Joshua Choi conceived the project.

2.8 References

(1) Brédas, J. L.; Calbert, J. P.; da Silva Filho, D. A.; Cornil, J. Organic Semiconductors: A Theoretical Characterization of the Basic Parameters Governing Charge Transport. *Proc Natl Acad Sci USA* **2002**, *99* (9), 5804. https://doi.org/10.1073/pnas.092143399.

(2) Ryno, S. M.; Risko, C.; Brédas, J.-L. Impact of Molecular Packing on Electronic Polarization in Organic Crystals: The Case of Pentacene vs TIPS-Pentacene. *J. Am. Chem. Soc.* **2014**, *136* (17), 6421–6427. https://doi.org/10.1021/ja501725s.

(3) Root, S. E.; Savagatrup, S.; Printz, A. D.; Rodriquez, D.; Lipomi, D. J. Mechanical Properties of Organic Semiconductors for Stretchable, Highly Flexible, and Mechanically Robust Electronics. *Chem. Rev.* **2017**, *117* (9), 6467–6499. https://doi.org/10.1021/acs.chemrev.7b00003.

(4) Wang, C.; Dong, H.; Jiang, L.; Hu, W. Organic Semiconductor Crystals. *Chem. Soc. Rev.* **2018**, *47* (2), 422–500. https://doi.org/10.1039/C7CS00490G.

(5) Diao, Y.; Lenn, K. M.; Lee, W.-Y.; Blood-Forsythe, M. A.; Xu, J.; Mao, Y.; Kim, Y.; Reinspach, J. A.; Park, S.; Aspuru-Guzik, A.; Xue, G.; Clancy, P.; Bao, Z.; Mannsfeld, S. C. B. Understanding Polymorphism in Organic Semiconductor Thin Films through Nanoconfinement. *J. Am. Chem. Soc.* **2014**, *136* (49), 17046–17057. https://doi.org/10.1021/ja507179d.

(6) Hudson, R. J.; Huang, D. M.; Kee, T. W. Anisotropic Triplet Exciton Diffusion in Crystalline Functionalized Pentacene. *J. Phys. Chem. C* **2020**. https://doi.org/10.1021/acs.jpcc.0c07608.

(7) Buchanan, E. A.; Kaleta, J.; Wen, J.; Lapidus, S. H.; Císařová, I.; Havlas, Z.; Johnson, J. C.; Michl, J. Molecular Packing and Singlet Fission: The Parent and Three Fluorinated 1,3-Diphenylisobenzofurans. *J. Phys. Chem. Lett.* **2019**, *10* (8), 1947–1953. https://doi.org/10.1021/acs.jpclett.8b03875.

(8) Grieco, C.; Doucette, G. S.; Pensack, R. D.; Payne, M. M.; Rimshaw, A.; Scholes, G. D.; Anthony, J. E.; Asbury, J. B. Dynamic Exchange During Triplet Transport in Nanocrystalline

TIPS-Pentacene Films. *J. Am. Chem. Soc.* **2016**, *138* (49), 16069–16080. https://doi.org/10.1021/jacs.6b10010.

(9) Wu, Y.; Liu, K.; Liu, H.; Zhang, Y.; Zhang, H.; Yao, J.; Fu, H. Impact of Intermolecular Distance on Singlet Fission in a Series of TIPS Pentacene Compounds. *J. Phys. Chem. Lett.* **2014**, *5* (20), 3451–3455. https://doi.org/10.1021/jz5017729.

(10) Wang, X.; Garcia, T.; Monaco, S.; Schatschneider, B.; Marom, N. Effect of Crystal Packing on the Excitonic Properties of Rubrene Polymorphs. *CrystEngComm* **2016**, *18* (38), 7353–7362. https://doi.org/10.1039/C6CE00873A.

(11) Congreve Daniel N.; Lee Jiye; Thompson Nicholas J.; Hontz Eric; Yost Shane R.; Reusswig Philip D.; Bahlke Matthias E.; Reineke Sebastian; Van Voorhis Troy; Baldo Marc A. External Quantum Efficiency Above 100% in a Singlet-Exciton-Fission–Based Organic Photovoltaic Cell. *Science* **2013**, *340* (6130), 334–337. https://doi.org/10.1126/science.1232994.

(12) Pazos-Outón, L. M.; Lee, J. M.; Futscher, M. H.; Kirch, A.; Tabachnyk, M.; Friend, R. H.; Ehrler, B. A Silicon–Singlet Fission Tandem Solar Cell Exceeding 100% External Quantum Efficiency with High Spectral Stability. *ACS Energy Lett.* **2017**, *2* (2), 476–480. https://doi.org/10.1021/acsenergylett.6b00678.

(13) Rao, A.; Friend, R. H. Harnessing Singlet Exciton Fission to Break the Shockley–Queisser Limit. *Nature Reviews Materials* **2017**, *2* (11), 17063. https://doi.org/10.1038/natrevmats.2017.63.

(14) Grieco, C.; Doucette, G. S.; Munro, J. M.; Kennehan, E. R.; Lee, Y.; Rimshaw, A.; Payne, M. M.; Wonderling, N.; Anthony, J. E.; Dabo, I.; Gomez, E. D.; Asbury, J. B. Triplet Transfer Mediates Triplet Pair Separation during Singlet Fission in 6,13-Bis(Triisopropylsilylethynyl)-Pentacene. *Advanced Functional Materials 27* (46), 1703929. https://doi.org/10.1002/adfm.201703929.

(15) Pensack, R. D.; Tilley, A. J.; Parkin, S. R.; Lee, T. S.; Payne, M. M.; Gao, D.; Jahnke, A. A.; Oblinsky, D. G.; Li, P.-F.; Anthony, J. E.; Seferos, D. S.; Scholes, G. D. Exciton

Delocalization Drives Rapid Singlet Fission in Nanoparticles of Acene Derivatives. *J. Am. Chem. Soc.* **2015**, *137* (21), 6790–6803. https://doi.org/10.1021/ja512668r.

(16) Li, Y.; Ji, D.; Liu, J.; Yao, Y.; Fu, X.; Zhu, W.; Xu, C.; Dong, H.; Li, J.; Hu, W. Quick Fabrication of Large-Area Organic Semiconductor Single Crystal Arrays with a Rapid Annealing Self-Solution-Shearing Method. *Scientific Reports* **2015**, *5* (1), 13195. https://doi.org/10.1038/srep13195.

(17) Giri, G.; Verploegen, E.; Mannsfeld, S. C. B.; Atahan-Evrenk, S.; Kim, D. H.; Lee, S. Y.; Becerril, H. A.; Aspuru-Guzik, A.; Toney, M. F.; Bao, Z. Tuning Charge Transport in Solution-Sheared Organic Semiconductors Using Lattice Strain. *Nature* **2011**, *480*, 504.

(18) Diao, Y.; Tee, B. C.-K.; Giri, G.; Xu, J.; Kim, D. H.; Becerril, H. A.; Stoltenberg, R. M.; Lee, T. H.; Xue, G.; Mannsfeld, S. C. B.; Bao, Z. Solution Coating of Large-Area Organic Semiconductor Thin Films with Aligned Single-Crystalline Domains. *Nature Materials* **2013**, *12*, 665.

(19) Guthrie, S. M.; Smilgies, D.-M.; Giri, G. Controlling Polymorphism in Pharmaceutical Compounds Using Solution Shearing. *Crystal Growth & Design* **2018**, *18* (2), 602–606. https://doi.org/10.1021/acs.cgd.7b01686.

(20) Fusella, M. A.; Yang, S.; Abbasi, K.; Choi, H. H.; Yao, Z.; Podzorov, V.; Avishai, A.; Rand, B. P. Use of an Underlayer for Large Area Crystallization of Rubrene Thin Films. *Chem. Mater.* **2017**, *29* (16), 6666–6673. https://doi.org/10.1021/acs.chemmater.7b01143.

(21) Li, Y.; Wan, J.; Smilgies, D.-M.; Bouffard, N.; Sun, R.; Headrick, R. L. Nucleation and Strain-Stabilization during Organic Semiconductor Thin Film Deposition. *Nature Scientific Reports* **2016**, *6* (1), 32620. https://doi.org/10.1038/srep32620.

(22) Zhu, X.; Zhang, X.; Huang, L.; Wang, Z.; Chi, L. Improving the Performance of TIPS-Pentacene Thin Film Transistors via Interface Modification. *Chemical Research in Chinese Universities* **2018**, *34* (1), 151–154. https://doi.org/10.1007/s40242-017-7122-x.

(23) Chen, J.; Cai, X.; Yang, D.; Song, D.; Wang, J.; Jiang, J.; Ma, A.; Lv, S.; Hu, M. Z.; Ni, C. Recent Progress in Stabilizing Hybrid Perovskites for Solar Cell Applications. *Journal of Power Sources* **2017**, *355*, 98–133. https://doi.org/10.1016/j.jpowsour.2017.04.025.

(24) Ito, Y.; Virkar, A. A.; Mannsfeld, S.; Oh, J. H.; Toney, M.; Locklin, J.; Bao, Z. Crystalline Ultrasmooth Self-Assembled Monolayers of Alkylsilanes for Organic Field-Effect Transistors. *J. Am. Chem. Soc.* **2009**, *131* (26), 9396–9404. https://doi.org/10.1021/ja9029957.

(25) McDowell, M.; Hill, I. G.; McDermott, J. E.; Bernasek, S. L.; Schwartz, J. Improved Organic Thin-Film Transistor Performance Using Novel Self-Assembled Monolayers. *Appl. Phys. Lett.* **2006**, *88* (7), 073505. https://doi.org/10.1063/1.2173711.

(26) Kelley, T. W.; Boardman, L. D.; Dunbar, T. D.; Muyres, D. V.; Pellerite, M. J.; Smith, T. P. High-Performance OTFTs Using Surface-Modified Alumina Dielectrics. *J. Phys. Chem. B* **2003**, *107* (24), 5877–5881. https://doi.org/10.1021/jp034352e.

(27) Virkar, A.; Mannsfeld, S.; Oh, J. H.; Toney, M. F.; Tan, Y. H.; Liu, G.; Scott, J. C.; Miller, R.; Bao, Z. The Role of OTS Density on Pentacene and C60 Nucleation, Thin Film Growth, and Transistor Performance. *Advanced Functional Materials* **2009**, *19* (12), 1962–1970. https://doi.org/10.1002/adfm.200801727.

(28) Tan, H.; Jain, A.; Voznyy, O.; Lan, X.; García de Arquer, F. P.; Fan, J. Z.; Quintero-Bermudez, R.; Yuan, M.; Zhang, B.; Zhao, Y.; Fan, F.; Li, P.; Quan, L. N.; Zhao, Y.; Lu, Z.-H.; Yang, Z.; Hoogland, S.; Sargent, E. H. Efficient and Stable Solution-Processed Planar Perovskite Solar Cells via Contact Passivation. *Science* **2017**, *355* (6326), 722. https://doi.org/10.1126/science.aai9081.

(29) Gao, X.-X.; Luo, W.; Zhang, Y.; Hu, R.; Zhang, B.; Züttel, A.; Feng, Y.; Nazeeruddin, M. K. Stable and High-Efficiency Methylammonium-Free Perovskite Solar Cells. *Advanced Materials* **2020**, *32* (9), 1905502. https://doi.org/10.1002/adma.201905502.

(30) Min, H.; Lee, D. Y.; Kim, J.; Kim, G.; Lee, K. S.; Kim, J.; Paik, M. J.; Kim, Y. K.; Kim, K. S.; Kim, M. G.; Shin, T. J.; Il Seok, S. Perovskite Solar Cells with Atomically Coherent

Interlayers on SnO2 Electrodes. *Nature* **2021**, *598* (7881), 444–450. https://doi.org/10.1038/s41586-021-03964-8.

(31) Jing, H.; Peng, R.; Ma, R.-M.; He, J.; Zhou, Y.; Yang, Z.; Li, C.-Y.; Liu, Y.; Guo, X.; Zhu, Y.; Wang, D.; Su, J.; Sun, C.; Bao, W.; Wang, M. Flexible Ultrathin Single-Crystalline Perovskite Photodetector. *Nano Lett.* **2020**, *20* (10), 7144–7151. https://doi.org/10.1021/acs.nanolett.0c02468.

(32) Ahmadi, M.; Wu, T.; Hu, B. A Review on Organic–Inorganic Halide Perovskite Photodetectors: Device Engineering and Fundamental Physics. *Advanced Materials* **2017**, *29* (41), 1605242. https://doi.org/10.1002/adma.201605242.

(33) Chen, Q.; Wu, J.; Ou, X.; Huang, B.; Almutlaq, J.; Zhumekenov, A. A.; Guan, X.; Han, S.; Liang, L.; Yi, Z.; Li, J.; Xie, X.; Wang, Y.; Li, Y.; Fan, D.; Teh, D. B. L.; All, A. H.; Mohammed, O. F.; Bakr, O. M.; Wu, T.; Bettinelli, M.; Yang, H.; Huang, W.; Liu, X. All-Inorganic Perovskite Nanocrystal Scintillators. *Nature* **2018**, *561* (7721), 88–93. https://doi.org/10.1038/s41586-018-0451-1.

(34) Le Berre, M.; Chen, Y.; Baigl, D. From Convective Assembly to Landau−Levich Deposition of Multilayered Phospholipid Films of Controlled Thickness. *Langmuir* **2009**, *25* (5), 2554–2557. https://doi.org/10.1021/la803646e.

(35) Giri, G.; Li, R.; Smilgies, D.-M.; Li, E. Q.; Diao, Y.; Lenn, K. M.; Chiu, M.; Lin, D. W.; Allen, R.; Reinspach, J.; Mannsfeld, S. C. B.; Thoroddsen, S. T.; Clancy, P.; Bao, Z.; Amassian, A. One-Dimensional Self-Confinement Promotes Polymorph Selection in Large-Area Organic Semiconductor Thin Films. *Nat Commun* **2014**, *5*, 3573. https://doi.org/10.1038/ncomms4573.

(36) Mitzi, D. B. A Layered Solution Crystal Growth Technique and the Crystal Structure of (C6H5C2H4NH3)2PbCl4. *Journal of Solid State Chemistry* **1999**, *145* (2), 694–704. https://doi.org/10.1006/jssc.1999.8281.

(37) Braun, M.; Frey, W. Crystal Structure of Bis(Benzylammonium) Lead Tetrachloride, (C7H7NH3)2PbCl4. *Zeitschrift für Kristallographie - New Crystal Structures* **1999**, *214* (3), 331–332. https://doi.org/10.1515/ncrs-1999-0318.

(38) Du, K.; Tu, Q.; Zhang, X.; Han, Q.; Liu, J.; Zauscher, S.; Mitzi, D. B. Two-Dimensional Lead(II) Halide-Based Hybrid Perovskites Templated by Acene Alkylamines: Crystal Structures, Optical Properties, and Piezoelectricity. *Inorg. Chem.* **2017**, *56* (15), 9291–9302. https://doi.org/10.1021/acs.inorgchem.7b01094.

(39) Shibuya, K.; Koshimizu, M.; Nishikido, F.; Saito, H.; Kishimoto, S. Poly[Bis(Phenethylammonium) [Dibromidoplumbate(II)]-Di-μ-Bromido]]. *Acta Crystallographica Section E: Structure Reports Online* **2009**, *65*, m1323–m1324.

(40) Kamminga, M. E.; Fang, H.-H.; Filip, M. R.; Giustino, F.; Baas, J.; Blake, G. R.; Loi, M. A.; Palstra, T. T. M. Confinement Effects in Low-Dimensional Lead Iodide Perovskite Hybrids. *Chem. Mater.* **2016**, *28* (13), 4554–4562. https://doi.org/10.1021/acs.chemmater.6b00809.

(41) Giri, G.; Li, R.; Smilgies, D.-M.; Li, E. Q.; Diao, Y.; Lenn, K. M.; Chiu, M.; Lin, D. W.; Allen, R.; Reinspach, J.; Mannsfeld, S. C. B.; Thoroddsen, S. T.; Clancy, P.; Bao, Z.; Amassian, A. One-Dimensional Self-Confinement Promotes Polymorph Selection in Large-Area Organic Semiconductor Thin Films. *Nature Communications* **2014**, *5*, 3573.

(42) Jiang, Z. It GIXSGUI: A MATLAB Toolbox for Grazing-Incidence X-Ray Scattering Data Visualization and Reduction, and Indexing of Buried Three-Dimensional Periodic Nanostructured Films. *Journal of Applied Crystallography* **2015**, *48* (3), 917–926. https://doi.org/10.1107/S1600576715004434.

Chapter 3: Exploring optical properties, singlet fission, and interfacial structures of perovskite-templated TIPS-pentacene thin films

Contributors: Ashley M. Conley, Rachel A. Dziatko,* Karl S. Westendorff,* Anna Sviripa, Arthur E. Bragg, Christopher Paolucci, Joshua J. Choi, and Gaurav Giri*

* - equal contributions to the work presented in this Chapter (see Contributions section for details)

This chapter is in preparation for a manuscript submission.

3.1 Abstract

Singlet fission, a process by which one singlet exciton is down converted into two lower energy triplet excitons, is sensitive to the degree of electronic coupling within a molecular packing structure. Variations in molecular packing can be detrimental to triplet formation and triplet-triplet separation, ultimately affecting the harvesting of triplets for electricity in organic photovoltaics. Here, study the effect of molecular packing and structural ordering on the optoelectronic properties using the six phase-pure molecular packing structures of TIPS-pentacene that were isolated using two-dimensional lead halide perovskites. Transient absorption spectroscopy reveals that while triplet formation is fast (<100 fs) regardless of template structure, the increased ordering in perovskite-templated samples speeds up triplet-triplet separation and recombination, providing evidence that the benefits of phase-purity offset minor variations in molecular packing. Molecular dynamics modeling of the interface reveals that perovskite-templating allows for closer packing of TIPS-Pn molecules, regardless of perovskite structure. With an extensive number of molecule-perovskite pairings, this work provides a methodology to use ordered, periodic surfaces to elucidate structure-property relationships of small molecules to adjust optoelectronic responses, such as singlet fission.

3.2 Introduction

It is well-established that molecular packing and morphology affect singlet fission (SF), an exciton multiplication process whereby one singlet exciton is converted into two triplet excitons. Singlet fission has potential to overcome the Shockley-Queisser efficiency limit for solar cells, and thus understanding this process is of great scientific interest in the field of photovoltaics.[1,2] SF has been observed in many prominent acene-based OSC molecules, such as 6,13-triisoprolylethynyl pentacene (TIPS-pentacene), which satisfy the energetic requirement that the triplet state energy is less than or equal to half of the singlet state energy.[3,4] Studies have shown that SF rates, charge transfer couplings, and triplet state recombination rates are sensitive to micro and macroscopic properties of OSC thin films, such as molecular packing structures,[3,5–8] structural disorder,[5,9,10] and morphology.[6,11] Precise control of crystalline properties is still an active area of research, as optimizing SF properties could have profound ramifications for photovoltaics.

Here, we utilize six perovskite-templated structures of TIPS-pentacene to study the effect of molecular packing on optoelectronic properties. We show that reduced structural disorder for perovskite-templated structures results in similar optoelectronic behavior. Minor variations in molecular interactions result in slight shifts in the π-π stacking absorbance feature. However, the photoluminescence of perovskite-templated samples reveals significant quenching, suggesting that the relaxation dynamics have been altered. We then measure singlet fission rates and triplet state lifetimes using transient absorption spectroscopy and show that increased ordering in molecular packing is essential for rapid triplet-triplet separation and transport, which is required to ultimately harness the triplets for electricity. Finally, molecular dynamics simulations of TIPS-pentacene/perovskite interfaces reveal structural changes to TIPS-pentacene molecular packing that are qualitatively consistent with diffraction data and suggest that reduced π-π stacking

distances for perovskite-templated structures is a possible explanation for the observation of similar optoelectronic behavior for different perovskite-templated structures.

3.3 Results and Discussion

3.3.1 Steady-state optical properties of perovskite-templated TIPS-pentacene

TIPS-pentacene crystallizes in a triclinic unit cell with P1 symmetry with a 2D brick-wall structure. Changes to the (101) plane spacing affects electronic interactions between TIPS-pentacene molecules through changes in the π-π stacking distances and molecular offset of pentacene backbones, as depicted in **Fig. 3.1.** The π-stacking interactions take place between two TIPS-pentacene molecular pairs[12] and transverse anisotropically in the **a** and **b** lattice directions, resulting in a two-dimensional, direction-dependent delocalization of lowest energy excitons.[3]

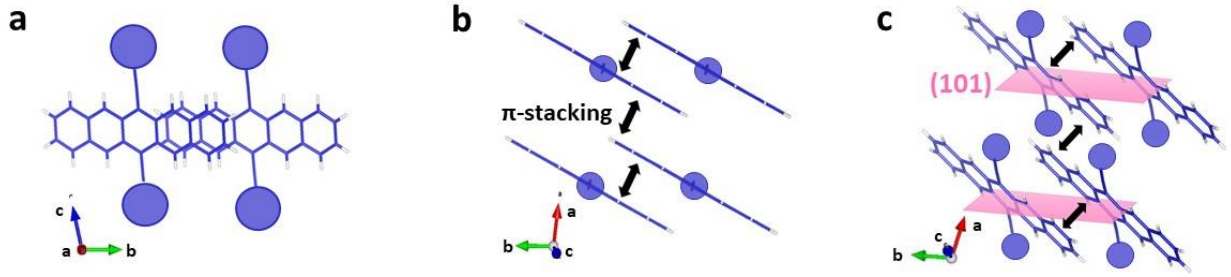

Figure 3.1. Schematic of the relationship between π-stacking of TIPS-pentacene molecules and the (101) plane. The overall π-π interactions will be affected by π-stacking distances and molecular offset of pentacene backbones. **a**) Depiction of the molecular offset of the TIPS-pentacene backbones whereby slight variations will result in changes π interactions through enhanced or diminished face-to-face versus slipped π-stacking. **b**) Depiction of the π-stacking distance between TIPS-pentacene molecules. **c**) Depiction of the (101) plane (pink) showing that variations in the plane spacing will result in changes in π-stacking (black arrows).

Small changes in π-stacking interactions can dramatically alter electronic interactions between molecules. Due to the limited number of reflections in our grazing incidence diffraction patterns from TIPS-pentacene (i.e. without perovskite diffraction peak overlapping), we do not have a well-defined structure with which to perform first principles calculations to directly elucidate structure-property relationships. Even with these limitations, intermolecular interactions

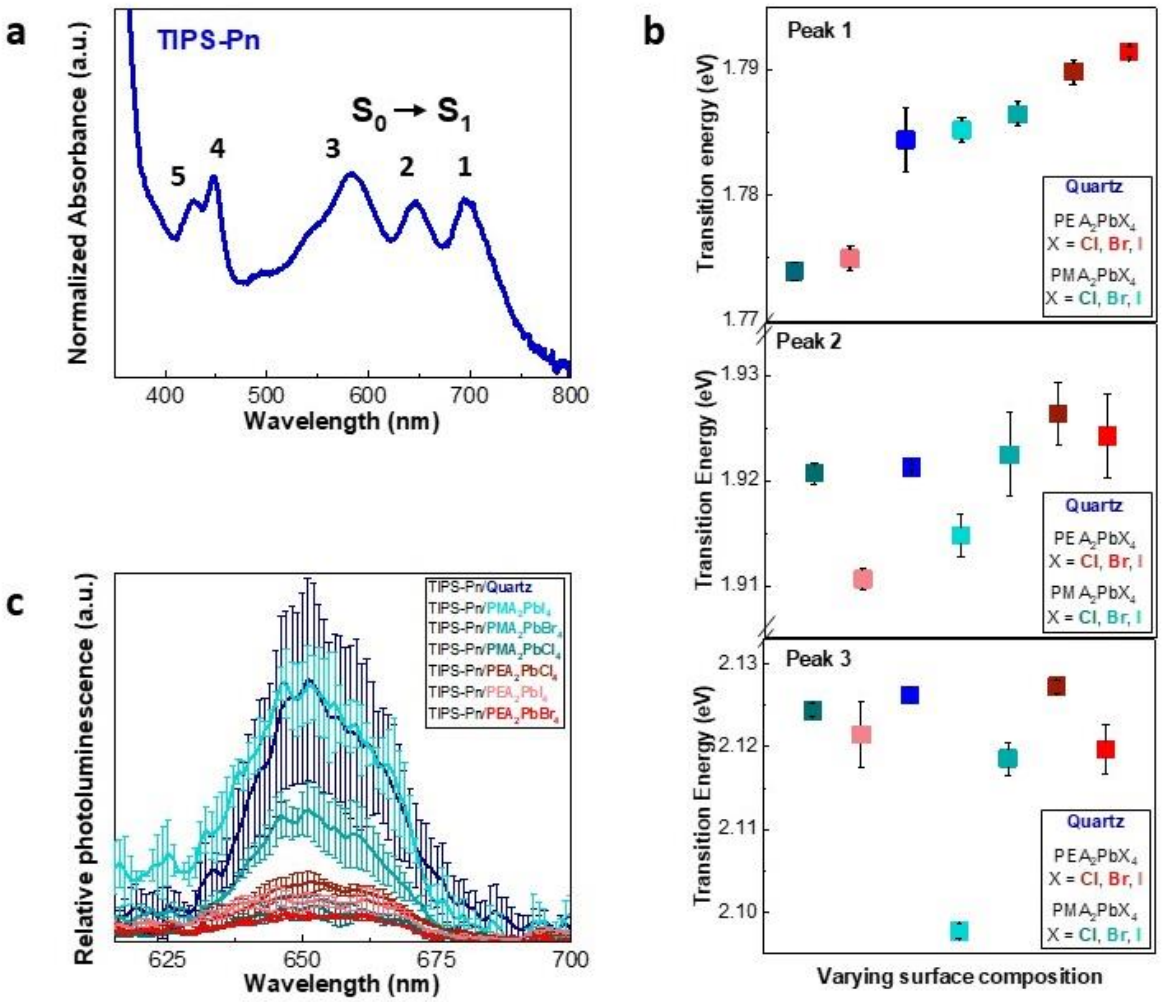

Figure 3.2. Steady state optical characterization of perovskite-templated TIPS-pentacene. **a)** Absorbance spectrum of TIPS-pentacene thin film showing vibronic progression of lowest energy $S_0 \rightarrow S_1$ transition (peaks 1, 2, and 3) and intramolecular transitions (peaks 4 and 5). **b)** Transition energies of π-π stacking absorbance peak (peak 1) of TIPS-pentacene with varying perovskite surface and the next two lowest energy transitions (peaks 2 and 3). **c)** Photoluminescence of TIPS-pentacene thin films.

can be compared for these perovskite-templated molecular packing structures through analysis of the π-stacking absorption feature and photoluminescence intensity signals.

Optical properties of perovskite-templated TIPS-pentacene structures were studied using UV-Vis spectroscopy. The lowest-energy transitions between 500 and 750 nm are associated with the $S_0 \rightarrow S_1$ transition of TIPS-pentacene,[13] as labeled as peaks 1, 2, and 3 in **Fig. 3.2a**. The $S_0 \rightarrow S_1$ multi-peak signature has been attributed to vibrational progression of the lowest energy transition as well as a delocalization of multiple nearly-degenerate energy levels arising from intermolecular excitations, while peaks 4 and 5 arise from intramolecular excitation.[3,14] Because $S_0 \rightarrow S_1$ transitions are below the bandgaps of the perovskites, the lowest-energy TIPS-pentacene absorbance peaks could be isolated. All TIPS-pentacene thin films exhibit an absorbance peak near 700 nm, denoted as peak 1, which corresponds to a red-shifted absorbance feature arising from π-π stacking of TIPS-pentacene molecules in the solid state that is not present in solution state spectra.[15] Incremental changes to the π-stacking transition energy were observed with a maximum energy difference of 0.015 eV when varying the perovskite surface (**Fig. 3.2b**, *top*), which suggests slight variations in the degree of π-stacking interactions and is consistent with our structural findings. The transition energies of peak 2 and 3 also showed differences in transition energies, but in contrast to the more discrete transition energies of peak 1, multiple samples exhibited overlapping transition energies (**Fig. 3.2b**, *middle/bottom*). Sharifzadeh, S. et al showed in ordered domains of TIPS-pentacene that peak 2 is composed of a blending of nearly-degenerate states while peak 1 is more strongly associated to one first singlet excited state arising from π-stacking,[3] which may explain the overlapping transition energies of peak 2. Peaks 4 and 5 show minor variations in transition energy, which is consistent with an intramolecular excitation that would be less affected by π-π intermolecular interactions (**Fig. 3.3**).

Steady-state photoluminescence (PL) measurements of TIPS-pentacene thin films are shown in **Fig. 3.2c**. TIPS-pentacene thin films were selectively excited with 560 nm light, which is below the bandgap of perovskites. All TIPS-pentacene thin films exhibited weak PL intensity with only one observable peak at ~650 nm, which is consistent with literature.[16] Perovskite-templated TIPS-pentacene samples exhibited reduced PL intensity relative to untemplated samples, suggesting that relaxation dynamics have been altered in more-ordered TIPS-pentacene films. Nui, M et al. showed that TIPS-pentacene exhibits more intense PL in disordered or amorphous regions due to disruptions in intermolecular interactions and exhibits reduced PL in regions with increased crystallinity.[17] Our results are consistent with literature in that perovskite-templated structures exhibited increased ordering and a subsequent reduction in PL. Our results provide evidence that regardless of minor variations in perovskite-templated TIPS-pentacene structure, increased ordering plays a substantial role in enhancing intermolecular interactions.

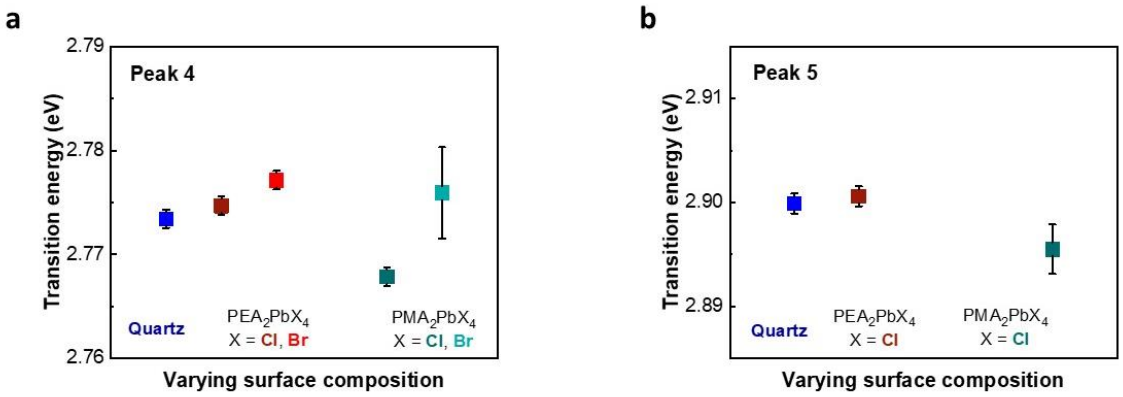

Figure 3.3. Absorbance of intramolecular transition peaks **a**) 4 and **b**) 5).

3.3.2 Singlet fission of perovskite-templated TIPS-pentacene thin films

Transient absorption (TA) spectroscopy was used to investigate singlet fission dynamics in perovskite-templated and untemplated TIPS-pentacene films. **Fig. 3.4** shows a depiction of the excitation process followed by triplet state formation. TIPS-pentacene molecules were excited with 700 nm light to form the singlet state, The singlet state then forms a triplet-triplet correlated pair through an energy splitting of the singlet state energy through intermolecular interactions between TIPS-pentacene molecules. Finally, the correlated triplet-triplet pair separates into two individual, de-coupled triplets. TA spectra were dominated by a feature peaking near 530 nm that is characteristic of the $T_1 \rightarrow T_N$ transition for triplet pairs in TIPS-pentacene (**Fig. 3.5a**).[18–20]

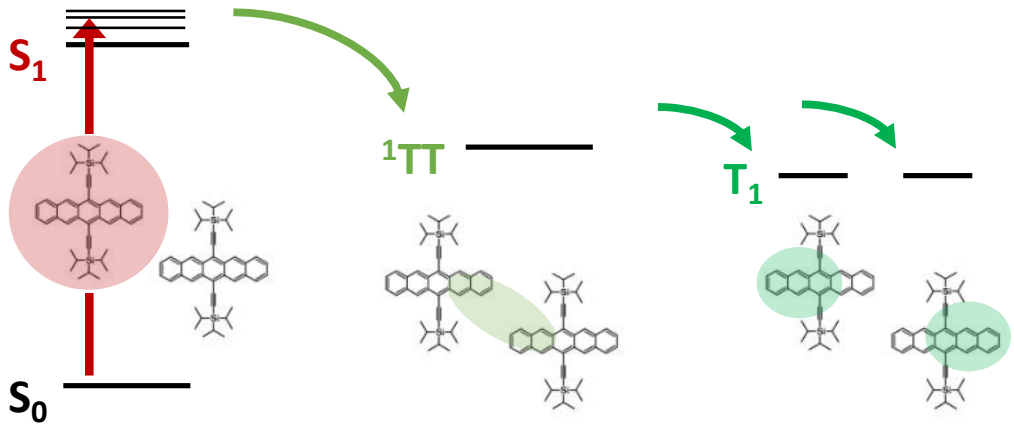

Figure 3.4. Schematic showing the singlet exciton (red) forming the triplet-triplet correlated pair (light green) before splitting into two triplet excitons (green).

Because TA spectra of TIPS-pentacene samples on PMA_2PbI_4 and PEA_2PbI_4 perovskite templates were complicated by direct excitation of the perovskite, we were unable to isolate singlet-fission/triplet-pair dynamics for these samples. All TIPS-pentacene films exhibited

ultrafast generation of triplet-triplet pairs via singlet fission ($S_1S_0 \rightarrow {}^1(TT)$), as evidenced by the rapid appearance of the triplet-pair absorption feature on a timescale commensurate with our experimental time resolution (**Fig. 3.5b**), consistent with previous reports.[18] Accurate determination of this timescale is inhibited by a coherent artifact arising from nonlinear optical interactions in the substrate during the period of pulse-pair overlap. The $T_1 \rightarrow T_n$ transition peak continues to rise and redshifts by ~2 nm in the picoseconds following excitation. This behavior is consistent with signatures of triplet-pair separation (${}^1TT \rightarrow {}^1T..T$).[18] The triplet feature begins to decay over the next nanosecond, which we attribute to triplet recombination ($T + T \rightarrow 2S_0$).

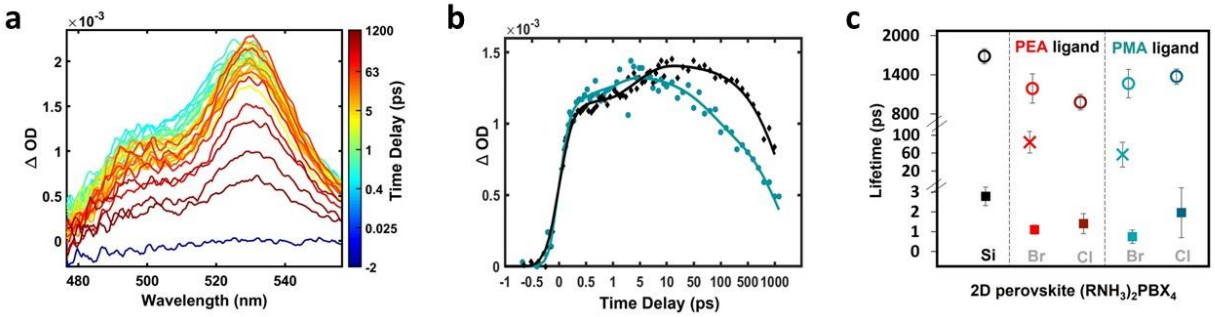

Figure 3.5. a) Transient absorption spectra of TIPS-pentacene on PEA_2PbCl_4 excited at 700 nm (~700 μJ/cm^2). **b)** Transient absorption at 525 nm following 700 nm photoexcitation of TIPS-pentacene on silica (black diamonds) and PMA_2PbBr_4 (green circles). Fits from global spectral analysis are plotted as solid lines. Data are plotted on a linear timescale from 0 to 1 ps and logarithmic from 1 to 100 ps. **c)** Triplet separation lifetimes (solid squares) and annihilation lifetimes (fast decay, X; slow decay open circles) with associated errors for TIPS-pentacene on perovskites and silica.

TA spectral evolution was analyzed by global spectral analysis (see Materials and methods). Transients at a probe wavelength of 525 nm are presented in **Fig. 3.5b**. All templated TIPS-pentacene exhibited both faster triplet-pair separation and recombination kinetics when

compared to the untemplated control. A summary of the triplet-pair separation and recombination timescales are summarized in **Fig. 3.5 and 3.6.** For the control sample, triplet-pair separation occurs on a timescale of 2.7 ± 0.6 picoseconds, which is consistent with the previously reported timescale (2.5 picoseconds) measured for Form I TIPS-pentacene.[18] In contrast, triplet-pair separation speeds up by a factor greater than two in perovskite-templated samples. Species-associated differential spectra (SADS) obtained from global fits all show that absorption features shift on these timescales and supports that this is associated with the same photophysical process in all samples.

Triplet recombination is also observed to be faster for templated samples. For the Br-based templates, recombination behavior was best fit using a biexponential decay; notably, SADS for both components in each fit have the same spectral shape. We note that recombination is somewhat faster than what has been reported[20] previously for amorphous and crystalline TIPS-pentacene; this is most likely a consequence of the slightly higher fluence needed to conduct our

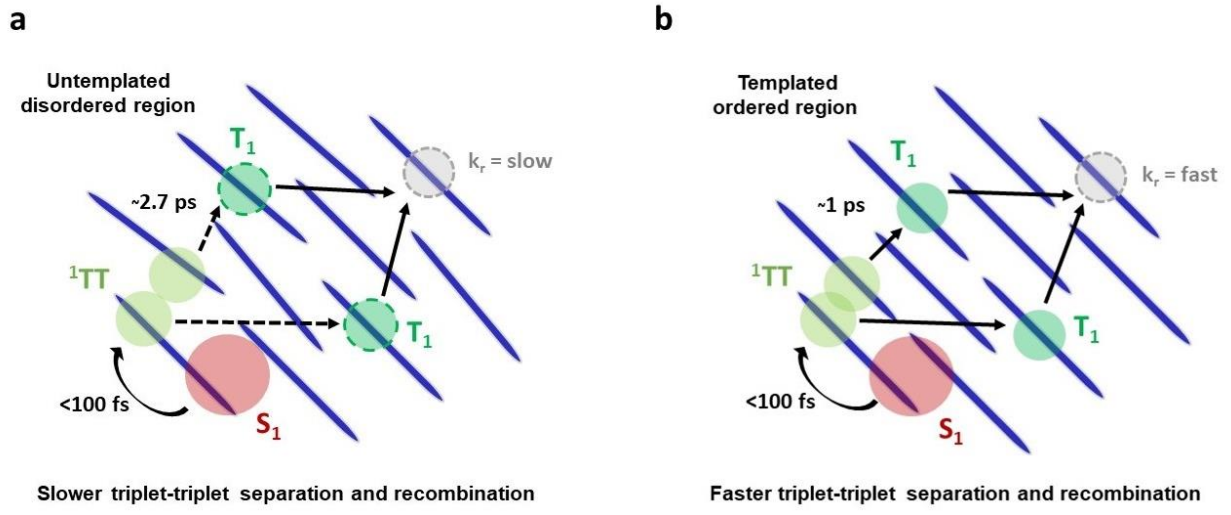

Figure 3.6. a) Diagram of untemplated/disordered and **b)** perovskite-templated/ordered regions of TIPS-pentacene showing that enhanced phase-purity (i.e. reduced disorder) leads to faster timescales for triplet-triplet separation and recombination.

measurements. The triplet decay lifetime decreases considerably for our samples at even higher fluences. Triplet decay observed at lowest fluences were observed to be on similar timescales reported from measurements at lower excitation fluences.[18]

The kinetics of triplet-pair generation and the separation, decoherence, diffusion, and recombination of triplets is well-known to be sensitive to the details of intermolecular interactions.[21] Various studies have shown that the rate of singlet fission is correlated with the degree of lateral slip stacking along the chromophore axis that enhances intermolecular orbital coupling.[11,22] Triplet-pair generation in TIPS-pentacene films is generally quite fast and efficient, such that little to no impact is expected for modest changes in packing structure. Notably, Pensack et. al recently showed that modified TIPS-pentacene with almost no lateral slip resulting in pairwise packing negatively impacts the survival of triplet-pairs due to fast (< 2-4 picoseconds) nonadiabatic quenching, but that rapid triplet-pair generation is maintained.[8,19] We observed no significant difference in the rate of triplet-pair generation in our films (in both cases, it occurs on ~100 fs timescales or faster), which is consistent with these previous observations.

In contrast, triplet-pair separation and recombination, which occur on slower timescales, are highly sensitive to impacts of crystal structure on intermolecular triplet energy transfer. A previous study revealed that the triplet annihilation is much faster in crystalline versus amorphous films due to increased diffusivity of triplet excitons, such that faster triplet transfer timescales may be expected with a general increase in the crystallinity of films.[20] In addition, Grieco et. al. reported that Form I TIPS-pentacene films have faster triplet-pair separation kinetics than Form II films due to improved intermolecular orbital interactions in Form I that facilitate faster site-to-site triplet transfer.[18] Similarly, Doucette et al. demonstrated that the triplet-separation rate can be increased when polycrystalline films are compressed in a diamond anvil cell, as compression induces

packing modifications that increase pair-wise charge-transfer interactions.[23] We note that the spacing parameter for templated films span a range relative to that of the untemplated TIPS-pentacene, yet all templated films exhibit similar triplet transfer dynamics. This behavior is consistent with the rate of triplet transfer dynamics being dominated by the degree of packing order, rather than modifications to pair-wise interactions.

The faster triplet-pair separation and triplet-recombination lifetimes observed with templated vs. untemplated TIPS-pentacene structures are consistent with both an increase in packing order and enhanced intermolecular interactions arising from shorter π-π distances that facilitate triplet transfer which result from templating TIPS-pentacene on perovskite surfaces. Interestingly, we observe that templating further increases the rate of triplet-pair separation relative to untemplated crystalline TIPS-pentacene under ambient conditions, highlighting that this approach can be used to affect enhanced triplet-energy transfer as is needed to ultimately harvest triplets in materials applications.

3.3.3. Simulated annealing of TIPS-pentacene/perovskite interfaces

We employed molecular dynamics (MD) simulations to better understand the structural origins of the singlet fission behavior of perovskite-templated TIPS-pentacene. The MD simulations were run in the OpenMM software using the AMOEBA (Atomic multipole optimized energetics for biomolecular applications) polarizable forcefield,[24,25] which is capable of simulating charge evolution at inorganic interfaces, including perovskites.[24] After developing forcefield parameters which recovered the bulk properties of TIPS-pentacene and each perovskite, we generated initial periodic interfaces by lattice matching TIPS-pentacene with perovskite **a** and **b** cell parameters. To further optimize the **a** and **b** cell parameters of the interface, we ran anisotropic simulated annealing NPT simulations. The optimal cell parameters were then used in simulated

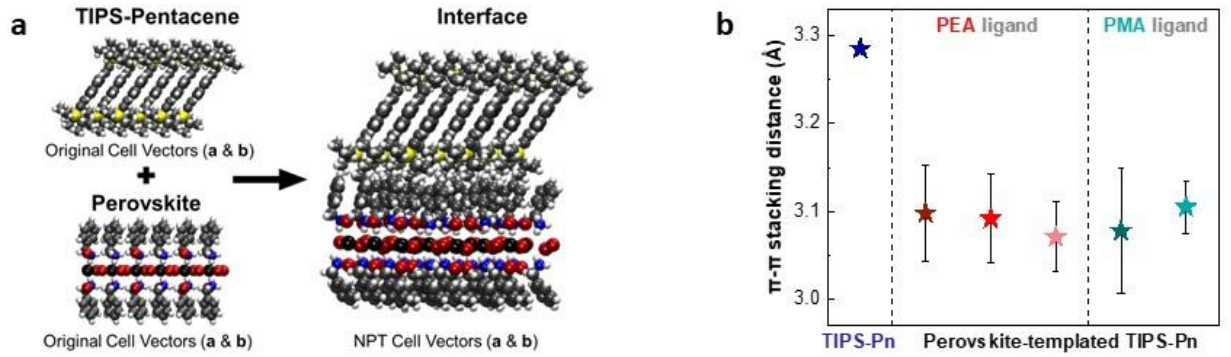

Figure 3.7. Molecular dynamics simulations of the TIPS-Pn/perovskite interface. **a)** Reaction scheme of TIPS-Pn and perovskite structures. **b)** Calculated π-π stacking distances for bulk TIPS-Pn and each TIPS-Pn/perovskite interfaces. Bulk TIPS-Pn π-π stacking distance is of the reported Form I structure.

annealing NVT simulations to identify low energy structural minima for each interface (**Fig. 3.7a**, additional simulation details in Methods). We could not identify minima for the $(PMA)_2PbI_4$ interface because the large lattice mismatch between TIPS-pentacene and $(PMA)_2PbI_4$ perovskite resulted in a supercell too large for MD simulations.

To validate our computational methods, we compared the simulated and experimentally observed values of (101) spacings. MD simulations qualitatively recovered the experimental trends in TIPS-pentacene d-spacing (described in detail in Chapter 2), but were systematically lower than experimental values. Using the experimental TIPS-pentacene (101) spacing as a reference, MD simulations correctly predict the (101) spacing trend observed using PEA-terminated perovskite interfaces, with higher and lower distortion of the TIPS-pentacene lattice for PEA_2PbCl_4 and PEA_2PbBr_4, respectively, and PEA_2PbI_4 in-between. Calculated (101) spacings for $(PMA)_2PbCl_4$ and $(PEA)_2PbBr_4$ were within 0.004 Å, in agreement with experiment (Fig. 2d). While our models do not represent the full complexity of the real interfaces, they recover the experimental trends in (101) spacings, suggesting that the parameters dictating structural changes (i.e. interfacial lattice sizes and intermolecular interactions) are effectively captured.

The large number of atoms in these interfaces prohibited accurate band structure calculations of these materials. However, previous studies on acene-based molecules demonstrate a strong correlation between π-π stacking distances and charge transfer character. A reduction in π-π stacking distances of pentacene molecules has been shown to increase delocalization over multiple molecules and also increase charge transfer character,[3] which has been assigned as the mechanism for triplet-triplet separation for TIPS-pentacene.[18] We proceeded to compute TIPS-pentacene π-π stacking distances using MD interfacial structures as a proxy for singlet fission behavior. **Fig. 3.7b** shows that all perovskite-templated TIPS-Pn structures relaxed to shorter π-π stacking distances compared to the bulk phase and that all π-π stacking distances for the interfaces were similar, despite differences in (101) spacings. These crystal structure changes can occur via a lengthened **c** vector in the templated TIPS-pentacene structure and/or a difference in TIPS-pentacene molecular tilt with respect to the a-b plane. Our experimental data corroborates this, as diffraction data indicates changes in both **a** and **c** axes of perovskite-templated samples (**Fig. 2.10f-g** in Chapter 2). With all considered, the faster triplet-triplet separation and recombination observed using TA spectroscopy is consistent with expected outcomes for enhanced intermolecular interactions and increased triplet energy transfer that occurs from shorter π-π stacking distances (observed using MD) and increased ordering (observed using GIXD). We conclude that perovskite-templating allows for improved intermolecular interactions by means of closer packing of TIPS-pentacene molecules in conjunction with increased molecular ordering.

3.4 Conclusion

Singlet fission, an exciton multiplication process, is dictated by the degree of electronic coupling between molecules. While triplet state formation via singlet fission can be robust against minor variations in molecular packing, triplet-triplet separation and diffusion are acutely sensitive to such regions, altering the likelihood that triplets can be harvested for electricity in photovoltaic devices. However, reducing structural disorder in molecular packing structures has been an ongoing challenge for researchers in the field. We utilize our easy-to-adopt method to reduce structural disorder of TIPS-pentacene using 2D perovskites as tunable, crystalline interfaces to quantify the effects of phase purity and reduced disorder through comparison of perovskite-templated and untemplated TIPS-pentacene molecular packing structures. Here, we employed six phase-pure molecular packing structures of TIPS-pentacene to study structure-property relationships. With enhanced phase-purity, triplet-triplet separation and recombination occurred on faster timescales, indicating improved triplet energy transfer. Using molecular dynamics, we show that the π-π stacking distances are reduced as a result of perovskite-templating and allows for improved intermolecular interactions. Researchers have established a direct link between singlet fission and structural, morphological, and heterogeneous features. Recent reports have repeatedly emphasized the importance of phase purity to efficiently separate triplets. However, without methods to achieve phase-pure structures, singlet fission remains limited in application. Perovskite-templating could prove beneficial to apply to small molecules that undergo singlet fission on longer timescales. Perovskite-templating could be used to enhance intermolecular interactions and increase singlet fission rates, triplet-triplet separation, and triplet diffusivity in addition to fundamental studies to elucidate structure-property relationships via the fine tuning of molecular packing structures.

3.5 Materials and Methods

Optical characterization using UV-Vis and steady-state photoluminescence spectroscopy.

Photoluminescence was measured using a PTI QuantaMaster 400 spectrofluorometer equipped with two detectors, a R2658 Visible PMT detector and H10330-75 PMT NIR detector, and a Xe arc lamp excitation source. An excitation wavelength of 560 nm was used to selectively excite the TIPS-pentacene thin films only by using a wavelength that is below the threshold energy required to excite perovskites used in this study. A 560 bandpass filter (FWHM = 10 nm) was used for the excitation light and a 570 nm longpass filter was used for the emission. Background arising from the substrate was subtracted from each spectrum. Absorbance spectra were collected using a PerkinElmer UV/Vis/NIR Lambda 950S spectrometer with an integrating sphere.

Ultra-fast transient absorption spectroscopy to measure singlet fission rates.

The setup for our transient absorption measurements has been described in detail previously[1,2] and here we describe experimental details for the work presented. Ultrafast excitation and probe pulses were generated using the amplified output of a Ti:sapphire laser (Coherent Legend Elite, 3.8 mJ/pulse, 1 kHz repetition rate, ~35 fs pulse duration). Excitation pulses at 700 nm were obtained through second harmonic generation of the NIR signal obtained from an optical parametric amplifier (OPA, Coherent OperaSolo). Broadband probe pulses were obtained via white light generation in a 2 mm calcium fluoride crystal. Probe pulses were passed through a wire-grid polarizer (Thorlabs) set at the magic angle (54.7°) with respect to the pump pulse polarization and placed immediately before the sample to eliminate time-dependent polarization effects. The pump and probe beams were coaligned to the sample films which were sealed inside a lens tube flushed with argon, in order to prevent photooxidation during the experiments.

TA measurements were conducted with a 700 nm excitation wavelength (~700 μJ/cm^2), which is resonant with the lowest energy feature observed by UV/Vis, and a broad-band white-light probe; the time resolution of our experiments was ~150 fs, and triplet kinetics were monitored out to 1200 ps. Sample films were kept under argon to avoid photo-oxidation and were translated side-to-side by < 1 mm in a direction perpendicular to the incident laser beam throughout data acquisition in order to eliminate the potential for photodegradation. Each scan encompassed 15-20 accumulations which translates across the entire thin film, which removes any effects arising from heterogeneity in the thin films. A vertically polarized pump was aligned parallel to the π-stacking axis (the *a*-axis of the unit cell), with the probe polarization set to magic angle with respect to that of the pump. Additional experimental details are provided in the Methods Section and the Supporting Information.

TA spectral evolution was analyzed in more detail by global spectral analysis.[7] Global analysis assumed a kinetic model involving time-resolution-limited appearance of triplet pairs, kinetic interconversion to separated pairs on the timescale τ_{sep}, and single or biexponential recombination (τ_{rec}), as captured by the Equation below:

$$^1(TT) \xrightarrow{\tau_{sep}} {}^1(T\cdots T) \xrightarrow{\tau_{rec}} 2S_0$$

Kinetic models were convoluted with the instrument time-resolution. Global fits and species associated difference spectra (SADS) obtained from global spectral analysis were reasonably fit were obtained in all cases.

Molecular dynamics and simulated annealing using AMEOBA [24–26]

AMOEBA forcefield parameters were either generated via previously outlined procedures or referenced from previous works. Initial structures for perovskites and TIPS-pentacene were developed using previously published crystal structures, as referenced in Chapter 2. Forcefield parameters were validated by NPT simulations of bulk TIPS-pentacene and perovskite structures to verify that they recovered experimental densities.

All MD simulations were run in OpenMM[27] with CPU acceleration. All NPT MD simulations used a Verlet Integrator with timesteps of 0.5 fs, and NVT simulations used a Langevin integrator with a timestep of 0.5 fs. Constant-temperature simulations used an Andersen thermostat with a collision frequency of 1 ps, and constant pressure simulations used a Monte Carlo anisotropic barostat. Nonbonding cutoffs were set to 1.05 nm to avoid errors with the fluctuating box size. Periodic boundary conditions were enforced and the Particle Mesh Ewald (PME) method and a mutual polarization scheme was employed with a 10^{-5} tolerance.

Simulated annealing NVT simulations started by optimizing the interface guess structure and initializing the simulation at 500 K. A friction coefficient of 1 ps^{-1}, and an initial temperature of 500 K was used. After 5 ps, the temperature of the simulation was lowered by 33.33 K every 0.25 ps for 10 ps. Simulated annealing NPT simulations used these same parameters. At the end of simulated annealing, the final structure was then optimized, and (101) spacing and π-π stacking distances were computed.

3.6 Contributions

Singlet fission measurements and analysis was performed by Rachel Dziatko and Dr. Arthur E. Bragg at Johns Hopkins University. Molecular dynamics simulations and analysis was performed by Karl Westendorff, Anna Sviripa, and Dr. Christopher Paolucci at the University of Virginia.

3.7 References

(1) Pazos-Outón, L. M.; Lee, J. M.; Futscher, M. H.; Kirch, A.; Tabachnyk, M.; Friend, R. H.; Ehrler, B. A Silicon–Singlet Fission Tandem Solar Cell Exceeding 100% External Quantum Efficiency with High Spectral Stability. *ACS Energy Lett.* **2017**, *2* (2), 476–480. https://doi.org/10.1021/acsenergylett.6b00678.

(2) Congreve Daniel N.; Lee Jiye; Thompson Nicholas J.; Hontz Eric; Yost Shane R.; Reusswig Philip D.; Bahlke Matthias E.; Reineke Sebastian; Van Voorhis Troy; Baldo Marc A. External Quantum Efficiency Above 100% in a Singlet-Exciton-Fission–Based Organic Photovoltaic Cell. *Science* **2013**, *340* (6130), 334–337. https://doi.org/10.1126/science.1232994.

(3) Sharifzadeh, S.; Wong, C. Y.; Wu, H.; Cotts, B. L.; Kronik, L.; Ginsberg, N. S.; Neaton, J. B. Relating the Physical Structure and Optoelectronic Function of Crystalline TIPS-Pentacene. *Advanced Functional Materials 25* (13), 2038–2046. https://doi.org/10.1002/adfm.201403005.

(4) Broch, K.; Dieterle, J.; Branchi, F.; Hestand, N. J.; Olivier, Y.; Tamura, H.; Cruz, C.; Nichols, V. M.; Hinderhofer, A.; Beljonne, D.; Spano, F. C.; Cerullo, G.; Bardeen, C. J.; Schreiber, F.

Robust Singlet Fission in Pentacene Thin Films with Tuned Charge Transfer Interactions. *Nature Communications* **2018**, *9* (1), 954. https://doi.org/10.1038/s41467-018-03300-1.

(5) Grieco, C.; Doucette, G. S.; Pensack, R. D.; Payne, M. M.; Rimshaw, A.; Scholes, G. D.; Anthony, J. E.; Asbury, J. B. Dynamic Exchange During Triplet Transport in Nanocrystalline TIPS-Pentacene Films. *J. Am. Chem. Soc.* **2016**, *138* (49), 16069–16080. https://doi.org/10.1021/jacs.6b10010.

(6) Jones, A. C.; Kearns, N. M.; Ho, J.-J.; Flach, J. T.; Zanni, M. T. Impact of Non-Equilibrium Molecular Packings on Singlet Fission in Microcrystals Observed Using 2D White-Light Microscopy. *Nature Chemistry* **2020**, *12* (1), 40–47. https://doi.org/10.1038/s41557-019-0368-9.

(7) Lubert-Perquel, D.; Szumska, A. A.; Azzouzi, M.; Salvadori, E.; Ruloff, S.; Kay, C. M. W.; Nelson, J.; Heutz, S. Structure Dependence of Kinetic and Thermodynamic Parameters in Singlet Fission Processes. *J. Phys. Chem. Lett.* **2020**, *11* (22), 9557–9565. https://doi.org/10.1021/acs.jpclett.0c02505.

(8) Arias, D. H.; Ryerson, J. L.; Cook, J. D.; Damrauer, N. H.; Johnson, J. C. Polymorphism Influences Singlet Fission Rates in Tetracene Thin Films. *Chemical Science* **2016**, *7* (2), 1185–1191. https://doi.org/10.1039/c5sc03535j.

(9) Margulies, E. A.; Wu, Y.-L.; Gawel, P.; Miller, S. A.; Shoer, L. E.; Schaller, R. D.; Diederich, F.; Wasielewski, M. R. Sub-Picosecond Singlet Exciton Fission in Cyano-Substituted Diaryltetracenes. *Angewandte Chemie International Edition* **2015**, *54* (30), 8679–8683. https://doi.org/10.1002/anie.201501355.

(10) Roberts, S. T.; McAnally, R. E.; Mastron, J. N.; Webber, D. H.; Whited, M. T.; Brutchey, R. L.; Thompson, M. E.; Bradforth, S. E. Efficient Singlet Fission Discovered in a Disordered Acene Film. *J. Am. Chem. Soc.* **2012**, *134* (14), 6388–6400. https://doi.org/10.1021/ja300504t.

(11) Arias, D. H.; Ryerson, J. L.; Cook, J. D.; Damrauer, N. H.; Johnson, J. C. Polymorphism Influences Singlet Fission Rates in Tetracene Thin Films. *Chem. Sci.* **2016**, *7* (2), 1185–1191. https://doi.org/10.1039/C5SC03535J.

(12) Diao, Y.; Lenn, K. M.; Lee, W.-Y.; Blood-Forsythe, M. A.; Xu, J.; Mao, Y.; Kim, Y.; Reinspach, J. A.; Park, S.; Aspuru-Guzik, A.; Xue, G.; Clancy, P.; Bao, Z.; Mannsfeld, S. C. B. Understanding Polymorphism in Organic Semiconductor Thin Films through Nanoconfinement. *J. Am. Chem. Soc.* **2014**, *136* (49), 17046–17057. https://doi.org/10.1021/ja507179d.

(13) Anthony, J. E. Funtionalized Pentacene: Improved Electronic Properties from Improved Solid-State Order. *JACS* **2001**.

(14) Li, Y.; Wan, J.; Smilgies, D.-M.; Bouffard, N.; Sun, R.; Headrick, R. L. Nucleation and Strain-Stabilization during Organic Semiconductor Thin Film Deposition. *Nature Scientific Reports* **2016**, *6* (1), 32620. https://doi.org/10.1038/srep32620.

(15) Tayebjee, M. J. Y.; Schwarz, K. N.; MacQueen, R. W.; Dvořák, M.; Lam, A. W. C.; Ghiggino, K. P.; McCamey, D. R.; Schmidt, T. W.; Conibeer, G. J. Morphological Evolution and Singlet Fission in Aqueous Suspensions of TIPS-Pentacene Nanoparticles. *J. Phys. Chem. C* **2016**, *120* (1), 157–165. https://doi.org/10.1021/acs.jpcc.5b11353.

(16) Schaberle, F. A.; Serpa, C.; Arnaut, L. G.; Ward, A. D.; Karlsson, J. K. G.; Atahan, A.; Harriman, A. The Photophysical Properties of Triisopropylsilyl-Ethynylpentacene—A Molecule with an Unusually Large Singlet-Triplet Energy Gap—In Solution and Solid Phases. *Chemistry* **2020**, *2* (2). https://doi.org/10.3390/chemistry2020033.

(17) Niu, M.; Zheng, F.; Yang, X.; Bi, P.; Feng, L.; Hao, X. Molecular Packing Correlated Fluorescence in TIPS-Pentacene Films. *Organic Electronics* **2017**, *49*, 340–346. https://doi.org/10.1016/j.orgel.2017.07.007.

(18) Grieco, C.; Doucette, G. S.; Munro, J. M.; Kennehan, E. R.; Lee, Y.; Rimshaw, A.; Payne, M. M.; Wonderling, N.; Anthony, J. E.; Dabo, I.; Gomez, E. D.; Asbury, J. B. Triplet Transfer Mediates Triplet Pair Separation during Singlet Fission in 6,13-Bis(Triisopropylsilylethynyl)-Pentacene. *Advanced Functional Materials* **2017**, *27* (46). https://doi.org/10.1002/adfm.201703929.

(19) Pensack, R. D.; Purdum, G. E.; Mazza, S. M.; Grieco, C.; Asbury, J. B.; Anthony, J. E.; Loo, Y.-L.; Scholes, G. D. Excited-State Dynamics of 5,14-vs 6,13-Bis(Trialkylsilylethynyl)-Substituted Pentacenes: Implications for Singlet Fission. https://doi.org/10.1021/acs.jpcc.2c00897.

(20) Munson, K. T.; Gan, J.; Grieco, C.; Doucette, G. S.; Anthony, J. E.; Asbury, J. B. Ultrafast Triplet Pair Separation and Triplet Trapping Following Singlet Fission in Amorphous Pentacene Films. *Journal of Physical Chemistry C* **2020**, *124* (43), 23567–23578. https://doi.org/10.1021/acs.jpcc.0c07920.

(21) Piland, G. B.; Burdett, J. J.; Dillon, R. J.; Bardeen, C. J. Singlet Fission: From Coherences to Kinetics. *Journal of Physical Chemistry Letters*. American Chemical Society July 3, 2014, pp 2312–2319. https://doi.org/10.1021/jz500676c.

(22) Bae, Yj.; Schatz, G.; Wasielewski, M.; Christensen, J.; Kang, G.; Malliakas, C.; Zhou, J.; Nelson, J.; Young, R.; Wu, Y. Design Principles for Efficient Singlet Fission in Anthracene-Based Organic Semiconductors; SPIE-INT SOC OPTICAL ENGINEERING Location BELLINGHAM, 2019; p 24.

(23) Doucette, G. S.; Huang, H.-T.; Munro, J. M.; Munson, K. T.; Park, C.; Anthony, J. E.; Strobel, T.; Dabo, I.; Badding, J. V.; Asbury, J. B. Tuning Triplet-Pair Separation versus Relaxation Using a Diamond Anvil Cell. *Cell Reports Physical Science* **2020**, *1* (1), 100005. https://doi.org/10.1016/j.xcrp.2019.100005.

(24) Rathnayake, P. V. G. M.; Bernardi, S.; Widmer-Cooper, A. Evaluation of the AMOEBA Force Field for Simulating Metal Halide Perovskites in the Solid State and in Solution. *J. Chem. Phys.* **2020**, *152* (2), 024117. https://doi.org/10.1063/1.5131790.

(25) Xu, T.; Wang, W.; Yin, S. Electrostatic Polarization Energies of Charge Carriers in Organic Molecular Crystals: A Comparative Study with Explicit State-Specific Atomic Polarizability Based AMOEBA Force Field and Implicit Solvent Method. *J. Chem. Theory Comput.* **2018**, *14* (7), 3728–3739. https://doi.org/10.1021/acs.jctc.8b00132.

(26) Zhang, C.; Bell, D.; Harger, M.; Ren, P. Polarizable Multipole-Based Force Field for Aromatic Molecules and Nucleobases. *J. Chem. Theory Comput.* **2017**, *13* (2), 666–678. https://doi.org/10.1021/acs.jctc.6b00918.

(27) Eastman, P.; Swails, J.; Chodera, J. D.; McGibbon, R. T.; Zhao, Y.; Beauchamp, K. A.; Wang, L.-P.; Simmonett, A. C.; Harrigan, M. P.; Stern, C. D.; Wiewiora, R. P.; Brooks, B. R.; Pande, V. S. OpenMM 7: Rapid Development of High Performance Algorithms for Molecular Dynamics. *PLOS Computational Biology* **2017**, *13* (7), e1005659. https://doi.org/10.1371/journal.pcbi.1005659.

Chapter 4: Detection of ionizing radiation using scintillator materials

4.1 Introduction to Radiation Detection

4.1.1 Types of electromagnetic radiation

Electromagnetic radiation can be found all around us. We visually see objects using our eyes, which act as detectors for visible light. However, there are other types of light that we cannot see with our eyes, such as radio waves, microwaves, infrared, ultraviolet, X-rays, and gamma rays. Electromagnetic radiation of varying types differs in the energy of the photon, as shown in **Fig. 4.1**,[1] and each of them interact with matter differently. Lower energy radiation, such as microwaves and infrared, are absorbed by molecules and cause them to vibrate and/or stretch, essentially converting the absorbed energy to heat. At a slightly higher energy, the absorption of visible light absorption can result in excited molecules whereby an electron is promoted to higher molecular energy levels. The excited electron can then relax back down to the unexcited ground state by re-

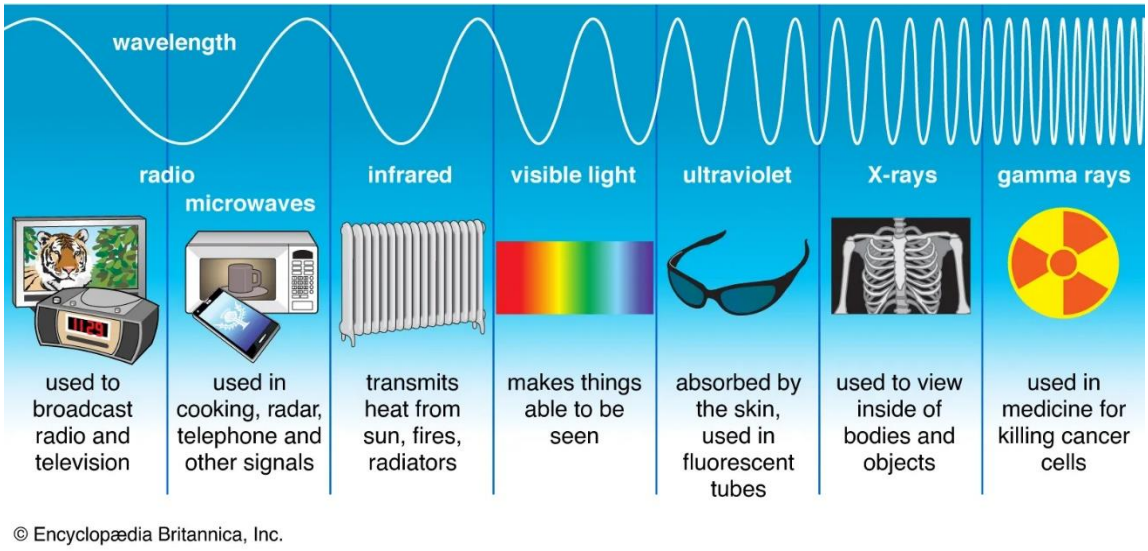

Figure 4.1. Types of Electromagnetic Radiation. Copyright of Encyclopedia Britannica, Inc. [ref. 1]

emitting a photon or relax via nonradiative relaxation, such as giving off heat. These relatively lower energy electromagnetic radiation types are categorized as non-ionizing sources of radiation. Higher energy radiation, such as ultraviolet, X-rays, and gamma rays, deposits enough energy in atoms and molecules to remove the excited electron from the material completely, making these types ionizing radiation.

4.1.2 Discovery of X-rays in 1895

X-rays were discovered by William Rontgen in 1895 while conducting an experiment with a vacuum tube.[2,3] For an unknown reason, a piece of cardboard plated with barium platinocyanide began to glow. Unbeknownst to Rontgen, he was producing X-ray radiation that was being absorbed by the cardboard sheet and causing it to emit visible light. The newly discovered radiation was termed "X-ray" due to it being unknown radiation.[4] Next, studied the properties of the X-rays and noted that the radiation was transmitted through some materials but not metals and very thick materials. Stemming from this observation, he then used the X-rays to create a new form of photography that can be used to see inside objects, including the human body.[4,5] Rontgen produced the first X-ray image, as shown in **Fig. 4.2** on the **left**.[5] Since then, X-ray imaging techniques have been developed to improve spatial resolution. A modern-day image of a hand is shown in **Fig. 4.2** on the **right**.[6]

Figure 4.2. The first X-ray image taken in 1895 (*left*) and modern day X-ray image (*right*).

4.1.3 Penetrating power of ionizing radiation

Ionizing radiation, such as X-rays and gamma-rays, have more penetrating power than non-ionizing radiation, which means that these high energy photons penetrate deeper into a given medium.[7] The probability that a high energy photon is absorbed by a medium depends on material thickness and its material-dependent absorption coefficient. The fraction of transmitted photons is shown in Equation 4.1. **I** is the transmitted intensity, $\mathbf{I_0}$ is the incident intensity, **μ** is the linear attenuation coefficient, and **d** is the thickness of the material.[7]

$$\frac{I}{I_0} = e^{-\mu d} \qquad \text{Eq. 4.1}$$

Higher atomic number (Z) elements, such as calcium or lead, attenuate X-rays more than lighter Z elements, such as carbon. **Fig. 4.3a-b** shows a depiction of the difference in X-ray transmission through lead and water. Lead is a high Z element with a high attenuation coefficient compared to water, which is composed of lighter Z elements. Given the same thickness of lead and water, more X-rays of a specific energy will be transmitted through water than through lead. **Fig. 4.3c** shows the effect of material thickness on the percent of 50 keV X-ray transmission.[8] As the material thickness increases, the percent of X-rays transmitted decreases and materials with higher Z elements require less material to achieve total attenuation. The varying transmission of X-rays based on atomic number Z and thickness allow for modern X-ray imaging of bones, teeth, and objects.

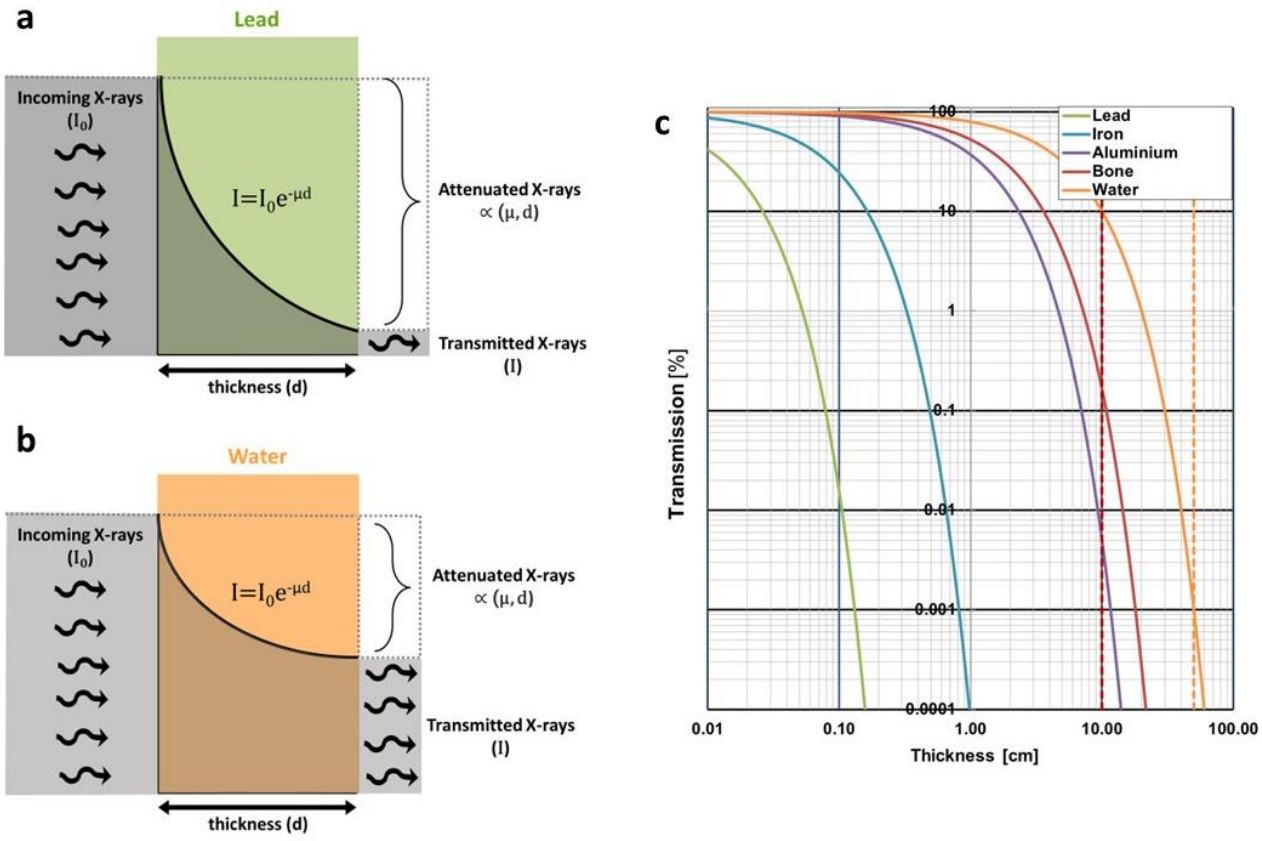

Figure 4.3. Depiction of the interaction of materials with X-rays. The attenuation of X-rays with **a)** lead and **b)** water. **c)** The effect of material and material thickness on transmission of 50 keV X-rays. Dashed lines refer to thickness of 10 cm and 50 cm for bone and water, respectively [ref. 3].

4.1.4 Scintillators for ionizing radiation detection

Ionizing radiation aggressively strips away electrons which produces ions, and thus it can be damaging to cells in living organisms as well as destructive to materials.[7] Because X-rays are not detectable by eye, secondary materials are needed to detect X-rays. Scintillators are materials that absorb X-rays or gamma-rays and down convert the absorbed energy into visible or NIR photons. The detection of ionizing radiation is shown in **Fig. 4.4**. When a high energy photon is

absorbed at the interaction site, a primary electron with a large excess of kinetic energy is created. The primary electron dissipates its energy to surrounding electrons and a cascade of secondary excited electrons is produced. As electrons become lower in energy, they begin to radiatively relax and emit lower energy photons. Finally, a second detector is used to collect the lower energy photons. Scintillators can be coupled to various secondary detectors, such as photomultiplier tubes, avalanche photodiodes, or charged coupled devices, which is contingent on the desired application.[2,7]

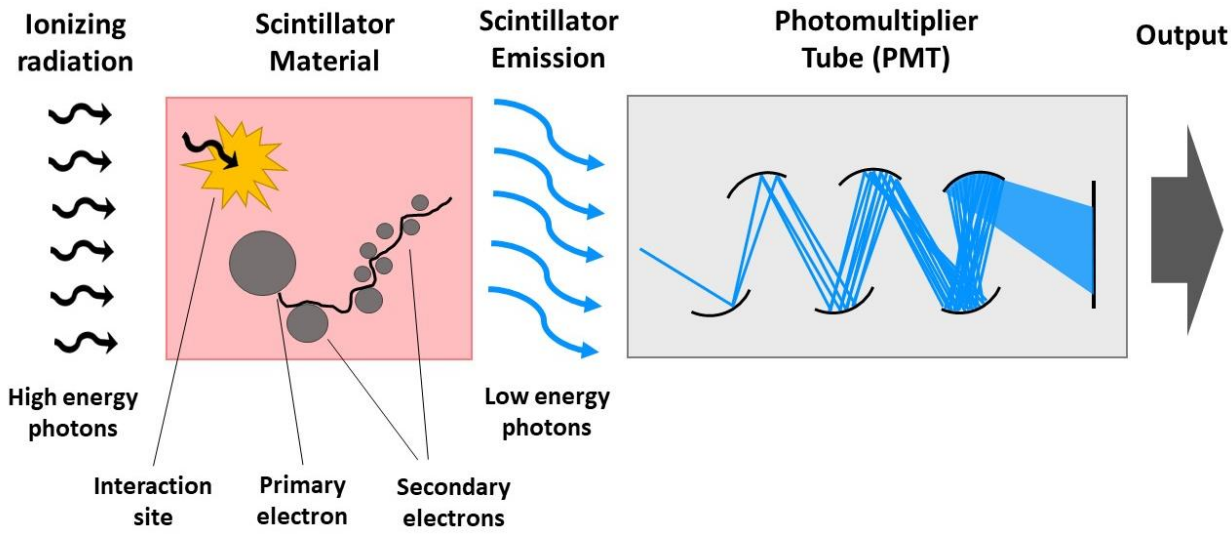

Figure 4.4. Schematic of ionizing radiation interacting with a scintillating material to convert high energy photons to low energy photons which are detected using a photomultiplier tube.

Modern scintillator detectors have been employed in applications such as medical imaging, security, and high energy physics.[2,9–11] Light yield is a key performance metric for scintillators and is defined as the number of scintillated photons per mega-electron volt (MeV) of energy deposited in the material.[7,12] High-performing commercial scintillators are typically grown as single crystals,

making them very expensive.[2] A benchmark scintillator is cesium iodide doped with thallium, which has a high light yield of 60,000 photons per MeV.[13] Other commercial scintillators, such as plastic scintillators, are cheaper but tend to have lower light yields and long decay times. Because higher-performing scintillators are grown as single crystals, they are unable to be used in applications that require large-area detectors.

4.2 Lead Halide Perovskites as Scintillators

Lead halide perovskites have desirable properties that are required for efficient ionizing radiation detection and scalability that can overcome limitations of current technology. The crystal structures of three-dimensional (3D) and two-dimensional (2D) perovskites are shown in **Fig. 4.5a** and **b**, respectively. 3D perovskites are composed of octahedra extending in all dimensions while 2D perovskites are comprised of octahedral sheets that are broken up by bulky organic cations. Both 2D and 3D perovskite structures are composed of heavy atoms, such as lead, chloride, bromide, and iodine, resulting in a high effective mass, Z_{eff}, that allows for strong interactions with high energy photons. As a result, perovskites have excellent stopping power, which defined as a material's ability to attenuate high energy radiation; photons with energies up to 1 MeV have a

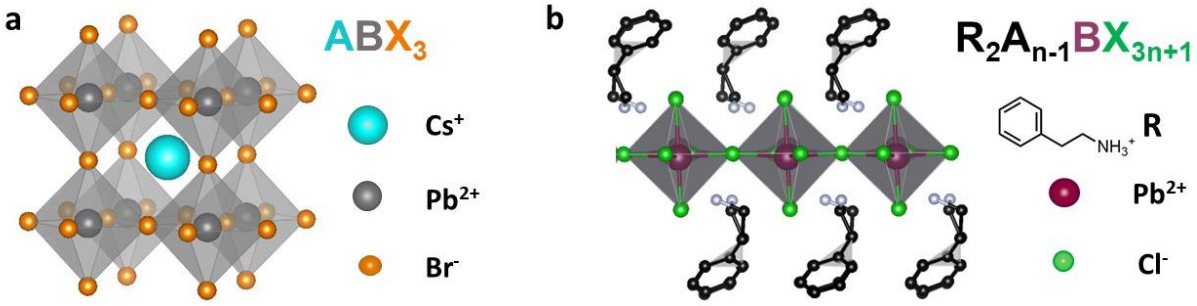

Figure 4.3. Crystal structure of **a)** three-dimensional and **b)** two-dimensional perovskites. For the 2D perovskite example, a one-layer (i.e. n=1) perovskite structure is shown.

penetration depth of only ~1 centimeter in perovskite materials.[14] The defect tolerance of lead halide perovskites allow for charge carrier diffusion lengths of ~1 um and long carrier mobility lifetimes, which is beneficial for optoelectronic-based devices as well as for scintillator applications.[15–19] Wei, et al. implemented single crystal $MAPbBr_3$ for X-ray detection via photon-to-current conversion and reported a record high mobility-lifetime product of $1.2x10^{-2}$ cm^2V^{-1}.[19] Lead halide perovskites have tunable emission properties based on material composition (e.g. Cl, Br, I), and in the case of 2D perovskites, the degree of quantum confinement. Perovskites are composed of cheap, abundant materials that are solution processible at low temperatures and consequentially, they can be fabricated as thin films, single crystals, or powders. Also, as a result of their solution processability, lead halide perovskites are candidates for large-area detector applications via large-area thin film manufacturing[20] or through the sintering of perovskite powders into pellets of varying size and geometry.[21] Lead halide perovskites are a compelling class of materials for cost-effective and potentially efficient alternatives to current radiation detection technology.

4.3 References

(1) Britannica, T. E. of E. Electromagnetic Spectrum. **2022**. https://www.britannica.com/science/electromagnetic-spectrum.

(2) Nikl, M. Scintillation Detectors for X-Rays. *Measurement Science and Technology* **2006**, *17* (4), R37–R54. https://doi.org/10.1088/0957-0233/17/4/r01.

(3) Assmus, A. Early History of X Rays. *Beam Line* **1995**, No. Summer 1995, 10–24.

(4) Röntgen, W. C. On a New Kind of Rays. *Science* **1896**, *3* (59), 227–231. https://doi.org/10.1126/science.3.59.227.

(5) W C Rontgen. Ueber Eine Neue Art von Strahlen. *Sitz. Ber. Phys. Med. Ges. Wuerzb* **1895**, *9*, 132–141.

(6) Anil K Bhat; et al. Radiographic Imaging of the Wrist. *Indian journal of plastic surgery : official publication of the Association of Plastic Surgeons of India* **2011**, *44* (2), 186–196. https://doi.org/doi:10.4103/0970-0358.85339.

(7) Knoll, G. F. *Radiation Detection and Measurement*, Third.; John Wiley and Sons, Inc., 2009.

(8) Paulis, L.; Kroll, J.; Heijnens, L.; Huijnen, M.; Gerretsen, R.; Backes, W.; Hofman, P. Is CT Bulletproof? On the Use of CT for Characterization of Bullets in Forensic Radiology. *International journal of legal medicine* **2019**, *133*, 1869–1877. https://doi.org/10.1007/s00414-019-02033-0.

(9) Birowosuto, M. D.; Dorenbos, P. Novel γ- and X-Ray Scintillator Research: On the Emission Wavelength, Light Yield and Time Response of Ce3+ Doped Halide Scintillators. *physica status solidi (a)* **2009**, *206* (1), 9–20. https://doi.org/10.1002/pssa.200723669.

(10) Carel W E van Eijk. Inorganic Scintillators in Medical Imaging. *Physics in Medicine & Biology* **2002**, *47* (8), R85. https://doi.org/10.1088/0031-9155/47/8/201.

(11) YANAGIDA, T. Inorganic Scintillating Materials and Scintillation Detectors. *Proceedings of the Japan Academy, Series B* **2018**, *94* (2), 75–97. https://doi.org/10.2183/pjab.94.007.

(12) de Haas, J. T. M.; Dorenbos, P.; van Eijk, C. W. E. Measuring the Absolute Light Yield of Scintillators. *Nuclear Instruments and Methods in Physics Research Section A: Accelerators, Spectrometers, Detectors and Associated Equipment* **2005**, *537* (1), 97–100. https://doi.org/10.1016/j.nima.2004.07.243.

(13) Epic Crystal. CsI(Tl) Scintillator. https://www.epic-crystal.com/halide-scintillators/csi-tl-scintillator.html.

(14) Birowosuto, M. D.; Cortecchia, D.; Drozdowski, W.; Brylew, K.; Lachmanski, W.; Bruno, A.; Soci, C. X-Ray Scintillation in Lead Halide Perovskite Crystals. *Scientific Reports* **2016**, *6* (1), 37254. https://doi.org/10.1038/srep37254.

(15) Stranks Samuel D.; Eperon Giles E.; Grancini Giulia; Menelaou Christopher; Alcocer Marcelo J. P.; Leijtens Tomas; Herz Laura M.; Petrozza Annamaria; Snaith Henry J. Electron-Hole Diffusion Lengths Exceeding 1 Micrometer in an Organometal Trihalide Perovskite Absorber. *Science* **2013**, *342* (6156), 341–344. https://doi.org/10.1126/science.1243982.

(16) Lee, M. M.; Teuscher, J.; Miyasaka, T.; Murakami, T. N.; Snaith, H. J. Efficient Hybrid Solar Cells Based on Meso-Superstructured Organometal Halide Perovskites. *Science* **2012**, *338* (6107), 643. https://doi.org/10.1126/science.1228604.

(17) Burschka, J.; Pellet, N.; Moon, S.-J.; Humphry-Baker, R.; Gao, P.; Nazeeruddin, M. K.; Grätzel, M. Sequential Deposition as a Route to High-Performance Perovskite-Sensitized Solar Cells. *Nature* **2013**, *499* (7458), 316–319. https://doi.org/10.1038/nature12340.

(18) Zhou Huanping; Chen Qi; Li Gang; Luo Song; Song Tze-bing; Duan Hsin-Sheng; Hong Ziruo; You Jingbi; Liu Yongsheng; Yang Yang. Interface Engineering of Highly Efficient Perovskite Solar Cells. *Science* **2014**, *345* (6196), 542–546. https://doi.org/10.1126/science.1254050.

(19) Wei, H.; Fang, Y.; Mulligan, P.; Chuirazzi, W.; Fang, H.-H.; Wang, C.; Ecker, B. R.; Gao, Y.; Loi, M. A.; Cao, L.; Huang, J. Sensitive X-Ray Detectors Made of Methylammonium Lead Tribromide Perovskite Single Crystals. *Nature Photonics* **2016**, *10* (5), 333–339. https://doi.org/10.1038/nphoton.2016.41.

(20) Zhang, Y.; Sun, R.; Ou, X.; Fu, K.; Chen, Q.; Ding, Y.; Xu, L.-J.; Liu, L.; Han, Y.; Malko, A. V.; Liu, X.; Yang, H.; Bakr, O. M.; Liu, H.; Mohammed, O. F. Metal Halide Perovskite Nanosheet for X-Ray High-Resolution Scintillation Imaging Screens. *ACS Nano* **2019**, *13* (2), 2520–2525. https://doi.org/10.1021/acsnano.8b09484.

(21) Dagnall, K. A.; Conley, A. M.; Yoon, L. U.; Rajeev, H. S.; Lee, S.-H.; Choi, J. J. Ytterbium-Doped Cesium Lead Chloride Perovskite as an X-Ray Scintillator with High Light Yield. *ACS Omega* **2022**, *7* (24), 20968–20974. https://doi.org/10.1021/acsomega.2c01712.

Chapter 5: Development of relative scintillation light yield methodology suitable for X-ray excitation sources with continuum of energies

5.1 Abstract

Light yield is a key performance parameter for evaluating the efficiency of scintillators. Light yield is defined as the number of scintillated photons emitted per mega-electron volt of energy absorbed by the scintillator material. Pulse height spectrometry is a commonly used method for measuring light yield whereby a gamma-ray emitter is used for monochromatic excitation, such as ^{137}Cs, of the scintillator being tested, and scintillated photon intensity is compared against a calibrated, known intensity. The radioactivity of gamma-ray ray sources, photon emission decreases over time according to its half-life, resulting in decreasing excitation photon flux over time. To increase gamma-ray photon flux, higher activity sources can be used, but special health and safety regulations are required, such as monitoring of total dose to the experimenter or special enclosures and handling of the radioactive source. While low activity sources are able to be handled more freely, the lower gamma-ray activity results in lower excitation photon flux and thus, lower scintillated photon signals that were not able to be observed. We opted to use a continuous spectrum X-ray source whereby X-rays up to 40 keV are produced via Bremsstrahlung radiation to increase photon flux and provide consistent excitation source to study novel perovskite scintillators. Because this is a continuous source that delivers a spectrum of photon energies to scintillator samples, a new methodology for quantifying the light yield needed to be developed. Here, we describe our methodology for measuring light yield using a continuous X-ray source.

5.2 Introduction

5.2.1 Light yield definition

Light yield is defined as the number of scintillated photons from a scintillator divided by the amount of energy absorbed by the material, as shown in Equation 5.1 below.

$$Light\ yield = \frac{Number\ of\ scintillated\ photons\ (counts)}{Amount\ of\ energy\ absorbed\ by\ the\ material\ (MeV)} \quad \text{Eq. 5.1}$$

A commonly reported method for measuring the light yield of scintillators is using pulse height spectrometry, wherein a radioactive source is used to calibrate the instrument response prior to the analysis of energy features (i.e. Compton edge, photopeak). However, because we used an X-ray tube source, which provides a continuous spectrum of X-ray energies, we adopted a different method.

5.2.2 Light yield methodology overview

The light yields of doped perovskite scintillators were determined in two parts. First, the scintillated photon output of commercial and sample scintillators was quantified by correlating a known number of incoming photons to the photon multiplier tube (PMT) detector response. A Xenon arc lamp was used as reference light to quantify the number of incoming photons using silicon and germanium power meters in the visible and near infrared (NIR) regions, respectively. Reference light wavelengths were filtered using bandpass filters purchased from Thor Labs and were selected to match the peak maximum of scintillator emission. Reference light was scattered inside of an integrating sphere using an identical geometry to that of the commercial and doped

perovskite scintillators, and detector responses were measured. The scintillated photon output of scintillators was calculated using a ratio of the known photon/detector responses from reference light measurements and sample scintillated emission measured by the detector, similar to the relative fluorescence method used to calculated quantum yields. Second, the energy deposited into the scintillators was quantified using the reported light yields of two commercial scintillators, calcium fluoride doped with europium (CaF_2(Eu)) and cesium iodide doped with thallium (CsI(TI)), and the measured scintillated photon outputs. Incoming X-rays were completely attenuated by the commercial scintillators, and thus energy deposited in both materials are equivalent. Reported light yields are measured using radioactive ^{137}Cs which emits photons with a monochromatic energy of 662 keV. Because the X-ray source used in this study produces photons with significantly lower energy that range up to only 40 keV, energy deposited values were corrected for non-proportionality. Sufficient doped perovskite scintillator powder was used (six to twelve Kapton capillaries) such that all X-rays were attenuated, and thus, the energy deposited is the same as that calculated for commercial scintillators. With scintillated light output quantified using reference light and power meters, the light yield was then calculated using this energy deposited value.

5.3 Light yield methodology

5.3.1 Materials

X-rays were generated using a Moxtek 60 kV 12-Watt MagPro X-ray imaging source with the operating voltage set to 40 kilovolts (kV) and the current set to 300 microamps (μA). CaF_2(Eu), CsI(TI), and cesium iodide doped with sodium (CsI(Na)) commercial scintillators were purchased from Epic Crystal Co. as 25.4 x 25.4 x 25.4 mm^3 cubes with all sides polished. The documented

light yields are 19,000, 60,000 and 41,000 $phMeV^{-1}$, respectively. Plastic scintillators were purchased from Epic Crystal. An acrylic glass cube was purchased from U.S. Plastic Corporation with dimensions 25.4 x25.4x25.4 mm^3 with all sides polished. Silicon (PM16-120) and germanium (PM16-122) photodiode power meters were purchased from Thor Labs. Bandpass filters were purchased from Thor Labs (480 ± 10 nm, 1000 ± 10 nm, 1150 ± 10 nm, 1250 ± 10 nm).

5.3.2 Powder sample preparation

Powder samples were packed into 12 Kapton capillaries purchased from Cole-Parmer (0.0710" ID, 0.0750" OD, cut to a length of 50 mm). Capillaries were sealed on both ends with Sigillum Wax Sealant purchased from Thomas Scientific and arranged into two rows of six, which was required to achieve total attenuation of X-rays.

5.3.3 Quantifying photon output of scintillators

The photon output of the halogen lamp light source was used in conjunction with a power meter and PMT detector to determine the photon output of the commercial and doped perovskite scintillators. Wavelengths matching that of the commercial and doped perovskite scintillators were selected for the reference light power meter measurements, as detailed in **Table 5.1**.

Scintillator	Emission of scintillator photons λ_{em}	Reference light wavelength λ_{em}
$CaF_2(Eu)$	435 nm	440 nm
CsI(TI)	550 nm	560 nm
Yb-doped $CsPbCl_3$	1000 nm	1000 nm
QD-doped $MAPbBr_3$ (3.8 nm QDs)	~1130 – 1200 nm	1150 nm
QD-doped $MAPbBr_3$ (4.3 nm QDs)	~1230 – 1300 nm	1250 nm

Table 5.1 The emission peak of commercial, Yb-doped $CsPbCl_3$, and QD-doped $MAPbBr_3$ scintillators and their reference light pairings. Reference light was scattered using a medium similar to the corresponding commercial and sample scintillator.

PMT detectors are known to have a region whereby the photon counts read by the detector is proportional to the number of photons. When incident photon flux hitting the detector becomes very high, then this proportionality breaks down and the number of photons is no longer related to the counts read by the detector. This breakdown in proportionality can be seen in **Fig. 5.1**. The linear region of the NIR and Vis PMT detectors were determined prior to light yields measurements, and all measurements were conducted in the linear regions of the detectors.

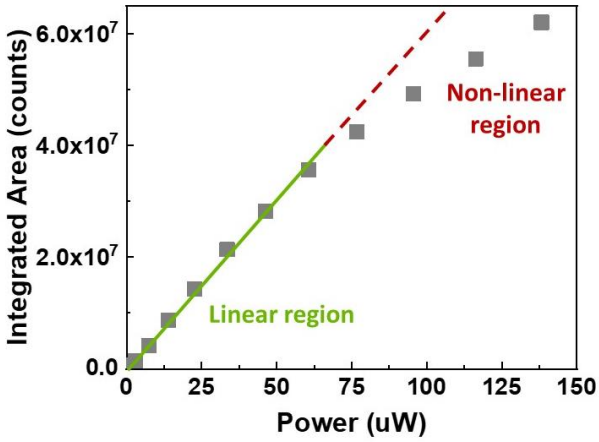

Figure 5.1. In the linear region of the detector, the integrated counts of reference light and scintillated light measured by the PMT and NIR detectors is proportional to the number of photons. As intensity increases, this one-to-one relationship breaks down in the non-linear region. All measurements relating to light yield were performed while working in the linear region of the PMT and NIR detectors.

The power of the reference light from the lamp was measured at the inlet of the integrating sphere for different excitation slit widths using a power meter. Power readings were converted to number of photons using Eq 2. The reference light was scattered in the same pattern as the scintillators to be tested; for commercial scintillators, the reference light was scattered using a polished glass cube with the same dimensions as the commercial scintillators and with the same geometry (**Fig. 5.2**).

For the doped-perovskite scintillators, reference light was scattered using non-doped perovskite powder in the same capillary configuration and geometry as doped-perovskite scintillators.

$$Power = nE_{ph} \qquad \text{Eq. 5.2}$$

Next, the scattered light signal was measured using the PMT detector. The number of photons measured with the power meter and the integrated counts from the PMT detector provide a quantitative relationship between the number of photons and counts.

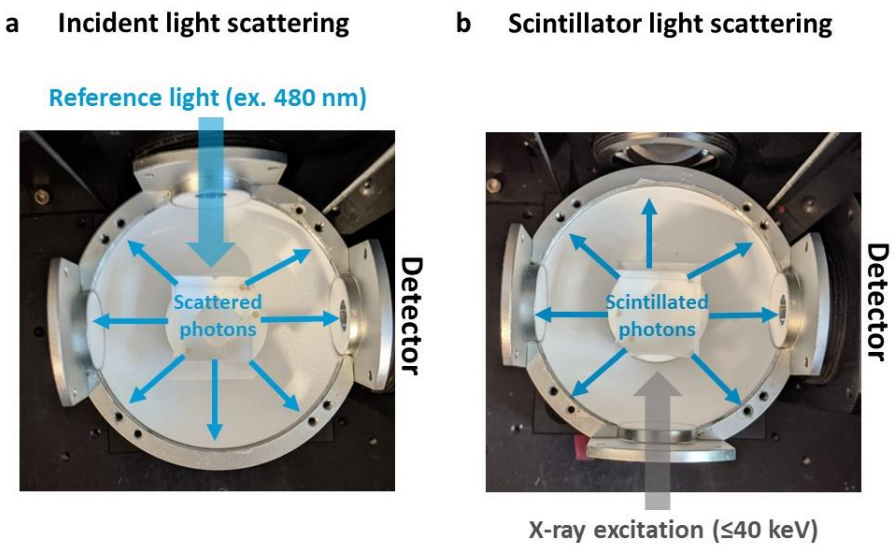

Figure 5.2. The scattering pattern of the incident light from halogen lamp (left) and the scattering pattern of scintillated photons from CaF_2(Eu) scintillator.

Lastly, the radioluminescence signals for each scintillator was measured using the PMT detector. Using Equation 5.3, the number of scintillated photons was calculated.

$$\frac{Int.\ Area\ (counts)_{comm.\ scint}}{Int.\ Area\ (counts)_{incid.\ lamp\ light}} = \frac{Number\ of\ photons_{comm.\ scint}}{Number\ of\ photons_{incid.\ lamp\ light}} \qquad \text{Eq. 5.3}$$

5.3.4 Using commercial scintillators with known light yields to determine energy deposited

Our light yield method relies on the complete X-ray attenuation of commercial and sample scintillators to ensure that the energy deposited in each material is equivalent. To show this, we first placed a detector scintillator (e.g. CsI(Na)) inside the integration sphere and took measurement of the scintillated emission (**Fig. 5.3a**). Next, the scintillator being tested for total attenuation was placed outside of the integrating sphere (e.g. CsI(TI)) in the path of the X-ray beam with the detector scintillator still inside of the integrating sphere to detect any X-ray transmission (**Fig 5.3b**). If a signal was detected from the scintillator inside the integrating sphere, then X-ray transmission through the outside scintillator was occurring and X-rays were not completely attenuated. If no signal was detected from the scintillator inside the sphere, then the scintillator outside of the sphere was indeed attenuating all of the X-rays. The cubic CaF_2(Eu) and CsI(TI) scintillators completely attenuated the X-ray beam as did two rows of six capillaries containing Yb-doped $CsPbCl_3$ powder and one row of six capillaries containing QD-doped $MAPbBr_3$ (**Fig. 5.4**).

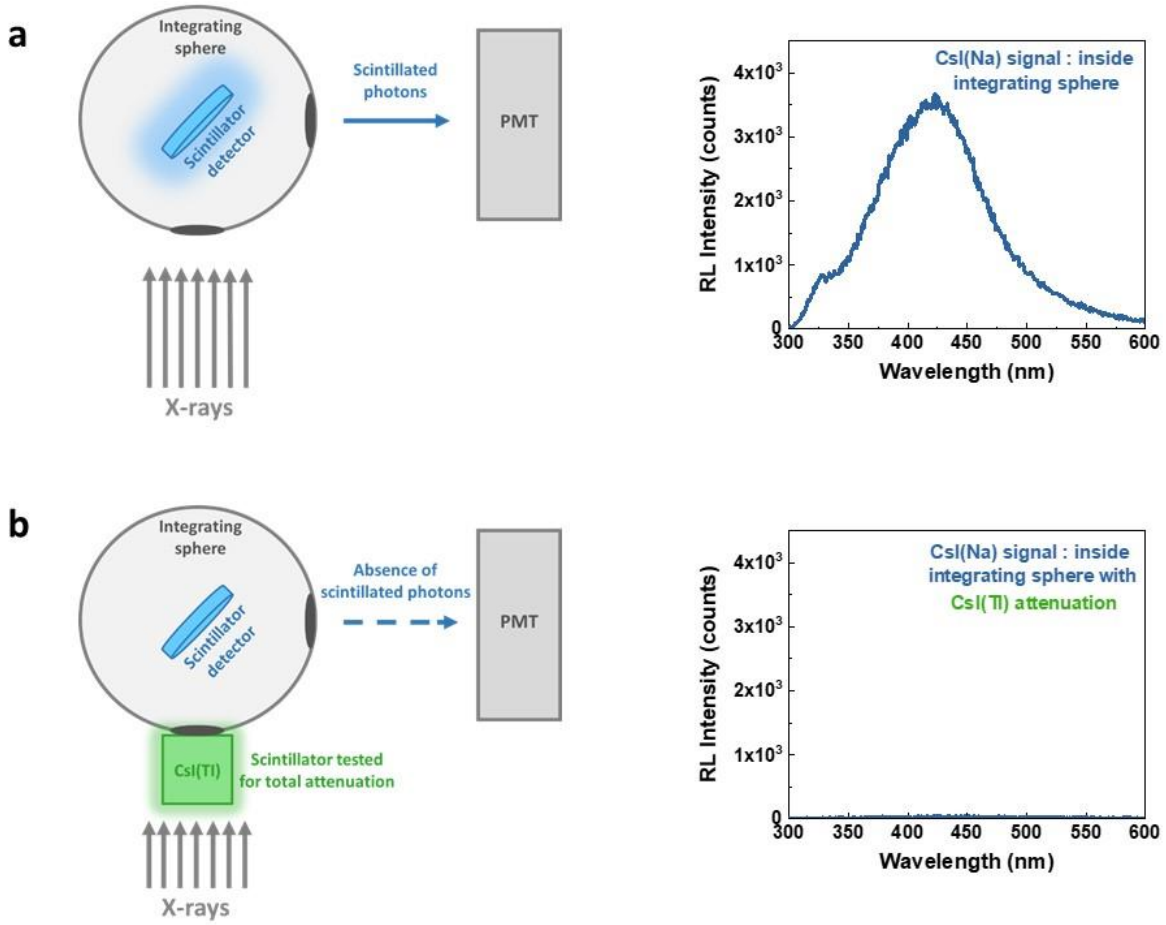

Figure 5.3. Testing for total attenuation of incoming X-rays. **a)** A scintillator is placed inside the integrating sphere and its scintillation emission signal is read by the detector. **b)** A second scintillator is tested for total attenuation by placing it between incoming X-rays and the scintillator inside the integrating sphere. No signal from the scintillator inside the integrating sphere is observed when there is no transmission through the scintillator outside the integrating sphere.

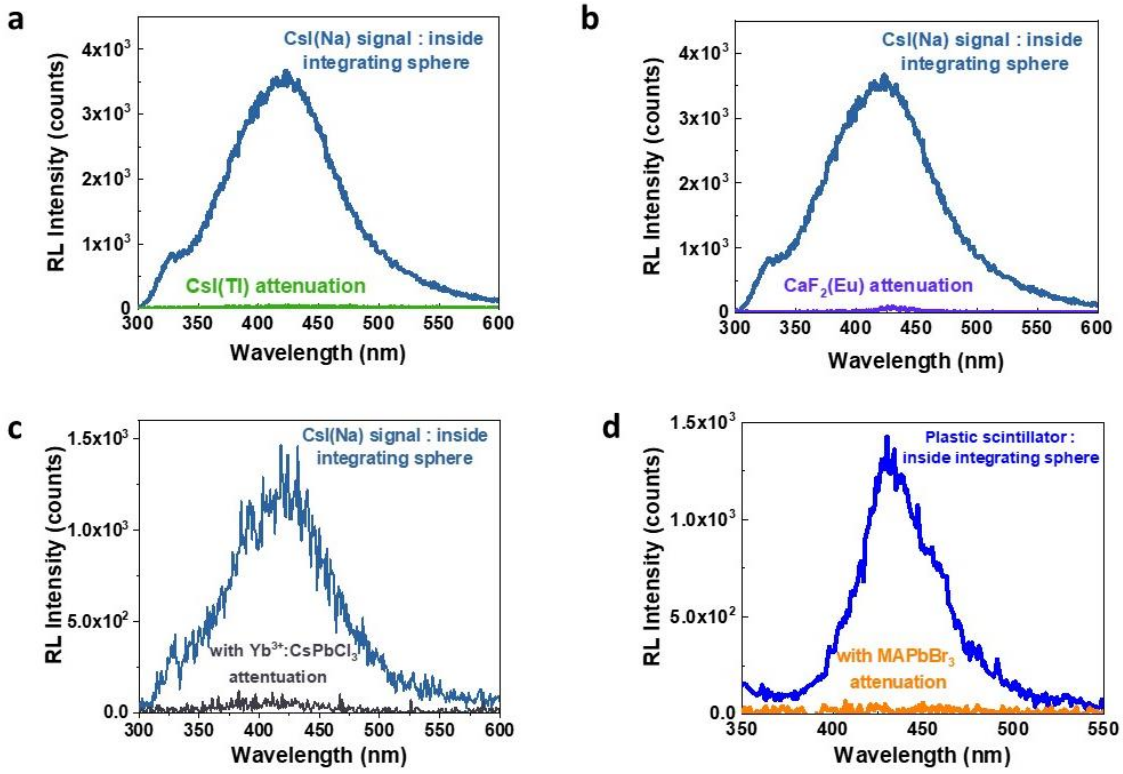

Figure 5.4. Total X-ray attenuation was shown for **a)** CsI(TI) and **b)** CaF_2(Eu) using CsI(Na) as an X-ray detector inside an integrating sphere. Total X-ray attenuation was also shown using **c)** two rows of Yb-doped $CsPbCl_3$ using CsI(Na) as the X-ray detector. **d)** one row of six capillaries filled with QD-doped $MAPbBr_3$ powder outside of the integrating sphere and a plastic scintillator as the X-ray detector.

Given that all X-rays are attenuated, the total energy deposited is equivalent for both commercial scintillators and doped-perovskite scintillators. Further, the energy deposited value should be independent of experimental parameters (i.e. slit widths). To ensure that arbitrary experimental parameters chosen by the experimenter did not significantly affect energy deposited values, four reference light points with varying intensities were used and cross-examined with emission curves collecting with varying emission slit width. To confirm this, the excitation slit width (0.75, 1, 1.25, 1.5 mm) and the emission slit width (10, 12, 13.5, 15 mm) were altered for a total of 16 unique slit width conditions for both CaF_2(Eu) and CsI(TI). The power readings for 435

nm and 480 nm reference lights, which was coupled to the maximum emission wavelength of CaF_2(Eu) and CsI(TI), respectively, with varying excitation slit widths is shown in **Fig. 5.5**. While not essential for the measurement, excitation slit width was observed to be proportional to power. The radioluminescence intensities and integrated intensities of CaF_2(Eu) and CsI(TI) commercial scintillators are shown in **Fig. 5.6**.

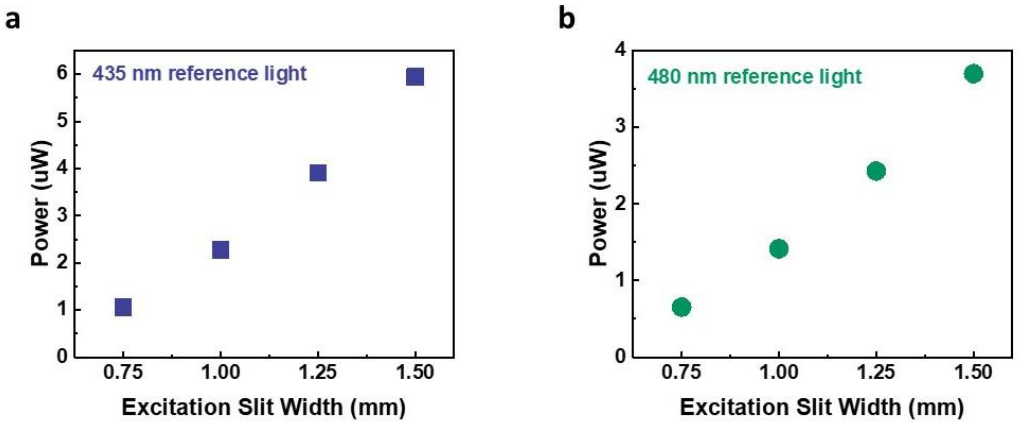

Figure 5.5. Power readings versus excitation slit width for **a)** 435 nm and **b)** 480 nm reference lights. Power is directly proportional to the number of photons of a specific wavelength. The number of incoming photons of the reference light used for light yield and energy deposited calculations was varied by varying the excitation slit width on the spectrofluorometer.

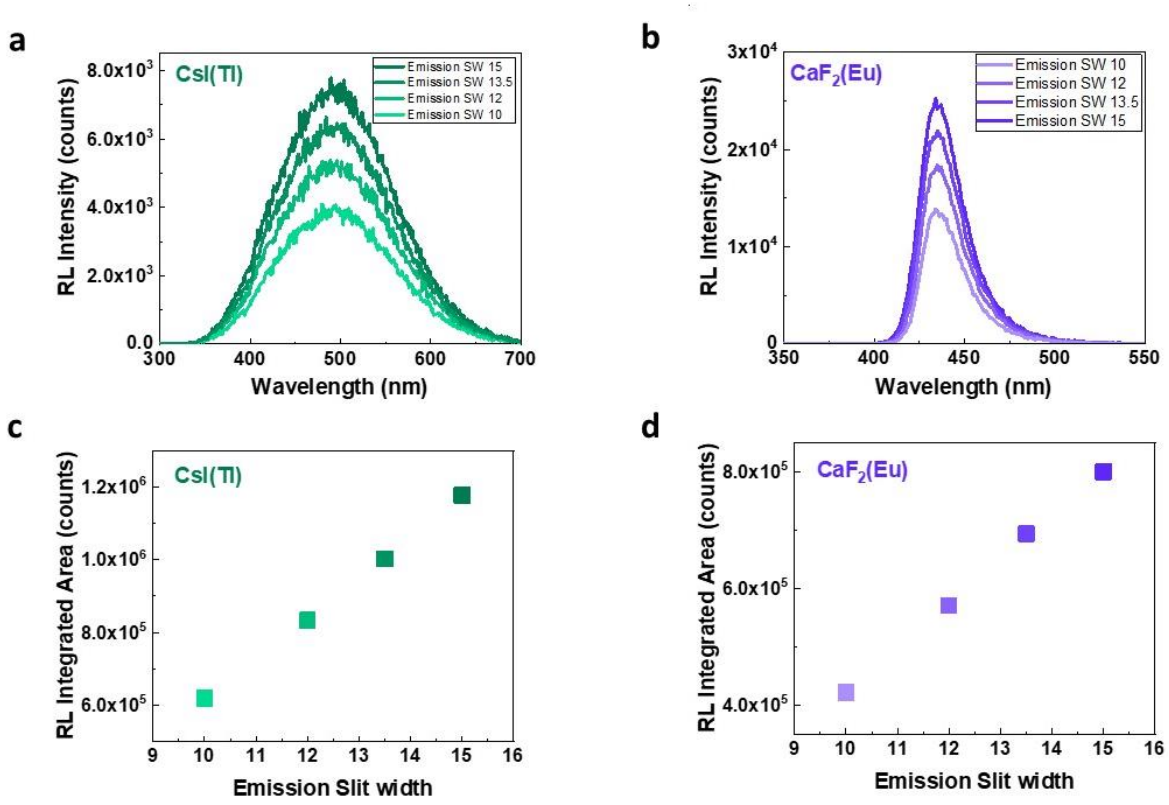

Figure 5.6. Radioluminescence curves and intensity changes of **a)** CsI(TI) and **b)** CaF_2(Eu) using different emission slit widths. Integrated areas of the radioluminescence curves for **c)** CsI(TI) and **d)** CaF_2(Eu) shows a linear relationship between slit width and detector response.

5.3.5 Non-proportionality correction

Standard reported light yields are those measured using 662 keV photon energies emitted from radioactive ^{137}Cs. For most materials, light yield values are wavelength-dependent (i.e. change with excitation energy). When varying the wavelength, the light yield of scintillators typically deviates from the light yield value measured using 662 keV photons; this phenomenon is called non-proportionality. Because the X-ray source used in this study emits lower energy

photons up to only 40 keV, energy deposited values were corrected for non-proportionality. The uncorrected calculated energy deposited values are shown in **Fig. 5.7**. on the left. Energy deposited values calculated from CaF_2(Eu) and CsI(TI) were corrected using their respective documented non-proportionalities relative to the light yield recorded using 662 keV gamma-ray photons from a ^{137}Cs source. CaF_2(Eu) suffers a 20% reduction in light yield at photon energies ranging between 10 and 40 keV while CsI(TI) exhibits a 15% increase in light yield. [1,2] The energy deposited values for both commercial scintillators are in good agreement regardless of excitation and emission slit widths. After the non-proportionality corrections, the energy deposited values using two different commercial scintillators with different light yields are in good agreement, bolstering confidence in the calculated energy deposited value used in this study for light yield calculations.

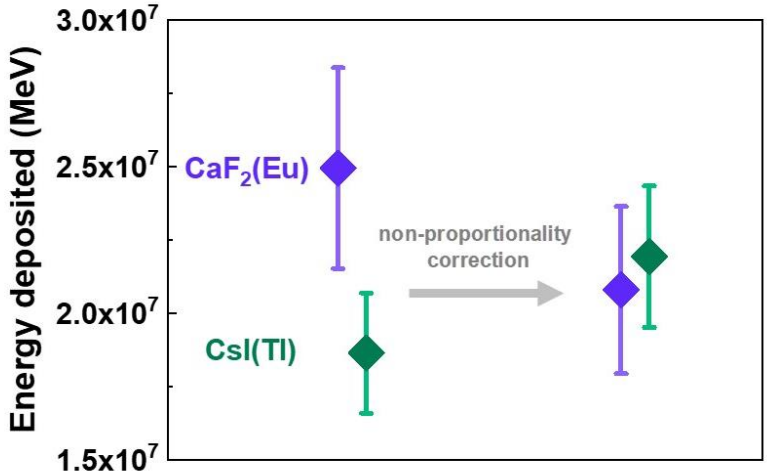

Figure 5.7. The calculated energy deposited values using commercial scintillators, CaF_2(Eu) and CsI(Eu), before and after a non-proportionality correction. The X-ray beam was completely attenuated by both scintillators.

5.3.6 Light yield of Yb^{3+}:$CsPbCl_3$

The light yield of Yb-doped $CsPbCl_3$ was calculated using an energy deposited value of $2.4x10^7$ MeV, a conservative value obtained from the above experiments. We used a range of excitation slit widths for the reference light and emission slit widths to show that the light yield measurement of at least 100,000 ph/MeV was independent of experimental conditions, adding confidence to the accuracy of our method (**Fig. 5.8**). Resolution of the radioluminescence emission spectra of Yb-doped $CsPbCl_3$ was not affected by increasing emission slit width over the chosen slit width range. For large emission slit widths (7, 10 mm), signals from larger excitation slit (2, 2.5 mm) widths approached saturation of the detector and were outside of the linear range of the detector, and thus were omitted. From this, we conclude that the light yield of Yb-doped $CsPbCl_3$ surpasses 100,000 ph/MeV.

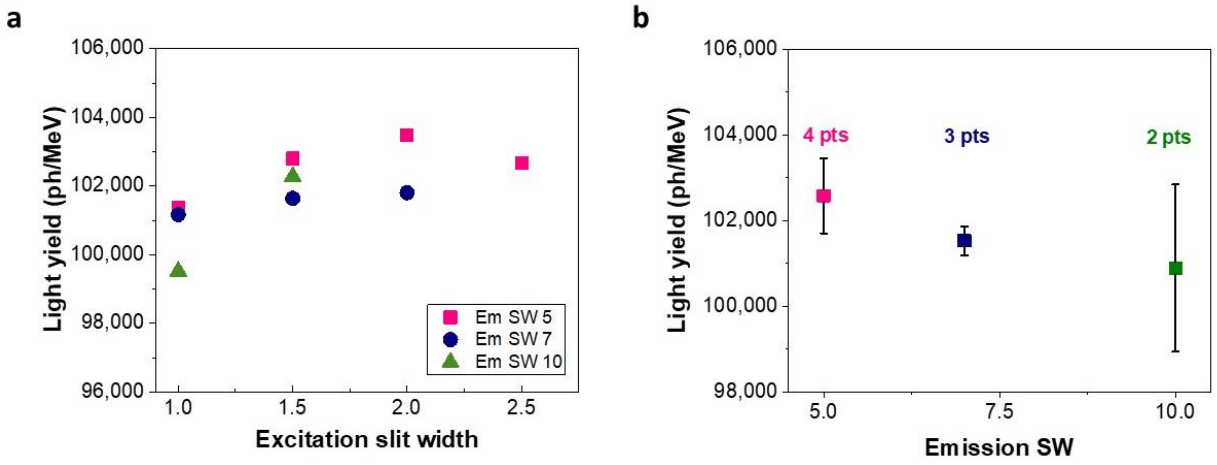

Figure 5.8. The calculated light yield values for 5% Yb-doped $CsPbCl_3$ under X-ray tube irradiation. **a)** Light yield values with varying excitation and emission slit widths and **b)** the average and standard deviation with varying emission slit width only.

5.3.7 Light yield of QD-doped $MAPbBr_3$

The light yields of QD-doped $MAPbBr_3$ were calculated using an energy deposited value of $2.4x10^7$ MeV, a conservative value obtained from the above experiments. Excitation slit widths for the reference light was varied from 2 to 5 mm in increments of 0.5 mm to ensure that experimental parameters did not affect light yield values. Power meter measurements of 1150 nm reference light are plotted against excitation slit width, integrated area of the detector response

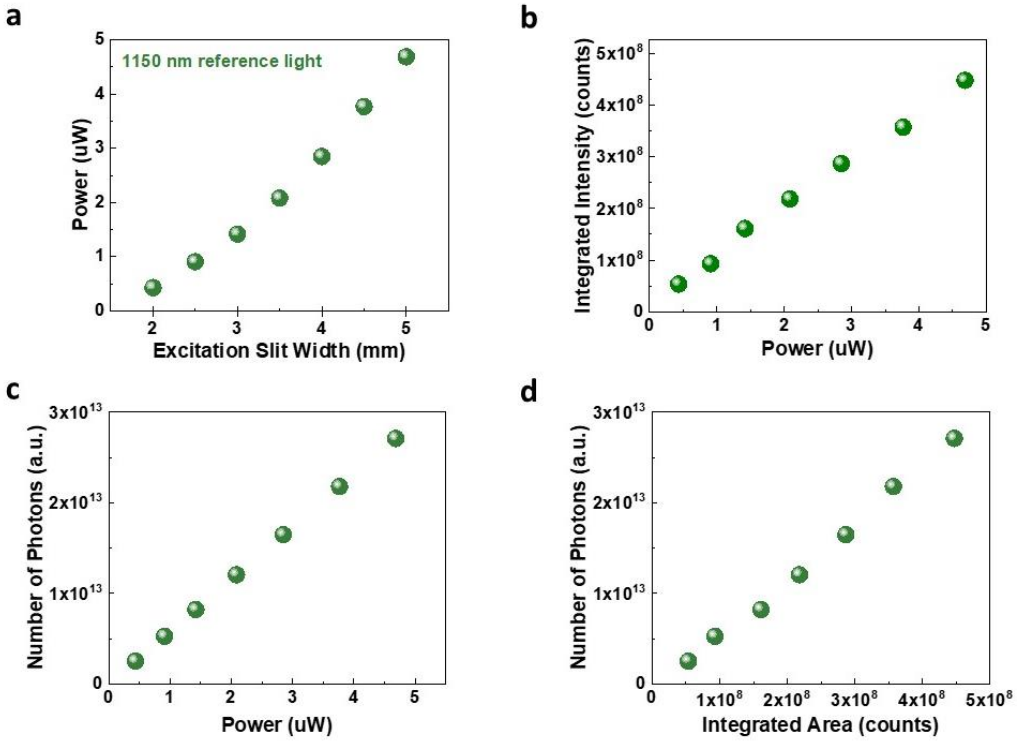

Figure 5.9. Reference light of 1150 nm was used to determine the light yield of QD-doped $MAPbBr_3$ scintillators (QD size 3.8 nm). **a)** Excitation slit width was altered to vary the power (number of photons) of reference light. **b)** The power of the reference light and the corresponding integrated intensity values show that the detector response is linear for the selected intensities. **c)** The number of photons as calculated from the power readings. **d)** The number of photons measured by the power meter was correlated to the integrated intensities to illustrate the correlation between photons detector response.

peak, and number of photons in **Fig. 5.9a-c**. A linear relationship between the integrated area of the reference light peak as measured using the PMT detector is shown in **Fig. 5.9d**, demonstrating that we are within the linear regime of the detector at this wavelength. A plot of the excitation slit width and power meter readings of 1250 nm reference light and the linear relationship with integrated counts from the PMT detector is shown in **Fig. 5.10a-b.**

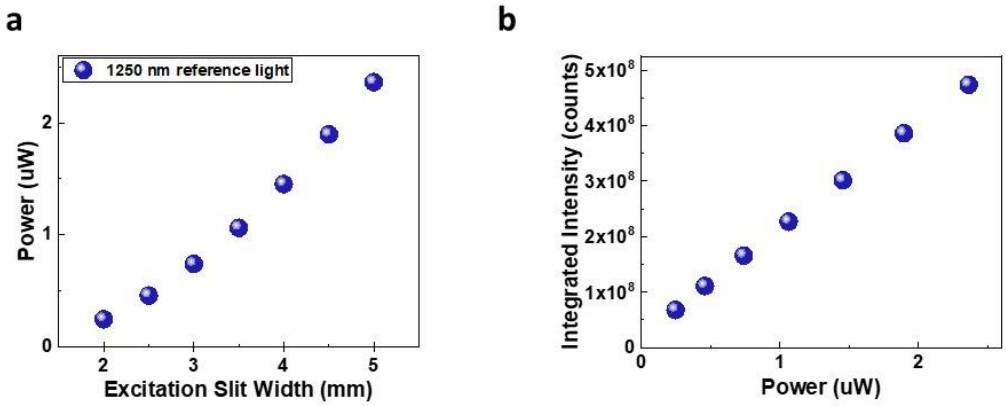

Figure 5.10. Reference light of 1250 nm was used to determine the light yield of QD-doped $MAPbBr_3$ scintillators (QD size 4.3 nm). **a)** Excitation slit width was altered to vary the power (number of photons) of reference light. **b)** The power of the reference light and the corresponding integrated intensity values show that the detector response is linear for the selected intensities.

Emission slit width was not able to be varied using the selected wavelengths for reference light (1150 nm, and 1250 nm for 3.8 nm and 4.3 nm QDs, respectively) due to detector saturation restrictions. QD-doped $MAPBBr_3$ scintillated emission was measured using a large emission slit width of 12 mm, and thus the 1150 nm and 1250 nm reference light intensities were dampened with neutral density filters of 2.0 and 1.0, respectively. The measured reference light intensities were corrected with their documented wavelength-dependent transmission factors post-measurement.

Light yields were calculated for $MAPbBr_3$ doped with 3.8 nm and 4.3 nm lead sulfide quantum dots (**Fig. 5.10a-b**) Calculated light yield values deviated slightly with varying excitation slit width, but ultimately provided reasonably agreeable light yield values. The averages and standard deviations of light yield values for QD-doped $MAPbBr_3$ are documented in Chapter 7.

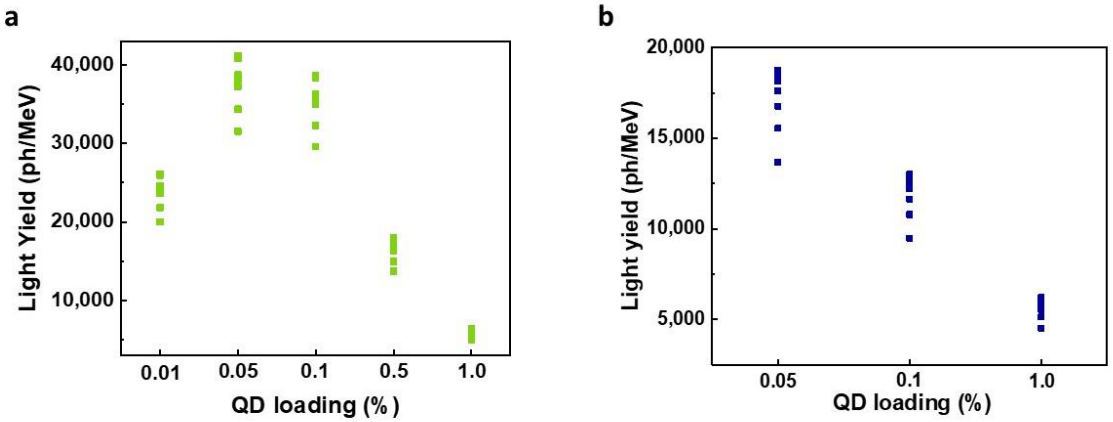

Figure 5.11. Calculated light yield values of QD-doped $MAPbBr_3$ with QD size **a)** 3.8 nm and **b)** 4.3 nm. The spread of light yield values here were calculated using a range of reference light intensities.

5.4. Conclusion

A methodology for measuring the light yield using a continuous spectrum X-ray source was developed. X-rays ranging from less than 10 keV up to 40 keV produced via Bremsstrahlung radiation was used to excite scintillators and the scintillated emission was measured using visible and infrared region photomultiplier tube detectors. A reference light matching the maximum scintillated emission in conjunction with power meter measurements was used to calculated the number of scintillated photons. By assuming total attenuation of X-rays by all scintillators used in this study, the amount of energy deposited in each material was equivalent. Using CaF_2(Eu) and CsI(TI) commercial scintillators with known light yields, the energy deposited value was calculated and corrected for non-proportionality. Finally, the light yields of Yb-doped $CsPbCl_3$ and quantum-dot-doped $MAPbBr_3$ was calculated.

5.5 References

(1) Klamra, W.; Sibczynski, P.; Moszyński, M.; Kozlov, V. Light Yield Nonproportionality of Doped CeF3scintillators. *Journal of Instrumentation* **2014**, *9* (07), P07013–P07013. https://doi.org/10.1088/1748-0221/9/07/p07013.

(2) W. Mengesha; T. D. Taulbee; B. D. Rooney; J. D. Valentine. Light Yield Nonproportionality of CsI(Tl), CsI(Na), and YAP. *IEEE Transactions on Nuclear Science* **1998**, *45* (3), 456–461. https://doi.org/10.1109/23.682426.

Chapter 6: Ytterbium-Doped Cesium Lead Chloride Perovskite as an X-ray Scintillator with High Light Yield

Contributors: Ashley M. Conley, Katelyn A. Dagnall,* Lucy U. Yoon, Haritha S. Rajeev, Seung-Hun Lee, Joshua J. Choi*

** - equal contribution)*

6.1 Abstract

Ytterbium doped cesium lead halides are quantum cutting materials with exceptionally high photoluminescence quantum yields, making them promising materials as scintillators. In this work, we report ytterbium-doped cesium lead chloride (Yb^{3+}:$CsPbCl_3$) with an X-ray scintillation light yield of 102,000 photons/MeV at room temperature, which is brighter than the current state-of-the-art commercial scintillators. The high light yield was achieved based on a novel method of synthesizing Yb^{3+}:$CsPbCl_3$ powders using water and low-temperature processing. The combination of high light yield, and the simple and inexpensive manufacturing method reported in this work demonstrates the great potential of Yb^{3+}:$CsPbCl_3$ for scintillation applications.

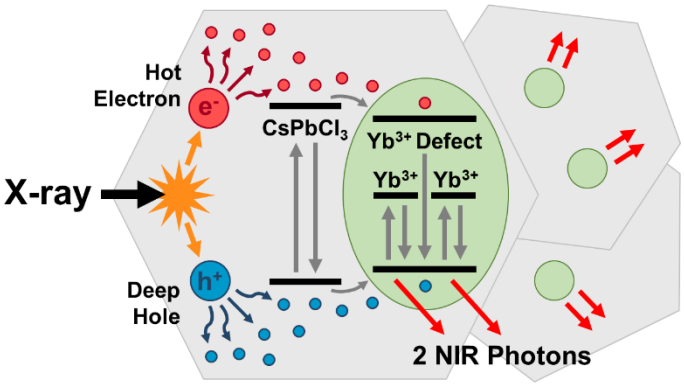

Figure 6.1. Quantum cutting mechanism of Yb^{3+}:$CsPbCl_3$ for ionizing radiation detection.

6.2 Introduction

Detection of X-ray photons is critically important in various fields, such as security, medical radiography, industrial manufacturing and astronomy[1–5]. Scintillators play key roles in many of these applications by absorbing X-ray photons and emitting visible or near-infrared photons for detection with conventional photodetectors. However, the state-of-the-art commercial scintillators are manufactured using complex fabrication methods such as single crystal growth at high temperature (~1700 °C) which make their cost prohibitively high for applications that require large area detection.[6,7] Alternatives such as plastic scintillators[8,9] can be inexpensively manufactured into large dimensions at low temperature but they are not commonly used in high-energy X-ray systems due to their low stopping power, low light yield and poor energy resolution that do not meet the performance criteria.

Metal halide perovskites (MHPs) have recently been identified as promising scintillator materials.[10,11] MHPs are low-bandgap (1.6-2.2 eV) materials composed of high-Z atoms with chemical composition of ABX_3, where A = Cs^+, $CH_3NH_3^+$, etc., B = Pb^{2+}, Sn^{2+} and X = Cl^-, Br^-, I^-. With a combination of relatively high effective atomic number, high density and low bandgap, MHPs are efficient hard radiation absorbers with potential light yields as high as 250,000 photons/MeV.[12–14] MHPs are composed of entirely earth abundant, low-cost elements and can be synthesized into single crystals, polycrystalline powders or thin films using simple solution processing methods at low temperatures (25-150 °C). Therefore, MHP based scintillators are expected to be drastically cheaper compared to current commercial scintillators.[15] Even in highly defective polycrystalline forms, MHPs exhibit low charge trapping due to defect tolerance.[16,17] For this reason, charge carrier diffusion length can be as long as few microns in polycrystalline MHP

powders synthesized at low temperature.[18] These attributes can be exploited to obtain high performance in optoelectronic devices such as solar cells and photodetectors.

However, pure MHP compositions by themselves have so far demonstrated limited scintillation performance due to the low exciton binding energy in MHPs suppresses formation of excitons and radiative recombination and liquid nitrogen temperatures were required to obtain higher light yield.[10,19] Formation of nanostructured MHPs into quantum dots or quantum wells to increase the exciton binding energy has shown to increase the light yield[20,21] but at the expense of increased bandgap and drastic cost increase associated with nanoparticle synthesis. Moreover, pure MHP composition scintillators suffer from the large overlap between photoluminescence and absorbance spectra which causes reabsorption of emitted photons.

In this work, we sought to address all of the challenges mentioned above using ytterbium (Yb^{3+}) doped cesium lead chloride perovskites (Yb^{3+}:$CsPbCl_3$) as scintillators. Doping of cesium lead halide ($CsPbX_3$) with Yb^{3+} can boost the photoluminescence quantum yield (PLQY) above 100% through the quantum cutting process[22–30] wherein one photon absorbed by the $CsPbX_3$ matrix can be converted into two photons emitted from the Yb^{3+} dopants. The bright emission through the quantum cutting process, combined with high atomic number compositions, makes Yb^{3+}:$CsPbCl_3$ compelling for scintillator applications, and yet there has been no report on scintillation from Yb^{3+} doped MHPs. In this paper, we report a novel method of synthesizing Yb^{3+}:$CsPbCl_3$ powders using only water as the solvent and mild thermal annealing (below 200 °C). Our manufacturing method can produce a large quantity of Yb^{3+}:$CsPbCl_3$ powder in a low-cost and scalable fashion. The Yb^{3+}:$CsPbCl_3$ powder can be sintered into any shape and size for various target applications. Radioluminescence activity was optimized as a function of Yb doping amount. The highest performance was achieved with 5 mol% Yb doping amount Yb^{3+}:$CsPbCl_3$

with light yield of 102,000 photons/MeV under room temperature operation, which is higher than light yields of state-of-the-art commercial scintillators. The Yb^{3+}:$CsPbCl_3$ powder was pressed into a pellet for radiographic imaging of various objects with a complementary metal-oxide-semiconductor (CMOS) photodetector. Our results demonstrate the promising potential of Yb^{3+}:$CsPbCl_3$ for scintillators that can simultaneously achieve high performance, large area detection and low-cost.

6.3 Results and Discussion

6.3.1 Fabrication of Yb^{3+}:$CsPbCl_3$ powders

The Yb^{3+}:$CsPbCl_3$ powder samples were prepared using simple solution processing with water as the solvent, as illustrated in **Fig. 6.2a**. Stoichiometric amounts of cesium chloride (CsCl), lead chloride ($PbCl_2$), and ytterbium chloride ($YbCl_3$) precursors were combined in de-ionized water, stirred at 40 °C for one hour, after which the water was removed through evaporation at 65 °C. The resultant powder was then finely crushed in a mortar and pestle, and annealed at 200 °C for one hour, with mechanical stirring and mixing during the process. Seven powder samples were produced with varying Yb^{3+} ion content from 0.5 mol% up to 60 mol%.

6.3.2 Structural and compositional characterization

The X-ray diffraction (XRD) patterns of the Yb^{3+}:$CsPbCl_3$ samples are shown in **Fig. 6.2b**, along with a reference pattern of the orthorhombic structural phase (*Pnma*) of $CsPbCl_3$. The XRD patterns from Yb^{3+}:$CsPbCl_3$ with less than 25% Yb^{3+} content match well to the $CsPbCl_3$ reference pattern, in agreement with previous reports which show that Yb^{3+} doping at low concentrations retain the bulk $CsPbCl_3$ crystal structure.[31] The orthorhombic (*Pnma*) structure of these powder

samples is consistent with Yb^{3+}:$CsPbCl_3$ powders formed through solid state reaction[31] and mechanochemical synthesis[32] and is in contrast with the cubic ($Pm\overline{3}m$) structure of Yb^{3+}:$CsPbCl_3$ nanocrystals and quantum dots.[22,33–35] The well-matched patterns between $CsPbCl_3$ and Yb^{3+}:$CsPbCl_3$ at and below 5% Yb^{3+} content, without any presence of peaks from precursor materials and other possible phases, suggest that the Yb^{3+} ions are incorporated into the $CsPbCl_3$ host lattice through placement into the Pb^{2+} sites. The (101) peak location does not shift significantly as a function of Yb^{3+} amount, suggesting that the substitution of the smaller Yb^{3+} ion in the Pb^{2+} position does not result in any significant lattice compression. In the 25%, 45%, and 60% Yb^{3+}:$CsPbCl_3$ compositions, XRD peaks not matching to the $CsPbCl_3$ structure were

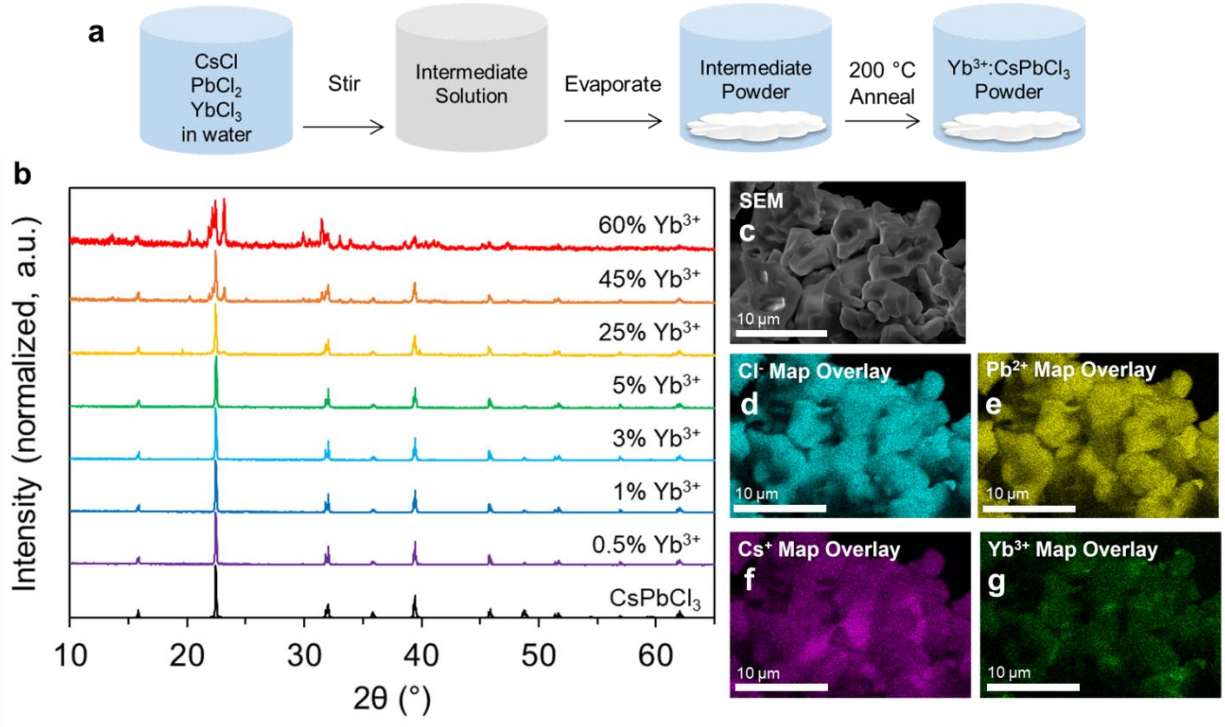

Figure 6.2. Synthesis and physical characterization of Yb^{3+}:$CsPbCl_3$ powders. **a)** Schematic of Yb^{3+}:$CsPbCl_3$ synthesis process. **b)** X-ray diffraction patterns of Yb^{3+}:$CsPbCl_3$ samples with different Yb content and the orthorhombic phase of $CsPbCl_3$. **c)** Scanning electron microscopy image of a 5% Yb^{3+}:$CsPbCl_3$ powder sample. **d**,**e**,**f**,**g**) Energy dispersive X-ray spectroscopy overlay of Cl^-, Pb^{2+}, Cs^+, and Yb^{3+}.

observed, indicating the presence of impurity species at these higher Yb^{3+} doping concentrations. These results show that our water based and low-temperature synthesis method results in high purity Yb:$CsPbCl_3$ with the Yb^{3+} dopants substituted into the Pb^{2+} sites in the lattice in Yb^{3+} concentrations at and below 5%.

The morphology of the 5% Yb^{3+}:$CsPbCl_3$ powder is shown in the scanning electron microscopy (SEM) image in **Fig. 6.2c**. The powder was found to be composed of micrometer scale grains. Energy dispersive X-ray spectroscopy (EDS) images show that the Cl^-, Pb^{2+}, Cs^+, and Yb^{3+} are distributed throughout the entirety of the grains (**Fig. 6.2d-g**). Few areas of higher concentration of Cs^+ and Yb^{3+} were observed (**Fig. 6.2f-g**) which suggests that there are some regions of the samples with higher Yb^{3+} concentration. The average surface elemental composition of the 5% Yb^{3+}:$CsPbCl_3$ sample obtained through EDS shows that the Yb^{3+} doping amount is close to the stoichiometric amounts of precursor used in the synthesis based on the measured Yb^{3+} to Pb^{2+} ratios (**Table 6.1**).

Element	Nominal Mole Fraction	Average Measured Mole Fraction
Cs	1	1.4499
Yb	0.05	0.0450
Pb	0.925	0.925
Cl	3	3.1856

Table 6.1. Elemental composition of 5% Yb^{3+}:$CsPbCl_3$ powder, as measured by EDXS using three averaged points with moles of Pb^{2+} as the calculation reference.

6.3.3 Optical Characterization

The absorbance and photoluminescence spectra of 5% Yb^{3+}:$CsPbCl_3$ sample are shown in **Fig. 6.3a**. A spectrophotometer and a spectrofluorometer, both equipped with an integrating sphere, were employed for these measurements to account for any light scattering in the powder samples. Our results show that there is a large Stokes shift between the absorption onset at 440 nm and the photoluminescent emission peak at 1000 nm. This is consistent with previous reports on Yb^{3+}:$CsPbCl_3$ wherein the light absorption occurs in the $CsPbCl_3$ with the onset of 440 nm, and the emission peak at 1000 nm originates from the $^2F_{5/2} \rightarrow {}^2F_{7/2}$ transition in Yb^{3+} ions.[22,23] The photoluminescence from the $CsPbCl_3$ matrix at 406 nm is greatly suppressed as a result of efficient sensitization with the Yb^{3+} ion dopants (inset in Fig. 6.3a). The emission wavelength of 1000 nm is well-matched with silicon photodiodes that are cost effective and widely available for coupling with scintillators in various applications. Moreover, the large Stokes shift is advantageous for scintillator performance as it prevents the re-absorption of radioluminescence photons by the material, enabling increased scintillator thickness without attenuating the emitted photon flux.

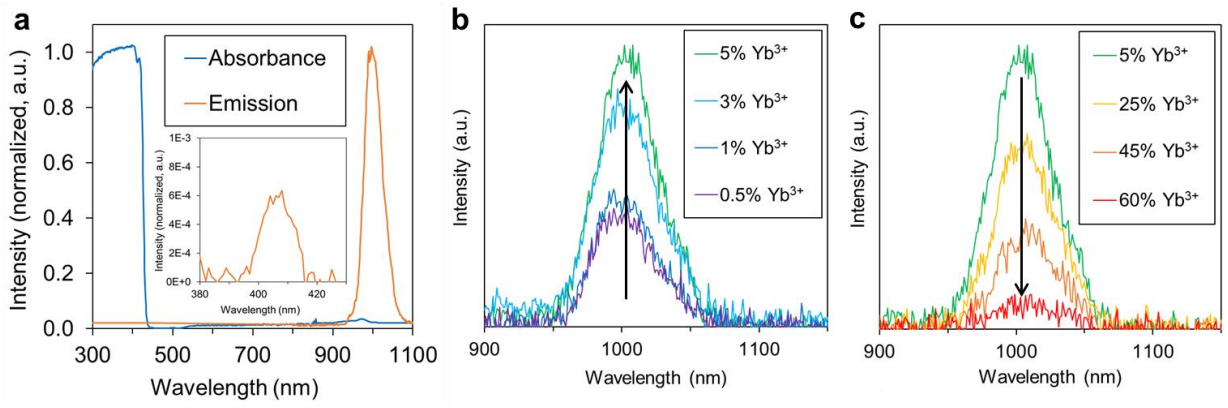

Figure 6.3. Optical characterization and radioluminescence of Yb^{3+}:$CsPbCl_3$ powder. **a)** Absorbance and photoluminescence of 5% Yb^{3+}:$CsPbCl_3$. **b**,**c**) X-ray radioluminescence spectra of 0.5%-5% Yb^{3+}:$CsPbCl_3$ and 5%-60% Yb^{3+}:$CsPbCl_3$.

6.3.4 Scintillation performance of Yb^{3+}:$CsPbCl_3$ with varying Yb^{3+} doping

Radioluminescence spectra of the Yb^{3+}:$CsPbCl_3$ samples were measured using a spectrofluorometer equipped with a Moxtek MAGPRO X-ray source operating at 40 kV and 300 μA. To ensure consistent amounts of excited scintillator material and X-ray excitation conditions, all Yb^{3+}:$CsPbCl_3$ samples in powder form were loaded into identical Kapton capillary tubes and placed into an integrating sphere with consistent sample placement (described in detail in Chapter 5). Our measurements show a trend of increasing radioluminescence intensity from Yb^{3+}:$CsPbCl_3$ samples with increasing Yb^{3+} ion content up to 5% (**Fig. 6.3b**). This is consistent with previous papers that showed larger photoluminescent quantum yields in Yb^{3+} doped $CsPbX_3$ with more Yb^{3+} ions in the low Yb^{3+} concentration regime.[22,23] Our results indicate that similar behavior occurs in radioluminescence emission as well. This is likely caused by more efficient sensitization of Yb^{3+} dopants due to larger number of Yb^{3+} defect complex sites and reduced average distances for charges to travel. However, at above the 5% Yb^{3+} doping level, we observed the opposite trend of decreasing radioluminescence intensity with higher Yb^{3+} concentration (**Fig. 6.3c**). We attribute this to presence of impurity species based on our X-ray diffraction results (Fig. 6.2b), that show an increased amount of impurity species with increasing Yb^{3+} ion content above 5%.

An important performance metric for scintillators is the light yield, which is defined to be the number of photons emitted per absorbed radiation energy. Given the same radiation source, scintillators with higher light yield produce brighter radioluminescence emission for more sensitive detection with photodetectors. In various applications such as medical imaging and national security, sensitive detection of weaker intensity radiation is highly desired. The scintillation light yields of our Yb^{3+}:$CsPbCl_3$ samples, as well as commercially available reference scintillators CaF_2(Eu) and CsI(TI), were quantified using excitation from the X-ray source

operating at 40 kV and 300 μA (see Chapter 5). Consistent with the trend observed in the radioluminescence spectra intensity as a function of Yb^{3+} amount, we found that the 5% Yb^{3+}:$CsPbCl_3$ provided the highest performance with a light yield of 102,000 photons/MeV (**Fig. 6.4a**). This is a significantly higher light yield than the state-of-the-art commercially available scintillators such as CsI(Tl) with a light yield of 65,000 photons/MeV. The high light yield from Yb^{3+}:$CsPbCl_3$ can be attributed to the combination of relatively low bandgap of $CsPbCl_3$, resulting in greater charge carrier generation with high energy radiation absorption, long charge carrier lifetime and diffusion length even in polycrystalline samples[18] and bright emission from the quantum cutting process.[22–30] Previous studies in the context of downconverters for solar cells have found that Yb^{3+} doped $CsPbX_3$ exhibits luminescence saturation at increasing photoexcitation fluences, limiting the emission of the material.[22,27] To check whether our 5% Yb^{3+}:$CsPbCl_3$ sample is limited by the saturation effect, we measured the radioluminescence intensity as a function of excitation X-ray flux. As shown in **Fig. 6.4b**, the photons emitted from the sample varies linearly with the X-ray source current, indicating that saturation does not occur within the operating conditions of the X-ray source employed in this study.

6.3.5 X-ray imaging with a polycrystalline pellet of Yb^{3+}:$CsPbCl_3$

To demonstrate the applicability of our Yb^{3+}:$CsPbCl_3$ for radiographic imaging, a cylindrical pellet of the 5% Yb^{3+}:$CsPbCl_3$ powder sample was manufactured by hydraulically pressing the powder under 6 tons of pressure at 70 °C for 3 hours. Images of various objects under X-ray irradiation formed on the scintillator pellet were captured using a Basler NIR GigE camera. In **Fig. 6.4c**, a thumbtack is shown, in which the embedded metal pin inside the plastic head is

clearly visible. **Fig. 6.4d** shows a micro-SIM phone card, in which the metal contact is differentiated from the plastic casing.

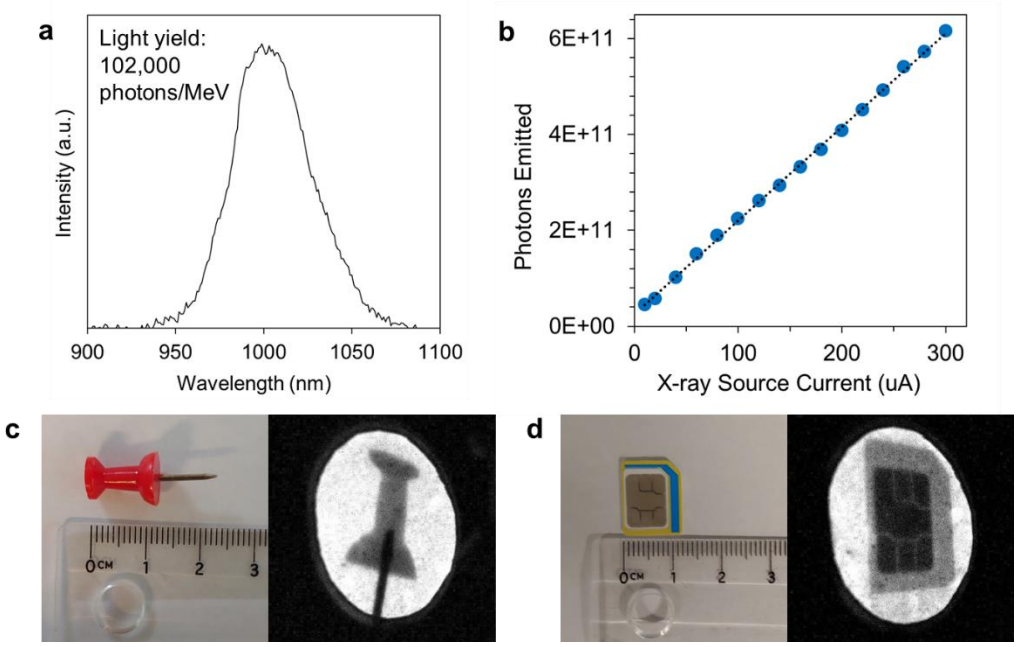

Figure 6.4. Radioluminescence performance and radiographic imaging of 5% Yb^{3+}:$CsPbCl_3$. **a)** X-ray radioluminescence spectrum of 5% Yb^{3+}:$CsPbCl_3$ with light yield of 102,000 photons/MeV. **b)** Linear radioluminescence response of 5% Yb^{3+}:$CsPbCl_3$as a function of X-ray source current. **c**,**d**) X-ray imaging on surface of 25 mm pressed 5% Yb^{3+}:$CsPbCl_3$ powder pellet of a thumbtack, and a micro-SIM card.

6.4 Conclusion

In summary, we have shown the first detection and application of radioluminescence in a Yb^{3+} doped cesium lead halide. Our water-based synthesis method produces Yb^{3+}:$CsPbCl_3$ powder over a wide composition range that shows incorporation of the Yb^{3+} dopant with high purity up to a maximum of 5 mol%. The water evaporation and low-temperature annealing method presented here is among the simplest methods of producing Yb^{3+}:$CsPbX_3$, but does not sacrifice the crystallinity of the $CsPbCl_3$ host lattice. The 5% Yb^{3+}:$CsPbCl_3$ scintillator has a large Stokes shift, and the strong characteristic Yb^{3+} emission at 1,000 nm. Suppressed $CsPbCl_3$ excitonic emission at 406 nm proves evidence of efficient transfer of charge carriers from the bulk lattice to the defect Yb^{3+} emission sites. Radioluminescence is exhibited by all Yb^{3+}:$CsPbCl_3$ samples and is optimized at 5 mol% due to a balance of high Yb^{3+} ion content and high material purity. The champion 5% Yb^{3+}:$CsPbCl_3$ composition has a measured light yield of 102,000 photons/MeV, which is higher than those from the commercial scintillator options. Radiographic imaging was demonstrated using a pressed powder pellet.

6.5 Materials and Methods

6.5.1. Synthesis of Yb^{3+} doped $CsPbCl_3$ powder

Cesium iodide (CsCl, >99.0%) was purchased from Tokyo Chemical Industry (TCI), lead (II) chloride ($PbCl_2$, 99.999%) was purchased from Alfa Aesar, and ytterbium (III) chloride hexahydrate ($YbCl_3 \cdot 6H_2O$, 99.9%-Yb) was purchased from STREM Chemicals. The precursors were combined according to the $Yb_xCsPb_{1-1.5x}Cl_3$ stoichiometry, assuming $2Yb^{3+}$:$1V_{Pb}$ substitution at the Pb^{2+} B-sites, in Yb^{3+} molar percents of 0%, 0.5%, 1%, 3%, 5%, 25%, 45%, and 60%. The precursors were dissolved in de-ionized water at a concentration of 5 g/L, and stirred for 1 hour at 40 °C. The solution was then transferred to a crystallization dish, and the water was slowly evaporated off at a temperature of 65 °C while stirring. The resultant powder was finely crushed using a mortar and pestle, transferred back to the crystallization dish, and annealed for 1 hour at 200 °C, stirring four times during the annealing process. The pressed powder pellet of 5% Yb^{3+}:$CsPbCl_3$ was fabricated using a 25 mm pellet die and an Atlas Manual Hydraulic Press under 6 tons of pressure for 2 hours, while under vacuum at 70 °C.

6.5.2. Physical characterization

X-ray diffraction patterns of the Yb^{3+}:$CsPbCl_3$ powders were measured using an Empyrean Multipurpose X-Ray Diffractometer with a Cu anode, at 45 kV and 40 mA with step size 0.02°. Figure S1 shows the decreasing (101) peak intensity with increasing Yb^{3+} molar concentration in the Yb^{3+}:$CsPbCl_3$ samples. Scanning electron microscopy (SEM) and energy dispersive X-ray spectroscopy (EDXS) were measured on an FEI Quanta 650 Scanning Electron Microscope.

6.5.3. Optical characterization

The steady state photoluminescence (PL) spectra of the 5% Yb^{3+}:$CsPbCl_3$ samples were measured using a PTI QuantaMaster 400 spectrofluorometer, using a Xe arc lamp excitation source monochromatized at a wavelength of 405 nm. The absorbance of the 5% Yb^{3+}:$CsPbCl_3$ sample was measured using a PerkinElmer UV/Vis/NIR Lambda 950S spectrometer equipped with an integrating sphere.

6.5.4. Radioluminescence characterization and light yield calculation

Materials

A Moxtek 60kV 12W MagPro X-ray Imaging Source was used for X-ray generation. Commercial scintillators CaF_2(Eu) and CsI(TI) were purchased from Epic-Crystal Co. with light yields of 19,000 and 60,000 ph/MeV, respectively. Both commercial scintillators were grown via the Bridgeman method and cut to be 25.4 x 25.4 x 25.4 mm^3 cubes with all sides polished. An acrylic glass cube with dimensions 25.4 x 25.4 x 25.4 mm^3 with all sides polished was purchased from U.S. Plastic Corporation. Power meters equipped with a silicon photodiode (PM16-120) and a germanium photodiode (PM16-122) were purchased from Thor Labs. A PTI QuantaMaster 400 spectrofluorometer equipped with a UV-Vis photomultiplier tube (PFR Technologies, LLC, R2658) and NIR photomultiplier tube (Hamamatsu Photonics, H10330-75) was used to measure radioluminescence and reference light signals.

Light yield determination

The light yield of the Yb^{3+}:$CsPbCl_3$, reported in photons per MeV of energy deposited, was determined in two parts. The energy deposited by the X-ray source was quantified using the known light yields of two commercial scintillators, CaF_2(Eu) and CsI(TI). The energy deposited values were corrected for non-proportionality of CaF_2(Eu) and CsI(TI) at the specific keV X-ray energies produced by the X-ray source used in the measurement. To quantify the Yb^{3+}:$CsPbCl_3$ photon output, the power of a reference light source was correlated to the photomultiplier tube (PMT) detector response; correcting for spectral sensitivity of the detector at different wavelengths.

Radioluminescence signals were obtained for the commercial scintillators and the Yb^{3+}:$CsPbCl_3$ scintillators using the Moxtek 60kV 12W MagPro X-ray Imaging Source at 300 µA and 40 kV. All scintillators studied were placed inside an integrating sphere and confirmed to completely absorb the X-ray beam, which was collimated using the inlet of the integrating sphere. All luminescence signals were determined to be within the linear range of the PMT detector and within the documented operating range of the power meters. The reference light power measurements were performed and cross-checked using both a silicon photodiode power meter and a germanium photodiode power meter.

Powder sample preparation

Powder samples were packed into 12 Kapton capillaries purchased from Cole-Parmer (0.0710” ID, 0.0750” OD, cut to a length of 50 mm). Capillaries were sealed on both ends with Sigillum Wax Sealant purchased from Thomas Scientific and arranged into two rows of six, which was confirmed to achieve total attenuation of X-rays.

Quantifying photon output of scintillators

The photon output of the xenon lamp light source with a monochromator was used in conjunction with a power meter and PMT detector to determine the photon output of the commercial CaF_2(Eu) and CsI(TI) scintillators and the Yb^{3+}:$CsPbCl_3$ scintillators. Wavelengths matching the emission of commercial and Yb^{3+}:$CsPbCl_3$ scintillators were selected for the reference light power meter measurements, as detailed in Table S2. The reference light was scattered in the same geometry as the scintillators. To match the commercial CaF_2(Eu) and CsI(TI) scintillators, the reference light measurement was performed with a polished glass cube with the same dimensions and geometry as the commercial scintillators inside an integrating sphere. For the Yb^{3+}:$CsPbCl_3$ scintillators, the reference light was scattered using $CsPbCl_3$ powder in the same capillary configuration and with the same geometry as the Yb^{3+}:$CsPbCl_3$ scintillator. The number of emitted photons from each scintillator was calculated with calibration using reference light power measurements and PMT detector counts.

6.5.5. Radiographic imaging

Radiographic images were captured using a Basler ace acA1300-60gm-NIR GigE camera with a 4.5 mm C Series VIS-NIR fixed focal length lens. The images were captured on the surface of the 25 mm 5% Yb^{3+}:$CsPbCl_3$ pressed powder pellet using the benchtop X-ray source at 40 kV and 300 μA, and a 5.5 s exposure time.

6.6 Contributions

Ashley Conley developed scintillation-related characterization methods. Katelyn Dagnall developed the scintillator materials and performed structural and optical characterization. Joshua Choi conceived the project.

6.7 References

(1) Withers, P. J.; Bouman, C.; Carmignato, S.; Cnudde, V.; Grimaldi, D.; Hagan, C. K.; Maire, E.; Manley, M.; Du Plessis, A.; Stock, S. R. X-ray computed tomography. *Nat. Rev. Methods Primers.* **2021**, *1* (18). DOI: 10.1038/s43586-021-00015-4

(2) Bailes, M.; Berger, B. K.; Brady, P. R.; Branchesi, M.; Danzmann, K.; Evans, M.; Holley-Bockelmann, K.; Iyer, B. R.; Kajita, T.; Katsanevas, S.; Kramer, M.; Lazzarini, A.; Lehner, L.; Losurdo, G.; Lück, H.; McClelland, D. E.; McLaughlin, M. A.; Punturo, M.; Ransom, S.; Raychaudhury, S.; Reitze, D. H.; Ricci, F.; Rowan, S.; Saito, Y.; Sanders, G. H.; Sathyaprakash, B. S.; Schutz, B. F.; Sesana, A.; Shinkai, H.; Siemens, X.; Shoemaker, D. H.; Thorpe, J.; van den Brand, J. F. J.; Vitale, S. Gravitational-wave physics and astronomy in the 2020s and 2030s. *Nat. Rev. Phys*. 2021, *3*, 344–366. DOI: 10.1038/s42254-021-00303-8

(3) Günther, S.; Reinke, P. Y. A.; Fernández-García, Y.; Lieske, J.; Lane, T. J.; Ginn, H. M.; Koua, F. H. M.; Ehrt, C.; Ewert, W.; Oberthuer, D.; Yefanov, O.; Meier, S.; Lorenzen, K.; Krichel, B.; Kopicki, J. D.; Gelisio, L.; Brehm, W.; Dunkel, I.; Seychell, B.; Gieseler, H.; Norton-Baker, B.; Escudero-Pérez, B.; Domaracky, M.; Saouane, S.; Tolstikova, A.; White, T. A.; Hänle, A.; Groessler, M.; Fleckenstein, H.; Trost, F.; Galchenkova, M.; Gevorkov, Y.; Li, C.; Awel, S.; Peck, A.; Barthelmess, M.; Schlünzen, F.; Lourdu Xavier, P.; Werner, N,; Andaleeb, H.; Ullah, N.; Falke, S.; Srinivasan, V.; França, B. A.; Schwinzer, M.; Brognaro, H.; Rogers, C.; Melo, D.; Zaitseva-Doyle, J. J.; Knoska, J.; Peña-Murillo, G. E.; Mashhour, A. R.; Hennicke, V.; Fischer, P.; Hakanpää, J.; Meyer, J.; Gribbon, P.; Ellinger,

B.; Kuzikov, M.; Wolf, M.; Beccari, A. R.; Bourenkov, G.; von Stetten, D.; Pompidor, G.; Bento, I.; Panneerselvam, S.; Karpics, I.; Schneider, T. R.; Garcia-Alai, M. M.; Niebling, S.; Günther, C.; Schmidt, C.; Schubert, R.; Han, H.; Boger, J.; Monteiro, D. C. F.; Zhang, L.; Sun, X.; Pletzer-Zelgert, J.; Wollenhaupt, J.; Feiler, C. G.; Weiss, M. S.; Schulz, E. C.; Mehrabi, P.; Karničar, K.; Usenik, A.; Loboda, J.; Tidow, H.; Chari, A.; Hilgenfeld, R.; Uetrecht, C.; Cox, R.; Zaliani, A.; Beck, T.; Rarey, M.; Günther, S.; Turk, D.; Hinrichs, W.; Chapman, H. N.; Pearson, A. R.; Betzel, C.; Meents, A. X-ray screening identifies active site and allosteric inhibitors of SARS-CoV-2 main protease. *Science* **2021**, *372* (6542) 642–646. DOI: 10.1126/science.abf7945

(4) Stromswold, D. C.; Siciliano, E. R.; Schweppe, J. E.; Ely, J. H.; Milbrath, B. D.; Kouzes, R. T.; Geelhood, B. D. Comparison of plastic and NaI(Tl) scintillators for vehicle portal monitor applications. *IEEE Nucl. Sci. Symp. Conf. Rec.* **2004**, *2* 1065–1069. DOI: 10.1016/j.nima.2005.05.056

(5) Glodo, J.; Wang, Y.; Shawgo, R.; Brecher, C.; Hawrami, R. H.; Tower, J.; Shah, K. S. New Developments in Scintillators for Security Applications. *Phys. Procedia* **2017**, *90* 285–290. DOI: 10.1016/j.phpro.2017.09.012

(6) Nikl, M.; Yoshikawa, A. Recent R&D Trends in Inorganic Single-Crystal Scintillator Materials for Radiation Detection. *Adv. Opt. Mater.* **2015**, *3* (4), 463–481. DOI: 10.1002/adom.201400571

(7) Dujardin, C.; Auffray, E.; Bourret-Courchesne, E.; Dorenbos, P.; Lecoq, P.; Nikl, M.; Vasil'ev, A. N.; Yoshikawa, A.; Zhu, R.-Y. Needs, trends, and advances in inorganic scintillators. *IEEE Trans. Nucl. Sci.* **2018**, *65* (8), 1977–1997. DOI: 10.1109/TNS.2018.2840160

(8) Hajagos, T. J.; Liu, C.; Cherepy, N. J.; Pei, Q. High-Z Sensitized Plastic Scintillators : A Review. *Adv. Mater.* **2018**, *30* (27), 1706956. DOI: 10.1002/adma.201706956

(9) Bertrand, G. H. V.; Hamel, M.; Sguerra, F. Current Status on Plastic Scintillators Modifications. *Chem. – A Eur. J.* **2014**, *20* (48), 15660–15685. DOI: 10.1002/chem.201404093

(10) Zhou, Y.; Chen, J.; Bakr, O. M.; Mohammed, O. F. Metal Halide Perovskites for X-ray Imaging Scintillators and Detectors. *ACS Energy Lett.* **2021**, *6* (2), 739–768. DOI: 10.1021/acsenergylett.0c02430

(11) Maddalena, F.; Tjahjana, L.; Xie, A.; Arramel; Zeng, S.; Wang, H.; Coquet, P.; Drozdowski, W.; Dujardin, C.; Dang, C.; Birowosuto, M.D. Inorganic, Organic, and Perovskite Halides with Nanotechnology for High–Light Yield X- and γ-ray Scintillators. *Crystals* **2019**, *9* (2), 88. DOI: 10.3390/cryst9020088

(12) Xie, A.; Nguyen, T. -H.; Hettiarachchi, C.; Witkowski, M. E.; Drozdowski, W.; Danang Birowosuto, M.; Wang, H.; Dang, C. Thermal Quenching and Dose Studies of X-ray Luminescence in Single Crystals of Halide Perovskites. *J. Phys. Chem. C* **2018**, *122* (28), 16265–16273. DOI: 10.1021/acs.jpcc.8b03622

(13) Wei, H.; Fang, Y.; Mulligan, P.; Chuirazzi, W.; Fang, H.; Wang, C.; Ecker, B. R.; Gao, Y.; Antonietta Loi, M.; Cao, L.; Huang, J. Sensitive X-ray detectors made of methylammonium lead tribromide perovskite single crystals. *Nat. Photonics* **2016**, *10*, 333–339. DOI: 10.1038/nphoton.2016.41

(14) Yakunin, S.; Sytnyk, M.; Kriegner, D.; Shrestha, S.; Richter, M.; Matt, G. J.; Azimi, H.; Brabec, C. J.; Stangl, J.; Kovalenko, M. V.; Heiss, W. Detection of X-ray photons by solution-processed lead halide perovskites. *Nat. Photonics* **2015**, *9*, 444–449. DOI: 10.1038/nphoton.2015.82

(15) Moseley, O. D. I.; Doherty, T. A. S.; Parmee, R.; Anaya, M.; Stranks, S. D. Halide perovskites scintillators: unique promise and current limitations. *J. Mater. Chem. C* **2021**, *9*, 11588–11604. DOI: 10.1039/d1tc01595h

(16) Kim, G. W.; Petrozza, A. Defect Tolerance and Intolerance in Metal-Halide Perovskites. *Adv. Energy Mater.* **2020**, *10* (37), 1–6. DOI: 10.1002/aenm.202001959

(17) Chu, W.; Zheng, Q.; Prezhdo, O. V.; Zhao, J.; Saidi, W. A. Low-frequency lattice phonons in halide perovskites explain high defect tolerance toward electron-hole recombination. *Sci. Adv.* **2020**, *6* (7). DOI: 10.1126/sciadv.aaw7453

(18) Stranks, S. D.; Eperon, G. E.; Grancini, G.; Menelaou, C.; Alcocer, M. J. P.; Leijtens, T.; Herz, L. M.; Petrozza, A.; Snaith, H. J. Electron-Hole Diffusion Lengths Exceeding 1 Micrometer in an Organometal Trihalide Perovskite Absorber. *Science* **2013**, *342* (6156), 341–344. DOI: 10.1126/science.1243982

(19) Mykhaylyk, V. B.; Kraus, H.; Kapustianyk, V.; Kim, H. J.; Mercere, P.; Rudko, M.; Da Silva, P.; Antonyak, O.; Dendebera, M. Bright and fast scintillations of an inorganic halide perovskite $CsPbBr_3$ crystal at cryogenic temperatures. *Sci. Rep.* **2020**, *10*, 1–11. DOI: 10.1038/s41598-020-65672-z

(20) Chen, Q.; Wu, J.; Ou, X.; Huang, B.; Almutlaq, J.; Zhumekenov, A. A.; Guan, X.; Han, S.; Liang, L.; Yi, Z.; Li, J.; Xie, X.; Wang, Y.; Li, Y.; Fan, D.; The. D. B. L.; All, A. H.; Mohammed, O. F.; Bakr, O. M.; Wu, T.; Bettinelli, M.; Yang, H.; Huang, W.; Liu, X.; All-inorganic perovskite nanocrystal scintillators. *Nature* **2018**, *561* (7721), 88–93. DOI: 10.1038/s41586-018-0451-1

(21) Li, X.; Meng, C.; Huang, B.; Yang, D.; Xu, X.; Zeng, H. All-Perovskite Integrated X-Ray Detector with Ultrahigh Sensitivity. *Adv. Opt. Mater.* **2020**, *8* (12), 1–8. DOI: 10.1002/adom.202000273

(22) Milstein, T. J.; Kroupa, D. M.; Gamelin, D. R. Picosecond Quantum Cutting Generates Photoluminescence Quantum Yields over 100% in Ytterbium-Doped $CsPbCl_3$ Nanocrystals. *Nano Lett.* **2018**, *18* (6), 3792–3799. DOI: 10.1021/acs.nanolett.8b01066

(23) Kroupa, D. M.; Roh, J. Y.; Milstein, T. J.; Creutz, S. E.; Gamelin, D. R. Quantum-Cutting Ytterbium-Doped $CsPb(Cl_{1-x}Br_x)_3$ Perovskite Thin Films with Photoluminescence Quantum Yields over 190%. *ACS Energy Lett.* **2018**, *3* (10), 2390–2395. DOI: 10.1021/acsenergylett.8b01528

(24) Ferro, S. M.; Wobben, M.; Ehrler, B. Rare-earth quantum cutting in metal halide perovskites - a review. *Mater. Horizons* **2021**, *8*, 1072–1083. DOI: 10.1039/d0mh01470b

(25) Li, X.; Duan, S.; Liu, H.; Chen, G.; Luo, Y.; Ågren, H. Mechanism for the Extremely Efficient Sensitization of Yb 3+ Luminescence in $CsPbCl_3$ Nanocrystals. *J. Phys. Chem.*

Lett. **2019**, *10* (3), 487–492. DOI: 10.1021/acs.jpclett.8b03406

(26) Pan, G.; Bai, X.; Yang, D.; Chen, X.; Jing, P.; Qu, S.; Zhang, L.; Zhou, D.; Zhu, J.; Xu, W.; Dong, B.; Song, H. Doping Lanthanide into Perovskite Nanocrystals: Highly Improved and Expanded Optical Properties. *Nano Lett.* **2017**, *17* (12), 8005–8011. DOI: 10.1021/acs.nanolett.7b04575

(27) Erickson, C. S.; Crane, M. J.; Milstein, T. J.; Gamelin, D. R. Photoluminescence Saturation in Quantum-Cutting Yb^{3+}-Doped $CsPb(Cl_{1-x}Br_x)_3$ Perovskite Nanocrystals: Implications for Solar Downconversion. *J. Phys. Chem. C* **2019**, *123* (19), 12474–12484. DOI: 10.1021/acs.jpcc.9b01296

(28) Zhou, D.; Liu, D.; Pan, G.; Chen, X.; Li, D.; Xu, W.; Bai, X.; Song, H. Cerium and Ytterbium Codoped Halide Perovskite Quantum Dots: A Novel and Efficient Downconverter for Improving the Performance of Silicon Solar Cells. *Adv. Mater.* **2017**, *29* (42), 3–8. DOI: 10.1002/adma.201704149

(29) Cohen, T. A.; Milstein, T. J.; Kroupa, D. M.; MacKenzie, J. D.; Luscombe, C. K.; Gamelin, D. R. Quantum-cutting Yb^{3+}-doped perovskite nanocrystals for monolithic bilayer luminescent solar concentrators. *J. Mater. Chem. A* **2019**, *7*, 9279–9288. DOI: 10.1039/c9ta01261c

(30) Zhang, X.; Zhang, Y.; Zhang, X.; Yin, W.; Wang, Y.; Wang, H.; Lu, M.; Li, Z.; Gu, Z.; Yu, W. W. Yb^{3+} and Yb^{3+}/Er^{3+} doping for near-infrared emission and improved stability of $CsPbCl_3$ nanocrystals. *J. Mater. Chem. C* **2018**, *6*, 10101–10105. DOI: 10.1039/c8tc03957g

(31) Stefanski, M.; Ptak, M.; Sieradzki, A.; Strek, W. Optical characterization of Yb^{3+}:$CsPbCl_3$ perovskite powder. *Chem. Eng. J.* **2021**, *408*, 127347. DOI: 10.1016/j.cej.2020.127347

(32) Crane, M. J.; Kroupa, D. M.; Roh, J. Y.; Anderson, R. T.; Smith, M. D.; Gamelin, D. R. Single-Source Vapor Deposition of Quantum-Cutting Yb^{3+}:$CsPb(Cl_{1-x}Br_x)_3$ and Other Complex Metal-Halide Perovskites. *ACS Appl. Energy Mater.* **2019**, *2* (6), 4560–4565. DOI: 10.1021/acsaem.9b00910

(33) Lesage, A.; van der Laan, M.; Gomez, L.; Gregorkiewicz, T. Substitutional Doping of Yb^{3+} in $CsPbBr_xCl_{3-x}$ Nanocrystals. *J. Phys. Chem. C* **2020**, *124* (11), 6413–6417. DOI: 10.1021/acs.jpcc.9b11393

(34) Ma, J. P.; Chen, Y. -M.; Zhang, L. -M.; Guo, S. –Q.; Liu, J. –D.; Li, H.; Ye, B. –J.; Li, Z. –Y.; Zhou, Y.; Zhang, B. –B.; Bakr, O. M.; Zhang, J. –Y.; Sun, H. –T. Insights into the local structure of dopants, doping efficiency, and luminescence properties of lanthanide-doped $CsPbCl_3$ perovskite nanocrystals. *J. Mater. Chem. C* **2019**, *7*, 3037–3048. DOI: 10.1039/c9tc00237e

(35) Zhou, L.; Liu, T.; Zheng, J.; Yu, K.; Yang, F.; Wang, N.; Zuo, Y.; Liu, Z.; Xue, C.; Li, C.; Cheng, B.; Wang, Q. Dual-Emission and Two Charge-Transfer States in Ytterbium-doped Cesium Lead Halide Perovskite Solid Nanocrystals. *J. Phys. Chem. C* **2018**, *122* (47), 26825–26834. DOI: 10.1021/acs.jpcc.8b07906

Chapter 7: Quantum-dot-doped lead halide perovskites for ionizing radiation detection

Contributors: *Ashley M. Conley, Ephraiem S. Sarabamoun, Katelyn A. Dagnall, Lucy U. Yoon, Haritha S. Rajeev, Seung-Hun Lee, and Joshua J. Choi**

This chapter has been submitted for publication.

7.1 Abstract

High performance scintillators are essential for medical imaging, security, high-energy physics, and others. Lead halide perovskites are attractive materials for ionizing radiation detection due to their high X-ray absorption, defect tolerance, and high charge carrier mobility. Current scintillator materials are expensive, typically grown as single crystals at high temperatures, whereas perovskites are solution processible at low temperatures, allowing for scalable, low-cost, large-area devices. We synthesize infrared-bandgap quantum-dot-doped perovskites that leverage exceptional optoelectronic properties of perovskites and bright emission of quantum dots for radiation detection. Complete attenuation of X-rays with energies up to 40 keV within 2 millimeters of material followed by efficient charge transfer to quantum dots for near-infrared emission was demonstrated. Scintillated light property dependence on quantum dot loading ranging from 0.01% to 1.0% was studied. A light yield of 37,400 ± 2,500 $phMeV^{-1}$ at room temperature was achieved, signaling usefulness of perovskite technology as cost-effective, scalable, efficient scintillators.

7.2 Introduction

Low-cost and efficient detectors for ionizing radiation, such as X-rays and gamma-rays, are desirable in the fields of X-ray diffraction,[1] X-ray imaging,[2] security,[3] high energy physics,[4] and others. Since the discovery of X-rays by Wilhelm Rontgen in 1895, X-ray detectors have evolved to center on two main designs: electronic-based semiconductors that directly convert photons to current and optical-based scintillators that down convert high energy photons to visible photons that are coupled to a sensitive photodetector.[5,6] Currently available scintillators, such as the benchmark CsI:TI (light yield of 60,000 $phMeV^{-1}$)[6,7] or the state-of-the-art $LuI_3:Ce^{3+}$ (light yield of 100,000 $phMeV^{-1}$),[8] are grown as single crystals using Czochralski or Bridgman processes to eliminate defects that induce charge carrier trapping and diminish light output, resulting in expensive products with limited application for large-area detectors.

Lead halide perovskites (LHPs) have desirable properties that are required for efficient ionizing radiation detection and material scalability that can overcome limitations of current technology. LHPs are composed of heavy atoms, such as lead, chlorine, bromine, and iodine, resulting in a high effective mass, Z_{eff}, that allows for strong interactions with high energy photons and excellent stopping power whereby photons with energies up to 1 MeV have a penetration depth of only ~1 centimeter.[9–12] LHPs are defect tolerant, exhibit charge carrier diffusion lengths of ~1 μm, and have long charge carrier lifetimes, resulting in remarkably efficient devices which have become revolutionary for many fields of optoelectronic-based devices.[13–17] LHPs also offer tunable optoelectronic properties based on material composition (e.g. Cl, Br, I) and the degree of quantum confinement of layered perovskite structures (i.e. n=1 up to n=∞ layers).[18,19] Moreover, LHPs are composed of cheap, abundant materials that are solution processible at low temperatures and can be fabricated as thin films, single crystals, and powders. The combination of these factors

makes LHPs a compelling class of materials for cost-effective and potentially efficient alternatives to current radiation detection technology.

Despite the advantages of LHPs, noteworthy radiation detection performances have so far been limited to LHPs in the forms of 0D quantum dots,[20–22] 2D perovskites,[9,23] and single crystals of 3D perovskites.[9,12,17,24] Reduced dimensionality in the 0D and 2D LHP structures provides quantum confinement of excitons, which increases exciton binding energies to more than 100 meV and reduces thermal quenching.[9,25] The theoretical maximum light yield of 2D LHPs exceeds 120,000 $phMeV^{-1}$, yet experimental light yields were reported to be 6,000 and 9,000 $phMeV^{-1}$ for $(C_6H_{13}NH_3)_2PbI_4$ and (EDBE)$PbCl_4$ ((EDBE = 2,20-ethylenedioxy)-bis(ethylamine)) at room temperature.[9] For 3D LHP systems, excitons have low binding energies less than 15 meV[26] and quickly dissociate into free carriers at room temperature, reducing radiative recombination and resulting in light yields below 1,000 $phMeV^{-1}$ at room temperature.[9,24] While light yields exceeding 100,000 $phMeV^{-1}$ with sub-nano second decay times have been achieved for methylammonium lead bromide ($MAPbBr_3$), cryogenic conditions at 10 K were required.[27] 3D LHPs, such as $MAPbBr_3$, also suffer from small Stokes shifts between absorption onset and emission, resulting in a partial re-absorption of emitted photons, which substantially reduces light emission and alters optical properties.[28,29] Due to low thicknesses, thin film and nanocrystalline LHP-based devices exhibit limited responsivity due to incomplete attenuation of high energy photons.[17,30] To increase the probability of photon-material interactions, researchers have resorted to growing large single crystals on the order of millimeters or centimeters in size to ensure that material thickness is greater than photon absorption lengths, further pushing the field to rely on single crystals similar to already commercialized products.[9,17,31]

To overcome limitations of single-phase LHP scintillators, we embedded 3.8 nm lead sulfide (PbS) quantum dots (QDs) in $MAPbBr_3$ to exploit complementary properties of each material: the defect tolerance, high stopping power, and long charge carrier diffusion lengths of LHPs and the quantum confinement, high radiative efficiency, lower bandgap, and tunable near-infrared (NIR) emission wavelength of quantum dots. Previously, Ning et al. synthesized thin films with heteroepitaxial alignment of PbS QDs embedded in $MAPbI_3$ thin films with atom-scale crystalline coherence and demonstrated remarkable charge transfer from perovskite to QDs.[32] Here, we embedded PbS QDs in a $MAPbBr_3$ matrix, a 3D LHP that is more stable under ambient conditions,[33] at very low loading amounts of 0.01% to 1.0% by mass. Rather than using a thin film geometry, we utilize a rapid, scalable powder fabrication method that provides sample sizes capable of capturing larger fractions of ionizing radiation. Light yield is inversely related to optical bandgap energy; by selecting a perovskite matrix with a lower energy bandgap of 2.2 eV, the theoretical light yield is up to 190,000 $phMeV^{-1}$, much higher than materials with wide bandgaps between 4 and 6 eV.[6,9] We show that optical properties of each species are retained and efficient charge transfer from LHP to QDs occurs even at very low QD loadings. We demonstrate the dependence of scintillation light output on QD loading, with a maximum light output at 0.05% QD loading with a light yield of 37,400 $phMeV^{-1}$ at room temperature. Lastly, we show proof of concept that emission wavelength can be varied from 1100 nm to 1350 nm by embedding different sized QDs and varying the QD loading, highlighting the potential to tune emission wavelength to match spectral response of detectors. Our work provides an advancement toward the commercialization of lead halide perovskite technology as cost-effective, efficient, and tunable scintillators with light yields rivaling that of commercial scintillators under room temperature operating conditions.

7.3 Results and Discussion

7.3.1 Scintillator functionality of QD-doped $MAPbBr_3$

The scintillation functionality of QD-doped $MAPbBr_3$ is shown in **Fig. 7.1a**. 3D LHP is the main component by mass, and the majority of incoming X-rays are absorbed by the perovskite matrix. As the primary hot electron dissipates energy to surrounding electrons, the secondary excited electrons relax to energies near the LHP conduction band edge. Because the PbS QDs have type I band alignment with respect to $MAPbBr_3$, electrons and holes are funneled to QDs, which act as emission centers for scintillated photons. The composite QD-doped LHP scintillator material exhibits a large Stokes shift between the strong perovskite absorption onset in the visible region and the emission of the QDs in the NIR region (**Fig. 7.1b**), preventing the self-absorption of scintillated photons by the perovskite matrix. With small doping amounts of less than 1%, reabsorption of NIR photons by other QDs is minimized.

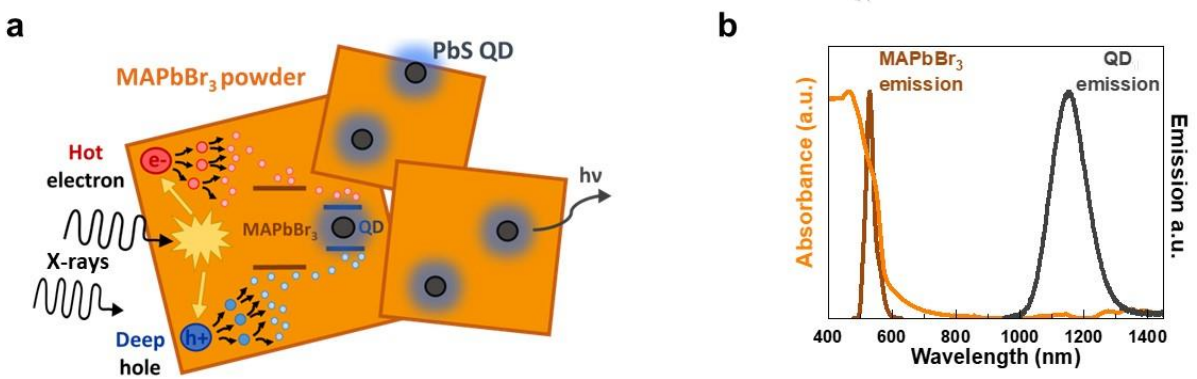

Figure 7.1. Schematic of QD-doped $MAPbBr_3$ scintillation process **a)** Depiction of the functionality of QD-doped $MAPbBr_3$ upon absorption of X-rays. A cascade of charge carriers is generated by the ionizing radiation and charge carriers are subsequently funneled into QDs for NIR emission. **b)** A large Stokes shift between perovskite absorbance and QD emission prevents reabsorption of scintillated NIR photons by the perovskite matrix, as shown by the absorbance of $MAPbBr_3$ and the emission of $MAPbBr_3$ and PbS QDs.

7.3.2 Fabrication of QD-doped $MAPbBr_3$ powder using anti-solvent crystallization

QD-doped LHP scintillators were fabricated using a bilayer solution ligand exchange to form a single solution containing both the QDs and LHP precursor components. Scintillator powders were subsequently crystallized upon injection into anti-solvent (**Fig. 7.2**, details in Materials and Methods). In previously published procedures, the QD ligand exchange is typically performed using a bilayer solution of N-dimethylformamide (DMF) or N-methylformamide (NMF) and hexane or octane.[34–37] We found that using NMF, which has significantly higher polarity, for the single solution of LHP precursors and QDs after ligand exchange to be essential for reproducibility. The NMF/octane bilayer solution method provided consistently functional scintillators with emission full width at half maximum (FWHM) rivaling that of oleate-capped

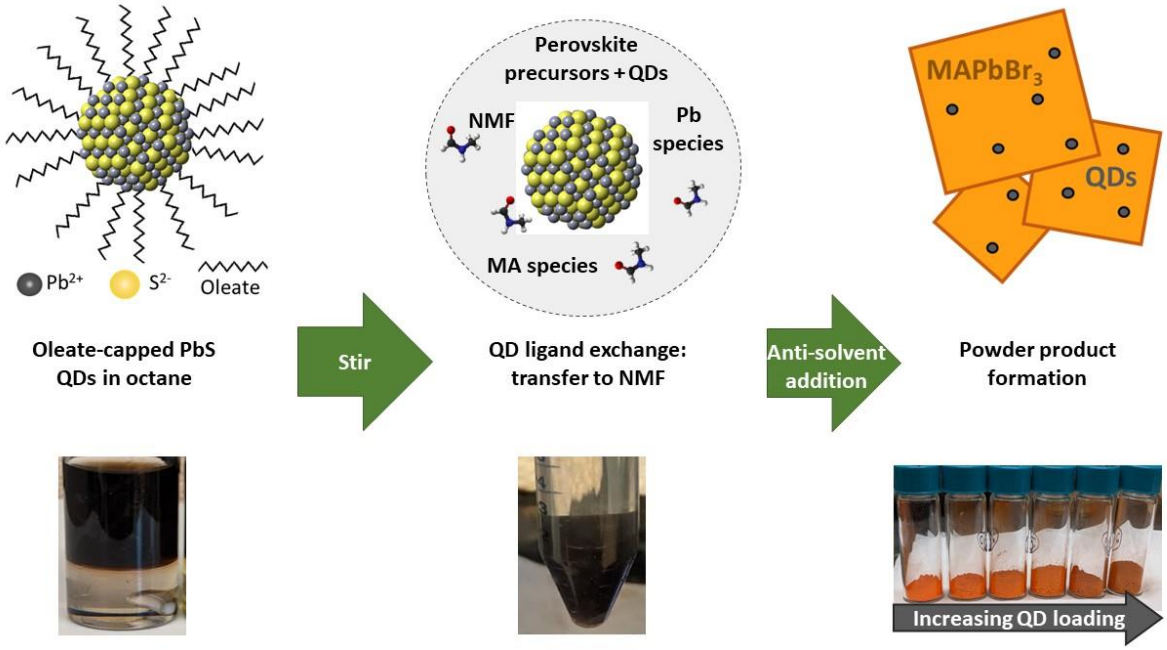

Figure 7.2. Processing diagram for QD-doped $MAPbBr_3$ scintillator powders. QDs undergo a ligand exchange using a bilayer solution of polar and nonpolar solvents. QDs transfer to polar phase to yield one solution containing QDs and perovskite precursors. Powders are formed rapidly via anti-solvent crystallization.

QDs whereas DMF/octane layering resulted in broadened emission peaks and irreproducible scintillator performances.

7.3.3 Crystal structure and morphology of QD-doped $MAPbBr_3$ powder

Scanning electron microscopy (SEM) was employed to characterize the particle size and morphology of the QD-doped LHP powders. Particle sizes were observed to be 500 μm (**Fig. 7.3a-b**), with these large particles being comprised of smaller particles less than 5 μm in size with a cubic morphology, reflecting the cubic atomic structure of $MAPbBr_3$ (**Fig. 7.3c-h**). Particle size generally decreased with increasing QD loading, which indicates increased nucleation rate possibly due to heterogeneous nucleation on the surfaces of the quantum dots in solution.

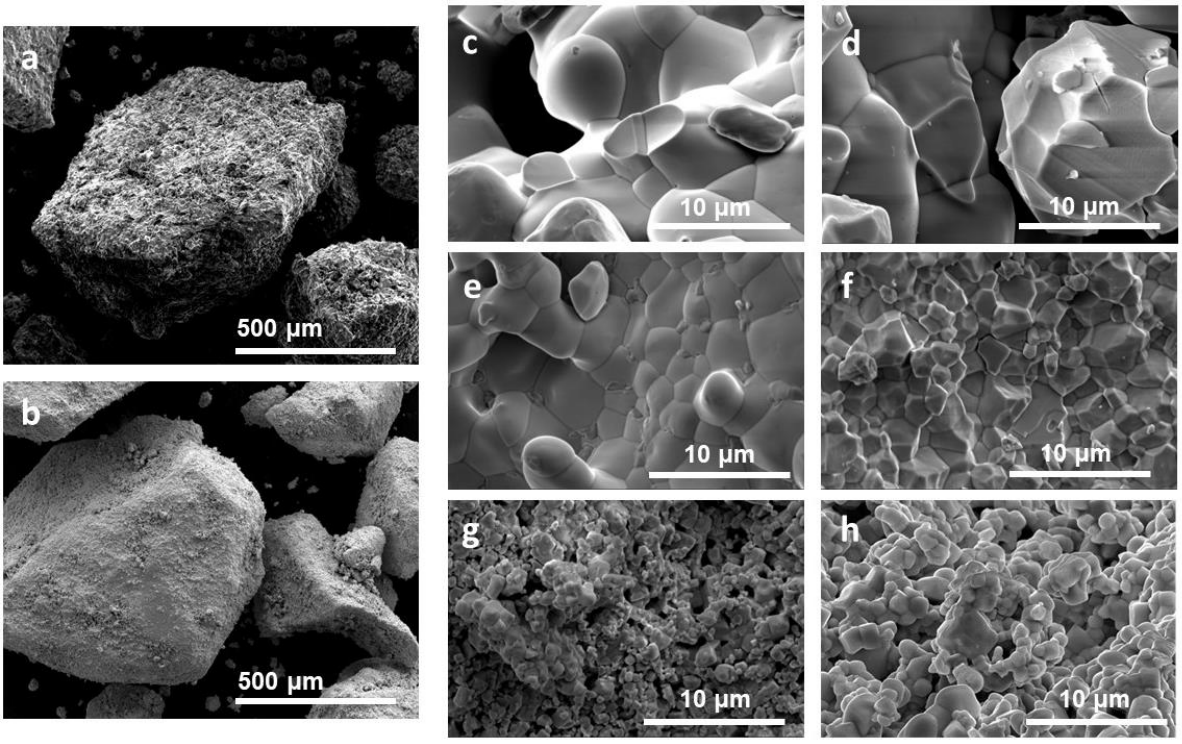

Figure 7.3. Scanning electron microscope (SEM) images of scintillator particle size and morphology. **a**) Particles of $MAPbBr_3$ without QDs and **b**) with 1.0 % QD loading. Morphology of particles with **c**) with no QDs, **d**) 0.01%, **e**) 0.05%, **f**) 0.1%, **g**) 0.5%, and **h**) 1.0% PbS quantum dot loading.

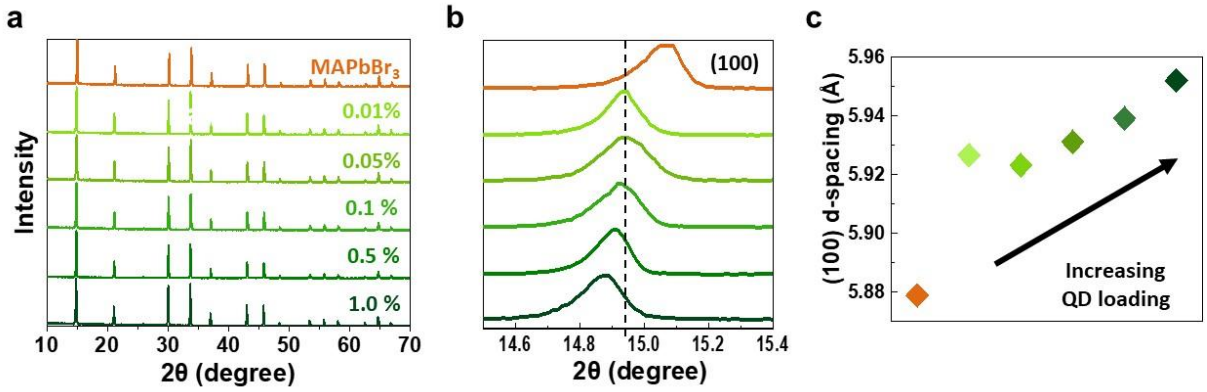

Figure 7.4. Structural analysis of QD-doped $MAPbBr_3$. **a)** Powder X-ray diffraction of scintillator powders with varying QD loadings. **b)** Peak shift of the (100) plane of $MAPbBr_3$ upon the incorporation of QDs. **c)** The d-spacing of the $MAPbBr_3$ (100) crystallographic plane.

Crystal structures of the powders were characterized using powder X-ray diffraction. All compositions of QD-doped LHP powders were highly-crystalline with the $pm\bar{3}m$ space group cubic structure of $MAPbBr_3$[38] (**Fig. 7.4a**). Diffraction peaks of PbS QDs were not observable in the composite powder samples, likely due to very low QD loading amounts by mass. Upon the inclusion of QDs into the $MAPbBr_3$ matrix, the (100) peak of $MAPbBr_3$ shifted to lower angles, indicating that a gradual expansion of the perovskite lattice occurred as the QD loading was increased (**Fig. 7.4b-c**). The Pb-Pb distance for PbS is ~5.97 Å,[32] and thus the expansion of the $MAPbBr_3$ lattice is indicative of strain induced by QD incorporation and lattice matching at the QD-perovskite interface. Our experimental results are consistent with studies that show that the perovskite lattice is more likely to accommodate strain than the more rigid PbS lattice.[32,39] With 1.0% QD loading, the $MAPbBr_3$ lattice sustains 1.2% strain, and the lowest strain from pure $MAPbBr_3$ lattice was observed for the lowest QD loading of 0.01% by mass with 0.8% strain.

7.3.4 Optical properties of quantum dot-perovskite composite powder

The absorption spectra of pure $MAPbBr_3$, as-prepared oleate-capped QDs, and QD-doped $MAPbBr_3$ powders were collected using a spectrophotometer equipped with an integrating sphere (**Fig. 7.5a**) The oleate-capped QD absorption peak was observed at 1039 nm, characteristic of 3.8 nm diameter PbS QDs. For the composite material, characteristic absorption signatures were observed for QDs and $MAPbBr_3$ in the NIR and visible regions, respectively. The QD absorption

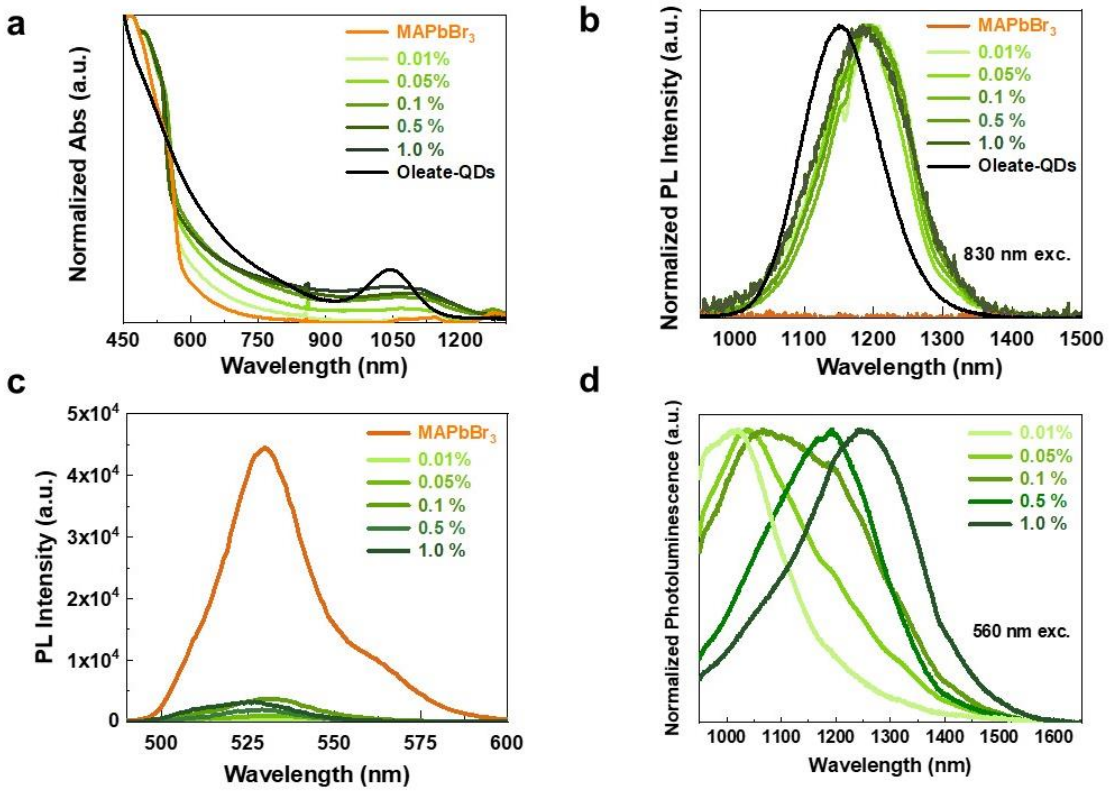

Figure 7.5. Optical properties of QD-doped $MAPbBr_3$. **a)** Normalized absorbance of scintillator powder shows perovskite strong absorption in the visible region and QD absorbance peak in the NIR region. **b)** Normalized photoluminescence of oleate-capped QDs and QDs embedded in $MAPbBr_3$. Excitation light with wavelength 830 nm was used to selectively excite QDs only. **c)** Photoluminescence of $MAPbBr_3$ with and without QDs shows that perovskite emission is quenched with incorporation of QDs. **d)** Photoluminescence of QDs embedded in $MAPbBr_3$ upon excitation of the perovskite matrix with 560 nm excitation light.

was observed for QD loadings of 0.05% and higher only, showing increasing absorbance correlated with increasing QD loadings.

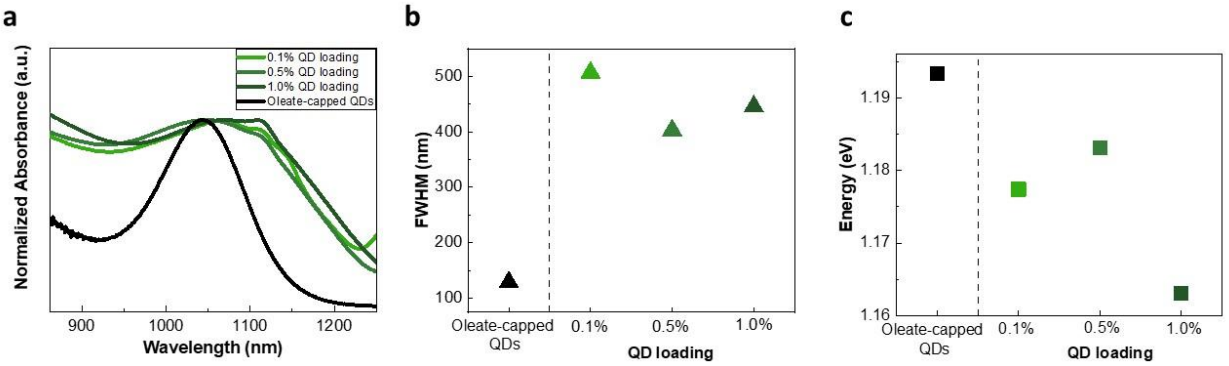

Figure 7.6. Absorbance peak analysis of QD-doped $MAPbBr_3$ powders compared to preformed oleate-capped PbS QDs before being embedded in perovskite matrix. **a)** Normalized absorbance peak of oleate-capped PbS QDs and highest QD loaded samples with observable peaks. **b)** Full width half maximum of absorbance peaks. **c)** Energy of PbS QD absorbance peaks with varying QD loading in perovskite matrix.

Upon incorporation in the perovskite matrix, the QD absorption peak underwent a redshift by 14 nm, 9 nm, and 26 nm for 0.1%, 0.5% and 1.0% QD loadings, respectively, relative to the oleate-capped QDs and the QD absorption peak was also significantly broadened once embedded in the $MAPbBr_3$ matrix (**Fig. 7.6a**), which is consistent with halide ligand exchange on the QD surface.[36,40,41] Upon selective excitation of the QDs with 830 nm light, whereby an exciton is generated within the QD, the QD emission peak was retained in the NIR region after incorporation in the perovskite matrix at all loadings (**Fig. 7.5b**), exhibiting a bandgap of 1.08 eV. The QD emission peak underwent a 0.04 eV redshift from 1153 nm for the oleate-capped QDs to ~1190 nm for QDs in the perovskite matrix but retained a FWHM of ~140 nm, indicating that the QD

photophysical properties based on QD size was retained. Both the absorbance and emission of QDs were slightly redshifted, which is consistent for QDs with a lead halide ligand exchange as well as the higher dielectric constant environment of the perovskite matrix.[35,42,43] The photoluminescence emission spectra of the QD-doped $MAPbBr_3$ and pure $MAPbBr_3$ are shown in **Fig. 7.5c**. The photoluminescence intensity of the $MAPbBr_3$ matrix was drastically quenched for QD-doped samples for all QD loading amounts, even at a low QD loading of 0.01%, indicating efficient charge carrier transfer from the perovskite matrix to QDs and is consistent with previous reports for QD-perovskite systems.[32,44]

To study QD emission with charge transfer from perovskite to QD, the perovskite matrix was excited with 560 nm light at the absorption edge of $MAPbBr_3$ (**Fig. 7.5d**). Because the valence band (VB) maximum and conduction band (CB) minimum of PbS QDs are within the bandgap of $MAPbBr_3$, we expected a single emission from QDs at ~1190 nm, similar to that observed when selectively exciting QDs with 830 nm light. However, QD emission was substantially blueshifted by nearly 200 nm at 0.01% and 0.05% QD loadings and redshifted by 50 nm at 1.0% QD loading.

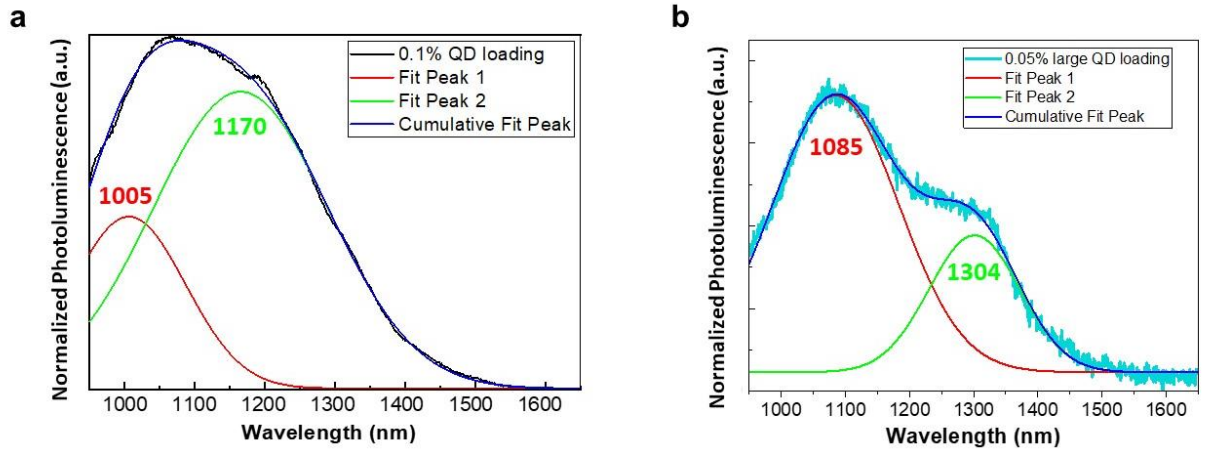

Figure 7.7. Deconvolution of two emission peaks observed when exciting QD-doped $MAPbBr_3$ with 560 nm light, which excites both the perovskite matrix and QDs. Multipeak emission of $MAPbBr_3$ doped with **a**) 3.8 nm and **b**) 4.3 nm QDs.

A double peak was observed at 0.1% QD loading, which appears to be a convolution of a new blueshifted peak at ~1005 nm and a peak at ~1170 nm corresponding to expected QD emission (**Fig. 7.7a**). All QD emission peaks following charge transfer were broadened relative to emission for selectively excited QDs using 830 nm light.

There is a ~0.2 eV energy difference between the two emission signatures observed at ~1005 nm and ~1200 nm. Exciplex state emission has been reported in perovskite-QD systems arising from synergistic effects between the two materials whereby electrons from the perovskite CB radiatively recombine with holes in the QD VB, resulting in a new broad emission peak.[46] Because this new emission peak is only observed for perovskite matrix excitation, our observations suggest that exciplex emission at the QD-perovskite interface via radiative recombination may be occurring between electrons in the QD CB and holes in the perovskite VB. Consistent with the study, the new emission peak shifts when changing QDs size. The new emission peak red shifts along with the expected QD emission peak when increasing QD size (**Fig. 7.7b**), which narrows the QD bandgap and reduces energy differences between QD and perovskite VB and CB band alignments. While previous reports of QD-perovskite composite materials have shown a single emission peak corresponding to radiative recombination in the VB and CB of the QDs following charge transfer, this was observed for systems with QD loadings much greater than 1% (i.e., 11% to 28%).[32, 45] In this study, the new emission peak is only observed for QD loadings of 0.01%, 0.05%, and 0.1%. At QD loadings 0.5% and greater, this feature is no longer observed; emission of the composite material matches that of QD emission based on QD size with minor red-shifts when further increasing QD loading and aligns with previous reports. At very low QD loadings, it is possible that small QD populations may be overwhelmed with carriers produced in the perovskite matrix and intensifies this inter-band emission. However, a thorough study would be

required to confirm exciplex emission and identify underlying mechanisms. While the appearance of this feature poses interesting research questions, it does not impact scintillator functionality and is thus outside the scope of this study.

7.3.5 Effect of varying QD loading on scintillation light yield

The radioluminescence of QD-doped perovskite scintillators was measured using a table-top imaging X-ray source that provides a continuum of X-ray energies up to 40 keV. A comparison of the normalized spectra of photoluminescence of oleate-capped QDs, photoluminescence of QD-doped $MAPbBr_3$, and radioluminescence of QD-doped MAPbBr3 with varying QD loadings are overlayed in **Fig. 7.8**. Spectral matching between photoluminescence and radioluminescence indicates that characteristic QD emission wavelength is maintained under ionizing radiation

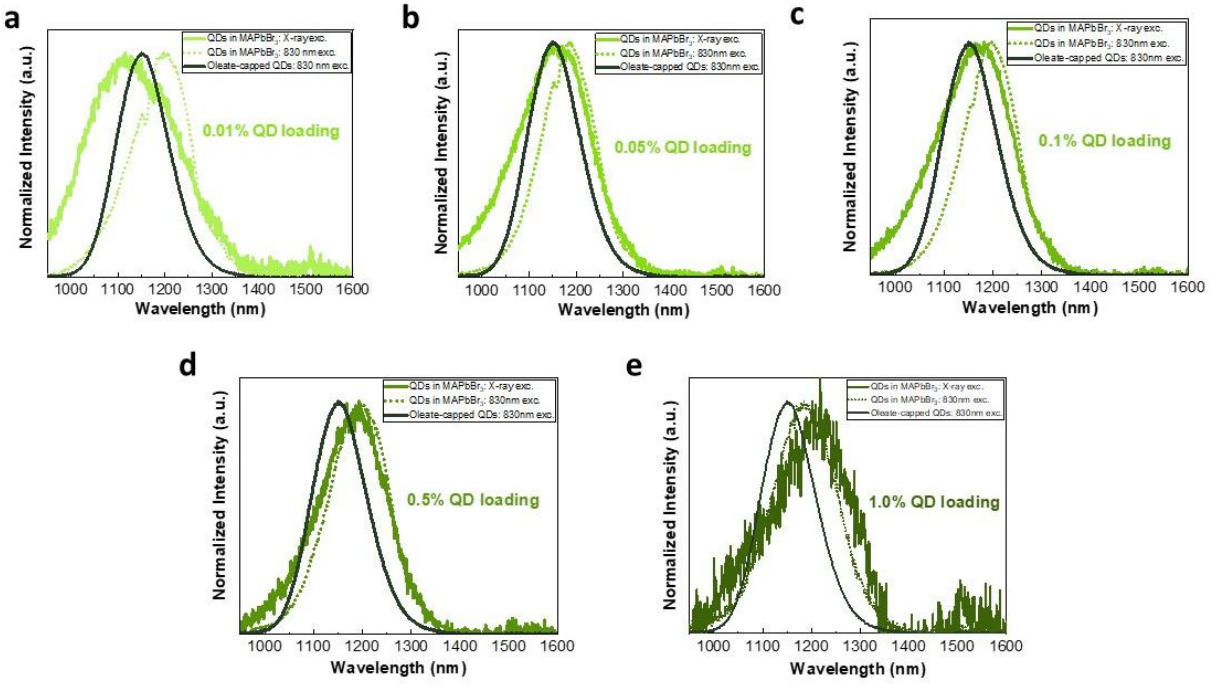

Figure 7.8. Comparison of the spectral overlap of oleate-capped QD photoluminescence with the photoluminescence of selectively excited QDs in $MAPbBr_3$ and radioluminescence with **a)** 0.01%, **b)** 0.05%, **c)** 0.1%, **d)** 0.5%, and **e)** 1.0% QD loading by mass.

exposure. Radioluminescence emission peaks of QD-doped $MAPbBr_3$ gradually redshifted with increasing QD loading from 1129 nm (0.01% loading) to 1199 nm (1.0% loading) (**Fig. 7.9a**). Because the perovskite matrix absorbs the vast majority of the X-rays, the strong NIR emission provides a second indication of energy transfer from the perovskite matrix to the quantum dots. Radioluminescence of $MAPbBr_3$ with 0.01% QD loading exhibited a broadened emission peak with a higher FWHM (264 nm) relative to the other samples (156-197 nm) (**Fig. 7.9b**). The energy differences between the radioluminescence and photoluminescence emission peak (X-ray and 830 nm excitation, respectively) decreased with increasing QD doping (**Fig. 7.9c**). Samples with lower QD loadings showed a blueshift in emission under X-ray illumination (0.01%, 0.05%, 0.1%) while the sample with highest loading (1.0%) exhibited a red-shift in emission. Total attenuation of X-rays was achieved with two millimeters of QD-doped perovskite powder (Figure S15), and thus we show that QD-doped perovskite scintillators exploit the excellent stopping power of LHPs in addition to the narrow band emission of the quantum dots.

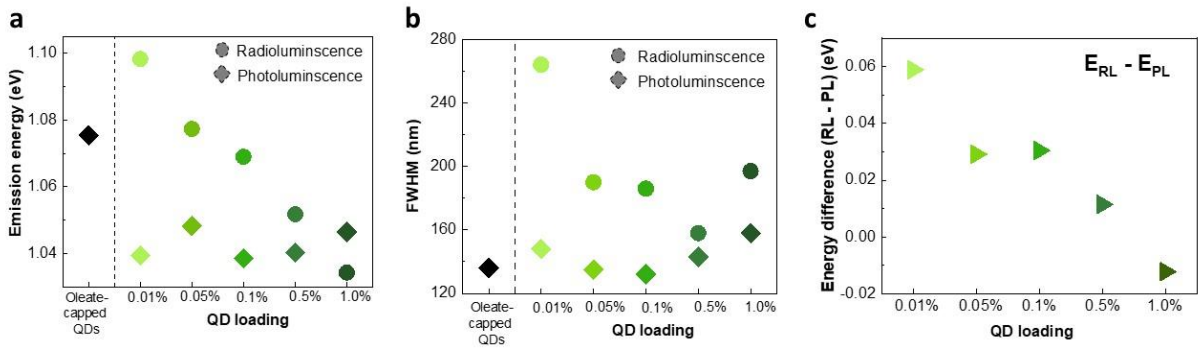

Figure 7.9. a) Energies of the radioluminescence and photoluminescence emission peaks for QD-doped $MAPbBr_3$ powders with varying QD loading as compared to the photoluminescence of as-prepared oleate-capped PbS QDs. **b)** Full width half maximum (FWHM) analysis of radioluminescence and photoluminescence emission peaks. **c)** Energy differences between radioluminescence under X-ray illumination and photoluminescence with selectively excited QDs with 830 nm excitation light.

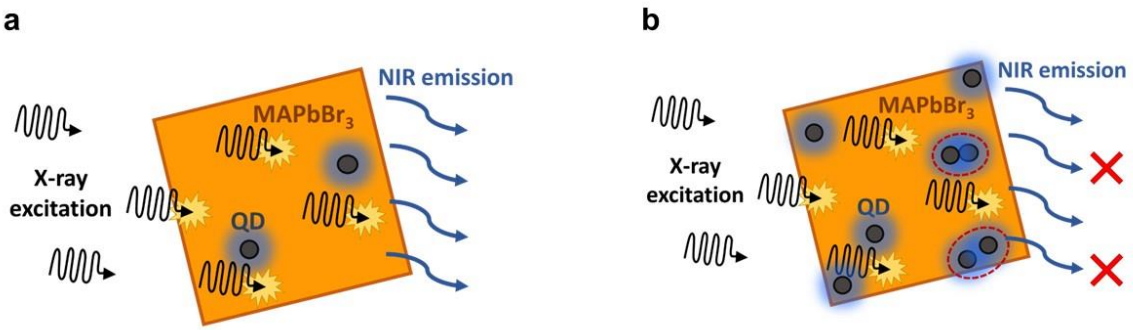

Figure 7.10. Depiction of QD emission at high and low loadings. **a)** Lower QD loading reduces the number of emission sites. **b)** Higher QD loading increases probability of QD-QD interactions which can quench QD emission.

As shown in **Fig. 7.10**, varying the QD loading alters the number of emission sites available to charge carriers; lower QD loading increases interdot distances, i.e. the average distance charge carriers need to travel to reach a quantum dot emission site, but simultaneously reduces the probability of interdot interactions that quench QD emission.[47,48] Due to the competing effects of the number of emission sites and interdot interactions, we hypothesized that there exists an optimal QD loading that maximizes scintillated photon output. With increasing QD loading, radioluminescence emission red-shifts to longer wavelength (**Fig. 7.11a**). Radioluminescence intensities of QD-doped perovskite scintillators with various QD loading amounts are shown in **Fig. 7.11b**. Increasing the QD loading from 0.01% to 0.05% resulted in an increase in radioluminescence intensity. Further increasing the QD loading from 0.05% to 0.1% resulted in a slight decrease in radioluminescence followed by a substantial reduction in radioluminescence at 0.5% and 1.0% QD loadings.

To quantify the light yields of QD-doped $MAPbBr_3$, we utilized a method using commercial scintillators with known light yields to calculate energy deposited values and power meters to quantify scintillated light output for visible and NIR scintillators; details of our procedure

can be found in Chapter 5. As shown in **Fig.7.11c**, a light yield of 37,400 ± 2,500 phMeV^{-1} was achieved for the best performing scintillator composition with 0.05% QD loading, and the lowest light yield was 5,800 ± 400 phMeV^{-1} for 1.0% QD loading. We note that all measurements were conducted at room temperature, and all scintillators were polycrystalline powder samples. Our results mark a significant improvement over currently reported perovskite scintillators that require low temperature operating conditions and are limited to expensive nanostructured materials.

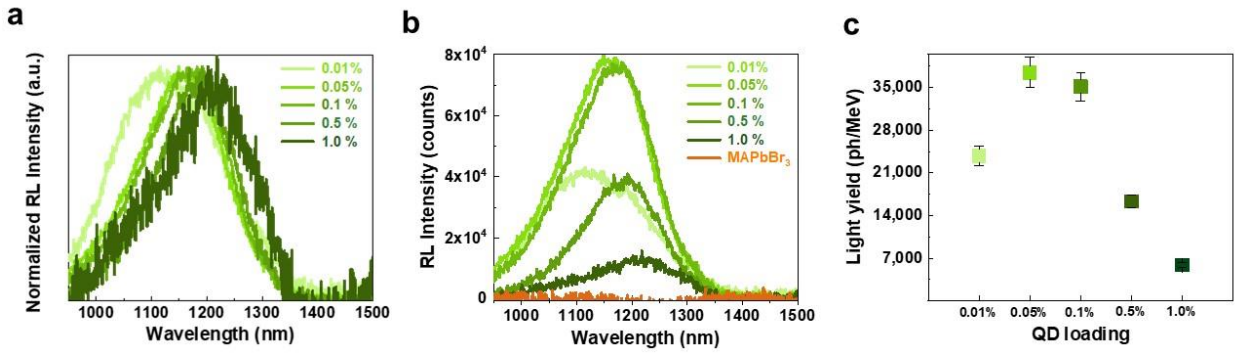

Figure 7.11. Radioluminescence and light yields of QD-doped $MAPbBr_3$ scintillators under X-ray excitation. **a)** Normalized radioluminescence shows a gradual redshift in the emission peak with increasing QD loading. **b)** Radioluminescence and **c)** light yields of scintillator powders with varying QD loading showing a maximum signal and light yield for 0.05% QD loading in $MAPbBr_3$.

7.3.6 Effect of varying quantum dot size and loading on radioluminescence

To explore the tunability of QD-doped $MAPbBr_3$ scintillators, we embedded a smaller (3.2 nm) and larger (4.3 nm) PbS QD into $MAPbBr_3$. Changing QD size alters the degree of quantum confinement which affects QD bandgap energy and emission wavelength (**Fig. 7.12a**). Varying QD size and loading resulted in a range of radioluminescence emission from 1100 nm to 1350 nm (**Fig. 7.12b**). QD size had the most prominent effect on QD-doped perovskite scintillation emission wavelength. Due to significantly blueshifted emission at low QD loading and redshifted emission at higher QD loading, a 50 nm shift in emission wavelength was observed when increasing QD loading from 0.05% to 1.0% loading for both 3.8 nm QDs and 4.3 nm QDs. A maximum radioluminescence signal was observed with 0.05% loading of the larger QD, the lowest loading explored for this QD size, corresponding to a light yield of 17,000 ± 1,200 $phMeV^{-1}$ (**Fig. 7.12c**). Consistent with the results based on 3.8 nm PbS QDs, increasing the 4.3 nm QD loading above 0.05% resulted in a decrease in radioluminescence.

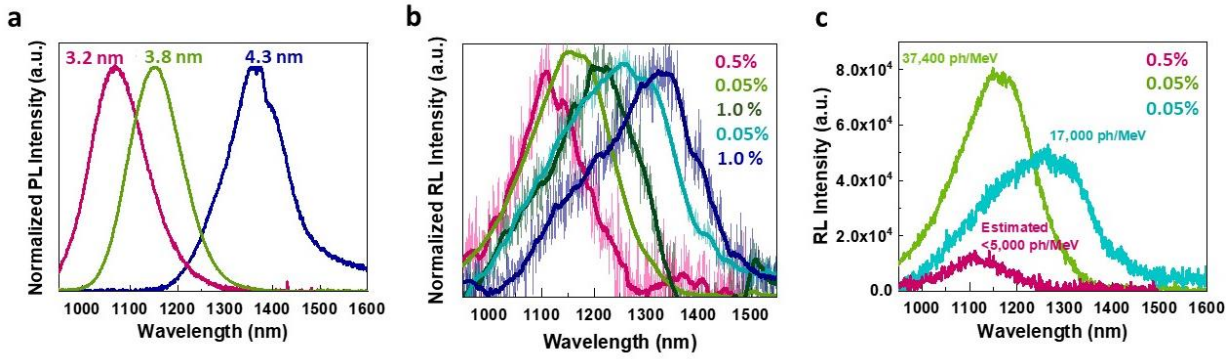

Figure 7.12. a) Photoluminescence of as-prepared oleate-capped PbS QDs with varying sizes. **b)** Range of radioluminescence emission of QD-doped $MAPbBr_3$ with varying QD size and doping amounts. **c)** Radioluminescence signals and corresponding light yields of best performing scintillators with optimal loadings using 3.2 nm, 3.8 nm, and 4.3 nm PbS QDs.

7.4 Conclusion

Lead sulfide quantum dots were embedded in $MAPbBr_3$ lead halide perovskite using solution-based crystallization methods to form polycrystalline scintillator powders for X-ray detection. Structural analysis indicated expansion of the $MAPbBr_3$ lattice when incorporating PbS quantum dots due to strain induced by lattice matching at the QD-perovskite interface. By combining photophysical aspects of quantum dots and lead halide perovskites, we establish that these composite heterocrystalline scintillators exhibit high X-ray absorption within the perovskite matrix for charge carrier generation using only a few millimeters of material followed by efficient charge transfer to quantum dots for NIR emission. Optical properties of perovskite and quantum dot components were preserved in the composite scintillators. A maximum light yield of 37,400 ± 2,500 $phMeV^{-1}$ was demonstrated at room temperature for $MAPbBr_3$ doped with 0.05% PbS quantum dots by mass. This work highlights the advantages of designing doped perovskite-based composite scintillators that exploit properties of different optoelectronic materials. The tunability of quantum dot emission could allow for spectral matching tailored to specific detectors, such as further reducing QD size to achieve emission at visible wavelengths where it can be paired with commonly used silicon detectors. With tunable optical properties in combination with solution processability, quantum-dot-doped lead halide perovskites could be promising for scalable, low-cost, large-area next generation ionizing radiation detectors with room temperature applications.

7.5 Materials and Methods

7.5.1 Synthesis of oleate-capped PbS QDs

Lead(II) oxide (3 mmol, 99.999%, Alfa Aesar), 15–60 mmol of oleic acid (90%, Sigma Aldrich), and 1-octadecene (90%, Alfa Aesar) were added to make a 30 mL total volume solution in a three-neck flask. To synthesize different sizes of QDs (3.2–4.3 nm in diameter), the molar ratio between PbO and HOA was varied from 5:1 to 20:1 and the temperature of $(TMS)_2S$ injection was varied from 90–120 °C. The solution was stirred in the flask for 1 hour under vacuum at 130 °C until the lead oxide was dissolved. Under Argon gas flow, the temperature was adjusted to 90–120 °C in preparation for injection. In an N_2-filled glovebox, 0.1 M of hexamethyldisilathiane ($(TMS)_2S$) solution was prepared by mixing 378 μL of $(TMS)_2S$ in 18 mL of 1-octadecene (ODE). 15 mL of 0.1 M $(TMS)_2S$ solution was taken out of the glovebox and quickly injected into the three-neck flask. After 60-70 s, the reaction flask was submerged in an ice bath to quickly quench the temperature of the reaction solution. During the purification process, unreacted species were removed by a series of centrifuge steps after cleaning the product with methyl acetate and hexane. The final QD was stored in solid form under N_2 in a glovebox.

7.5.2 Synthesis of QD-doped $MAPbBr_3$ powder:

Lead bromide ($PbBr_2$, 99.999% trace metals basis), methylammonium bromide (MABr, ≥99%, anhydrous), N-methylformamide (NMF, 99%), isopropylalcohol (IPA, 99.5%, anhydrous) and octane (≥99%, anhydrous) were purchased from Sigma Aldrich. Synthesis was performed in a nitrogen filled glovebox in absence of water and oxygen. Perovskite precursor solutions with one molar concentrations in NMF with 1.1:1 ratio of MABr:$PbBr_2$ were prepared and allowed to stir until completely dissolved. Oleate-capped QDs were suspended in octane solution with a

concentration of 10 mg/mL. An aliquot of QD solution was added to the top of the perovskite precursor solution and fresh octane was added so that the vol:vol ratio of octane-to-NMF was 2:1. The bilayer solution was stirred for 21 hours to allow for ligand exchange and QD transfer from the nonpolar octane layer to the polar NMF layer with the perovskite precursors. The octane layer was removed and washed three times with fresh octane using the same 2:1 ratio of octane to NMF. The NMF solution containing quantum dots and perovskite precursors was injected into IPA at a vol:vol ratio of 10:1 for IPA:NMF and powder products formed immediately. The powder was washed three times with IPA and the powders were dried in a glovebox vacuum oven for two days.

7.5.3 Scintillator powder sample preparation

Kapton capillaries with an inner diameter of 0.0710" and outer diameter of 0.0750" were purchased from Cole-Parmer. A clay sealant was purchased from Thomas Scientific to plug the ends of the capillaries. Optically clear adhesive tape was purchased from Thor Labs. For scintillation measurements using X-ray excitation, photoluminescence using 830 nm light, and absorbance measurements, powders were packed into Kapton capillaries. For photoluminescence of lead halide perovskites and quantum dots using 560 nm light, powders were mounted to glass slides using optical tape.

7.5.4 Powder characterization

X-ray diffraction patterns were collected using an Empyrean Multipurpose X-ray Diffractometer equipped with a Cu anode using a step size of 0.015° with parameters set to 45 kV and 40 mA. Morphology of particles were determined using a FEI quanta 650 scanning electron microscope. Steady state photoluminescence measurements were conducted using a PTI QuantaMaster 400

spectrofluorometer equipped with two detectors, a R2658 Visible PMT detector and H10330-75 PMT NIR detector, and a Xe arc lamp excitation source (560 nm and 830 nm bandpass filters were used). Absorbance spectra were collected using a PerkinElmer UV/Vis/NIR Lambda 950S spectrometer with an integrating sphere.

7.6 Contributors

Joshua Choi and Heung-Sun Lee conceived the study. Ashley Conley developed and optimized the synthesis procedure, performed optical and structural measurements, performed and designed light yield methodology, and performed data analysis in this study. Ephraiem Sarabamoun performed morphological measurements. Ephraiem Sarabamoun and Lucy Yoon fabricated quantum dots. Katelyn. assisted in material development. Haritha Hajeev assisted in structural measurements.

7.6 References

(1) Tegze, M.; Faigel, G. X-Ray Holography with Atomic Resolution. *Nature* **1996**, *380* (6569), 49–51. https://doi.org/10.1038/380049a0.

(2) Kasap, S.; Frey, J. B.; Belev, G.; Tousignant, O.; Mani, H.; Greenspan, J.; Laperriere, L.; Bubon, O.; Reznik, A.; DeCrescenzo, G.; Karim, K. S.; Rowlands, J. A. Amorphous and Polycrystalline Photoconductors for Direct Conversion Flat Panel X-Ray Image Sensors. *Sensors (Basel)* **2011**, *11* (5), 5112–5157. https://doi.org/10.3390/s110505112.

(3) Vetter, K.; Barnowksi, R.; Haefner, A.; Joshi, T. H. Y.; Pavlovsky, R.; Quiter, B. J. Gamma-Ray Imaging for Nuclear Security and Safety: Towards 3-D Gamma-Ray Vision. *Nuclear Instruments and Methods in Physics Research Section A: Accelerators, Spectrometers, Detectors and Associated Equipment* **2018**, *878*, 159–168. https://doi.org/10.1016/j.nima.2017.08.040.

(4) Aharonian, F.; Buckley, J.; Kifune, T.; Sinnis, G. High Energy Astrophysics with Ground-Based Gamma Ray Detectors. *Reports on Progress in Physics* **2008**, *71* (9), 096901. https://doi.org/10.1088/0034-4885/71/9/096901.

(5) Szeles, C. CdZnTe and CdTe Materials for X-Ray and Gamma Ray Radiation Detector Applications. *physica status solidi (b)* **2004**, *241* (3), 783–790. https://doi.org/10.1002/pssb.200304296.

(6) Nikl, M. Scintillation Detectors for X-Rays. *Measurement Science and Technology* **2006**, *17* (4), R37–R54. https://doi.org/10.1088/0957-0233/17/4/r01.

(7) Epic Crystal. CsI(Tl) Scintillator. https://www.epic-crystal.com/halide-scintillators/csi-tl-scintillator.html.

(8) Birowosuto, M. D.; Dorenbos, P.; van Eijk, C. W. E.; Krämer, K. W.; Güdel, H. U. High-Light-Output Scintillator for Photodiode Readout: LuI3:Ce3+. *Journal of Applied Physics* **2006**, *99* (12), 123520. https://doi.org/10.1063/1.2207689.

(9) Birowosuto, M. D.; Cortecchia, D.; Drozdowski, W.; Brylew, K.; Lachmanski, W.; Bruno, A.; Soci, C. X-Ray Scintillation in Lead Halide Perovskite Crystals. *Scientific Reports* **2016**, *6* (1), 37254. https://doi.org/10.1038/srep37254.

(10) He, Y.; Hadar, I.; Kanatzidis, M. G. Detecting Ionizing Radiation Using Halide Perovskite Semiconductors Processed through Solution and Alternative Methods. *Nature Photonics* **2022**, *16* (1), 14–26. https://doi.org/10.1038/s41566-021-00909-5.

(11) Wei, H.; Huang, J. Halide Lead Perovskites for Ionizing Radiation Detection. *Nature Communications* **2019**, *10* (1), 1066. https://doi.org/10.1038/s41467-019-08981-w.

(12) Yakunin, S.; Sytnyk, M.; Kriegner, D.; Shrestha, S.; Richter, M.; Matt, G. J.; Azimi, H.; Brabec, C. J.; Stangl, J.; Kovalenko, M. V.; Heiss, W. Detection of X-Ray Photons by Solution-Processed Lead Halide Perovskites. *Nature Photonics* **2015**, *9* (7), 444–449. https://doi.org/10.1038/nphoton.2015.82.

(13) Stranks Samuel D.; Eperon Giles E.; Grancini Giulia; Menelaou Christopher; Alcocer Marcelo J. P.; Leijtens Tomas; Herz Laura M.; Petrozza Annamaria; Snaith Henry J. Electron-Hole Diffusion Lengths Exceeding 1 Micrometer in an Organometal Trihalide Perovskite Absorber. *Science* **2013**, *342* (6156), 341–344. https://doi.org/10.1126/science.1243982.

(14) Lee, M. M.; Teuscher, J.; Miyasaka, T.; Murakami, T. N.; Snaith, H. J. Efficient Hybrid Solar Cells Based on Meso-Superstructured Organometal Halide Perovskites. *Science* **2012**, *338* (6107), 643. https://doi.org/10.1126/science.1228604.

(15) Burschka, J.; Pellet, N.; Moon, S.-J.; Humphry-Baker, R.; Gao, P.; Nazeeruddin, M. K.; Grätzel, M. Sequential Deposition as a Route to High-Performance Perovskite-Sensitized Solar Cells. *Nature* **2013**, *499* (7458), 316–319. https://doi.org/10.1038/nature12340.

(16) Zhou Huanping; Chen Qi; Li Gang; Luo Song; Song Tze-bing; Duan Hsin-Sheng; Hong Ziruo; You Jingbi; Liu Yongsheng; Yang Yang. Interface Engineering of Highly Efficient Perovskite Solar Cells. *Science* **2014**, *345* (6196), 542–546. https://doi.org/10.1126/science.1254050.

(17) Wei, H.; Fang, Y.; Mulligan, P.; Chuirazzi, W.; Fang, H.-H.; Wang, C.; Ecker, B. R.; Gao, Y.; Loi, M. A.; Cao, L.; Huang, J. Sensitive X-Ray Detectors Made of Methylammonium Lead Tribromide Perovskite Single Crystals. *Nature Photonics* **2016**, *10* (5), 333–339. https://doi.org/10.1038/nphoton.2016.41.

(18) Chen, Y.; Sun, Y.; Peng, J.; Tang, J.; Zheng, K.; Liang, Z. 2D Ruddlesden–Popper Perovskites for Optoelectronics. *Advanced Materials* **2018**, *30* (2), 1703487. https://doi.org/10.1002/adma.201703487.

(19) Protesescu, L.; Yakunin, S.; Bodnarchuk, M. I.; Krieg, F.; Caputo, R.; Hendon, C. H.; Yang, R. X.; Walsh, A.; Kovalenko, M. V. Nanocrystals of Cesium Lead Halide Perovskites (CsPbX3, X = Cl, Br, and I): Novel Optoelectronic Materials Showing Bright Emission with Wide Color Gamut. *Nano Lett.* **2015**, *15* (6), 3692–3696. https://doi.org/10.1021/nl5048779.

(20) Xu, Q.; Huang, J.; Liu, J.; Wang, J.; Zhou, S.; Wang, X.; Nie, J.; Guo, Y.; OuYang, X. Lead Halide Perovskite Quantum Dots Based Liquid Scintillator for X-Ray Detection. *Nanotechnology* **2021**, *32*. https://doi.org/10.1088/1361-6528/abe48a.

(21) Chen, Q.; Wu, J.; Ou, X.; Huang, B.; Almutlaq, J.; Zhumekenov, A. A.; Guan, X.; Han, S.; Liang, L.; Yi, Z.; Li, J.; Xie, X.; Wang, Y.; Li, Y.; Fan, D.; Teh, D. B. L.; All, A. H.; Mohammed, O. F.; Bakr, O. M.; Wu, T.; Bettinelli, M.; Yang, H.; Huang, W.; Liu, X. All-Inorganic Perovskite Nanocrystal Scintillators. *Nature* **2018**, *561* (7721), 88–93. https://doi.org/10.1038/s41586-018-0451-1.

(22) Zhang, Y.; Sun, R.; Ou, X.; Fu, K.; Chen, Q.; Ding, Y.; Xu, L.-J.; Liu, L.; Han, Y.; Malko, A. V.; Liu, X.; Yang, H.; Bakr, O. M.; Liu, H.; Mohammed, O. F. Metal Halide Perovskite Nanosheet for X-Ray High-Resolution Scintillation Imaging Screens. *ACS Nano* **2019**, *13* (2), 2520–2525. https://doi.org/10.1021/acsnano.8b09484.

(23) Shibuya, K.; Koshimizu, M.; Takeoka, Y.; Asai, K. Scintillation Properties of (C6H13NH3)2PbI4: Exciton Luminescence of an Organic/Inorganic Multiple Quantum Well Structure Compound Induced by 2.0 MeV Protons. *Nuclear Instruments and Methods*

in Physics Research Section B: Beam Interactions with Materials and Atoms **2002**, *194* (2), 207–212. https://doi.org/10.1016/S0168-583X(02)00671-7.

(24) Kobayashi, M.; Omata, K.; Sugimoto, S.; Tamagawa, Y.; Kuroiwa, T.; Asada, H.; Takeuchi, H.; Kondo, S. Scintillation Characteristics of CsPbCl3 Single Crystals. *Nuclear Instruments and Methods in Physics Research Section A: Accelerators, Spectrometers, Detectors and Associated Equipment* **2008**, *592* (3), 369–373. https://doi.org/10.1016/j.nima.2008.04.079.

(25) Quan, L. N.; García de Arquer, F. P.; Sabatini, R. P.; Sargent, E. H. Perovskites for Light Emission. *Advanced Materials* **2018**, *30* (45), 1801996. https://doi.org/10.1002/adma.201801996.

(26) Miyata, A.; Mitioglu, A.; Plochocka, P.; Portugall, O.; Wang, J. T.-W.; Stranks, S. D.; Snaith, H. J.; Nicholas, R. J. Direct Measurement of the Exciton Binding Energy and Effective Masses for Charge Carriers in Organic–Inorganic Tri-Halide Perovskites. *Nature Physics* **2015**, *11* (7), 582–587. https://doi.org/10.1038/nphys3357.

(27) Mykhaylyk, V. B.; Kraus, H.; Saliba, M. Bright and Fast Scintillation of Organolead Perovskite MAPbBr3 at Low Temperatures. *Mater. Horiz.* **2019**, *6* (8), 1740–1747. https://doi.org/10.1039/C9MH00281B.

(28) Diab, H.; Arnold, C.; Lédée, F.; Trippé-Allard, G.; Delport, G.; Vilar, C.; Bretenaker, F.; Barjon, J.; Lauret, J.-S.; Deleporte, E.; Garrot, D. Impact of Reabsorption on the Emission Spectra and Recombination Dynamics of Hybrid Perovskite Single Crystals. *J. Phys. Chem. Lett.* **2017**, *8* (13), 2977–2983. https://doi.org/10.1021/acs.jpclett.7b00998.

(29) Schötz, K.; Askar, A. M.; Peng, W.; Seeberger, D.; Gujar, T. P.; Thelakkat, M.; Köhler, A.; Huettner, S.; Bakr, O. M.; Shankar, K.; Panzer, F. Double Peak Emission in Lead Halide Perovskites by Self-Absorption. *J. Mater. Chem. C* **2020**, *8* (7), 2289–2300. https://doi.org/10.1039/C9TC06251C.

(30) Turtos, R. M.; Gundacker, S.; Omelkov, S.; Auffray, E.; Lecoq, P. Light Yield of Scintillating Nanocrystals under X-Ray and Electron Excitation. *Journal of Luminescence* **2019**, *215*, 116613. https://doi.org/10.1016/j.jlumin.2019.116613.

(31) Selling, J.; Schweizer, S.; Birowosuto, M. D.; Dorenbos, P. Cerium-Doped Barium Halide Scintillators for x-Ray and γ-Ray Detections. *Journal of Applied Physics* **2007**, *102* (7), 074915. https://doi.org/10.1063/1.2786714.

(32) Ning, Z.; Gong, X.; Comin, R.; Walters, G.; Fan, F.; Voznyy, O.; Yassitepe, E.; Buin, A.; Hoogland, S.; Sargent, E. H. Quantum-Dot-in-Perovskite Solids. *Nature* **2015**, *523* (7560), 324–328. https://doi.org/10.1038/nature14563.

(33) McGovern, L.; Futscher, M. H.; Muscarella, L. A.; Ehrler, B. Understanding the Stability of MAPbBr3 versus MAPbI3: Suppression of Methylammonium Migration and Reduction of Halide Migration. *J. Phys. Chem. Lett.* **2020**, *11* (17), 7127–7132. https://doi.org/10.1021/acs.jpclett.0c01822.

(34) Crisp, R. W.; Kroupa, D. M.; Marshall, A. R.; Miller, E. M.; Zhang, J.; Beard, M. C.; Luther, J. M. Metal Halide Solid-State Surface Treatment for High Efficiency PbS and PbSe QD Solar Cells. *Scientific Reports* **2015**, *5* (1), 9945. https://doi.org/10.1038/srep09945.

(35) Zhang, X.; Zhang, J.; Phuyal, D.; Du, J.; Tian, L.; Öberg, V. A.; Johansson, M. B.; Cappel, U. B.; Karis, O.; Liu, J.; Rensmo, H.; Boschloo, G.; Johansson, E. M. J. Inorganic CsPbI3 Perovskite Coating on PbS Quantum Dot for Highly Efficient and Stable Infrared Light Converting Solar Cells. *Advanced Energy Materials* **2018**, *8* (6), 1702049. https://doi.org/10.1002/aenm.201702049.

(36) Qiao, K.; Cao, Y.; Yang, X.; Khan, J.; Deng, H.; Zhang, J.; Farooq, U.; Yuan, S.; Song, H. Efficient Interface and Bulk Passivation of PbS Quantum Dot Infrared Photodetectors by PbI2 Incorporation. *RSC Adv.* **2017**, *7* (83), 52947–52954. https://doi.org/10.1039/C7RA10422G.

(37) Yang, Z.; Fan, J. Z.; Proppe, A. H.; Arquer, F. P. G. de; Rossouw, D.; Voznyy, O.; Lan, X.; Liu, M.; Walters, G.; Quintero-Bermudez, R.; Sun, B.; Hoogland, S.; Botton, G. A.; Kelley, S. O.; Sargent, E. H. Mixed-Quantum-Dot Solar Cells. *Nature Communications* **2017**, *8* (1), 1325. https://doi.org/10.1038/s41467-017-01362-1.

(38) Wang, K.-H.; Li, L.-C.; Shellaiah, M.; Sun, K. W. Structural and Photophysical Properties of Methylammonium Lead Tribromide (MAPbBr3) Single Crystals. *Scientific Reports* **2017**, *7*. https://doi.org/10.1038/s41598-017-13571-1.

(39) Sánchez-Godoy, H. E.; Erazo, E. A.; Gualdrón-Reyes, A. F.; Khan, A. H.; Agouram, S.; Barea, E. M.; Rodriguez, R. A.; Zarazúa, I.; Ortiz, P.; Cortés, M. T.; Muñoz-Sanjosé, V.; Moreels, I.; Masi, S.; Mora-Seró, I. Preferred Growth Direction by PbS Nanoplatelets Preserves Perovskite Infrared Light Harvesting for Stable, Reproducible, and Efficient Solar Cells. *Advanced Energy Materials* **2020**, *10* (46), 2002422. https://doi.org/10.1002/aenm.202002422.

(40) Bederak, D.; Balazs, D. M.; Sukharevska, N. V.; Shulga, A. G.; Abdu-Aguye, M.; Dirin, D. N.; Kovalenko, M. V.; Loi, M. A. Comparing Halide Ligands in PbS Colloidal Quantum Dots for Field-Effect Transistors and Solar Cells. *ACS Appl. Nano Mater.* **2018**, *1* (12), 6882–6889. https://doi.org/10.1021/acsanm.8b01696.

(41) Dirin, D. N.; Dreyfuss, S.; Bodnarchuk, M. I.; Nedelcu, G.; Papagiorgis, P.; Itskos, G.; Kovalenko, M. V. Lead Halide Perovskites and Other Metal Halide Complexes As Inorganic Capping Ligands for Colloidal Nanocrystals. *J. Am. Chem. Soc.* **2014**, *136* (18), 6550–6553. https://doi.org/10.1021/ja5006288.

(42) Bederak, D.; Sukharevska, N.; Kahmann, S.; Abdu-Aguye, M.; Duim, H.; Dirin, D. N.; Kovalenko, M. V.; Portale, G.; Loi, M. A. On the Colloidal Stability of PbS Quantum Dots Capped with Methylammonium Lead Iodide Ligands. *ACS Appl. Mater. Interfaces* **2020**, *12* (47), 52959–52966. https://doi.org/10.1021/acsami.0c16646.

(43) Balazs, D. M.; Rizkia, N.; Fang, H.-H.; Dirin, D. N.; Momand, J.; Kooi, B. J.; Kovalenko, M. V.; Loi, M. A. Colloidal Quantum Dot Inks for Single-Step-Fabricated Field-Effect Transistors: The Importance of Postdeposition Ligand Removal. *ACS Appl. Mater. Interfaces* **2018**, *10* (6), 5626–5632. https://doi.org/10.1021/acsami.7b16882.

(44) Gong, X.; Yang, Z.; Walters, G.; Comin, R.; Ning, Z.; Beauregard, E.; Adinolfi, V.; Voznyy, O.; Sargent, E. H. Highly Efficient Quantum Dot Near-Infrared Light-Emitting Diodes. *Nature Photonics* **2016**, *10* (4), 253–257. https://doi.org/10.1038/nphoton.2016.11.

(45) Hosokawa, H.; Tamaki, R.; Sawada, T.; Okonogi, A.; Sato, H.; Ogomi, Y.; Hayase, S.; Okada, Y.; Yano, T. Solution-Processed Intermediate-Band Solar Cells with Lead Sulfide Quantum Dots and Lead Halide Perovskites. *Nature Communications* **2019**, *10* (1), 43. https://doi.org/10.1038/s41467-018-07655-3.

(46) Sanchez, R. S.; de la Fuente, M. S.; Suarez, I.; Muñoz-Matutano, G.; Martinez-Pastor, J. P.; Mora-Sero, I. Tunable Light Emission by Exciplex State Formation between Hybrid Halide Perovskite and Core/Shell Quantum Dots: Implications in Advanced LEDs and Photovoltaics. *Science Advances* **2016**, 2 (1), e1501104. https://doi.org/10.1126/sciadv.1501104.

(47) Nakazawa, N.; Zhang, Y.; Liu, F.; Ding, C.; Hori, K.; Toyoda, T.; Yao, Y.; Zhou, Y.; Hayase, S.; Wang, R.; Zou, Z.; Shen, Q. The Interparticle Distance Limit for Multiple Exciton Dissociation in PbS Quantum Dot Solid Films. *Nanoscale Horiz.* **2019**, *4* (2), 445–451. https://doi.org/10.1039/C8NH00341F.

(48) Liu, Y.; Gibbs, M.; Puthussery, J.; Gaik, S.; Ihly, R.; Hillhouse, H. W.; Law, M. Dependence of Carrier Mobility on Nanocrystal Size and Ligand Length in PbSe Nanocrystal Solids. *Nano Lett.* **2010**, *10* (5), 1960–1969. https://doi.org/10.1021/nl101284k.

(49) Klamra, W.; Sibczynski, P.; Moszyński, M.; Kozlov, V. Light Yield Nonproportionality of Doped CeF3scintillators. *Journal of Instrumentation* **2014**, *9* (07), P07013–P07013. https://doi.org/10.1088/1748-0221/9/07/p07013.

(50) W. Mengesha; T. D. Taulbee; B. D. Rooney; J. D. Valentine. Light Yield Nonproportionality of CsI(Tl), CsI(Na), and YAP. *IEEE Transactions on Nuclear Science* **1998**, *45* (3), 456–461. https://doi.org/10.1109/23.682426.

Chapter 8: Future Outlook

8.1 Exploring new 2D perovskite/organic semiconductor pairings

8.1.1 Utilizing other 2D perovskites

At this point, two-dimensional perovskites were successfully implemented as crystalline surfaces with tunable ligand molecule and density. Six perovskites were used in the study, as described in detail in Chapter 2. However, there are many more perovskites with different ligands that have not yet been explored. Perovskites used in our study were terminated with phenyl groups, which provided a non-polar surface termination that matched well with toluene solvent and allowed for continuous thin film fabrication due to good wetting between the perovskite surface and the toluene solvent. However, many ligands have been employed to make two-dimensional perovskites with other terminating groups, such as long chain saturated carbons or fluorinated phenyl groups. Many other perovskite structures that are already reported in literature have not yet been explored in the context of templates for organic semiconductor crystallization. There is an opportunity to tailor the terminating functional group to specific organic semiconductor molecules to maximize interfacial interactions between the perovskites and organic semiconductors.

8.1.2 Enhancing singlet fission timescales in less efficient organic small molecules

The organic semiconductor selected for this study, TIPS-pentacene, was a good candidate for testing 2D perovskites as tunable surfaces for small molecule crystallization because TIPS-pentacene has been shown to adopt many different crystalline structures already. TIPS-pentacene crystal structure has been tuned via deposition parameters, temperature, and thin film thickness. In

this regard, TIPS-pentacene was an ideal molecule to demonstrate proof of concept that 2D perovskites could be substituted for traditional self-assembled monolayers, such as silanes, with the added benefit of surface tunability. With its many structural possibilities, TIPS-pentacene was promising to capture the effects of varying ligand molecule termination and ligand density. However, TIPS-pentacene undergoes exceptionally efficient singlet fission. It would be advantageous to now extend this works to use 2D perovskites to tune the crystal structure of less-efficient small molecule organic semiconductors to enhance singlet fission properties, such as triplet state formation, triplet-triplet separation, and/or triplet diffusion.

8.2 Quantum dot doped lead halide perovskites

8.2.1 Creating a well-matched interface between 3D perovskites and QDs

Functional quantum-dot-doped lead halide perovskite powder scintillators with emission dictated by quantum dot size were fabricated using anti-solvent crystallization. In order for charge carriers to be injected into embedded quantum dots efficiently, a defect-free, well-matched interface between the two materials is required. However, the quality of the interface is affected by many factors such as the quantum dot size, the crystallization method, and the quantum dot surface termination. While functional scintillators were fabricated, the anti-solvent crystallization method may have introduced undesired strain from the quick, kinetic trapping of metastable structures in addition to the lattice mismatch between the lead sulfide lattice and $MAPbBr_3$. First, future works could focus on better controlling the rate of crystallization to enhance seeded-growth of the perovskite matrix on the quantum dot surfaces through means of changing the solvent or evaporation rate during crystallization. Second, future works may focus on using $MAPbI_3$ as the perovskite matrix, which has been shown to have better lattice matching with the lead sulfide

lattice than $MAPbBr_3$. Perhaps a mixed halide perovskite matrix could be used that incorporates both bromine and iodine into the perovskite structure. Third, quantum dots have different ratios of crystal facet termination on its surface based on quantum dot size. Larger quantum dots tend to be more cuboctahedron with more of its surface area being terminated with the (100) crystal facet while smaller quantum dots are more octahedral in shape with more of its surface being terminated with the (111) crystal facets. The (100) crystal facet of lead sulfide is the surface that matches with the perovskite lattice well. Future studies could explore the relationship between the crystal faceting of quantum dots and the efficiency of charge transfer across the quantum-dot-perovskite interface. Optimizing the quantum dot/perovskite interface could enhance charge transfer and lead to brighter quantum-dot-doped perovskite scintillators.

8.2.2 Utilizing QDs with NIR emission within range of silicon PMT detectors

A disadvantage of utilizing quantum dots that emit deep in the NIR (i.e. at wavelengths greater than 1100 nm) is that the scintillator must be coupled to expensive Ge or InGaAs detectors and cannot be coupled to widely-used, popular silicon-based PMT detectors. One avenue to overcome this limitation is to reduce scintillator emission to wavelengths less than 1100 nm, which is the highest wavelength of light that can be absorbed by silicon. Because quantum dot emission is based off of quantum dot core size, embedding smaller quantum dots is a potential solution to this problem. However, for unknown reasons, preliminary results showed a sharp reduction in radioluminescence when embedding quantum dots into $MAPbBr_3$ that were less than 3.8 nm in diameter. Future works could focus on identifying the underlying reason for this observation. It is possible that for smaller quantum dots, the band alignment between the two materials no longer supports electron and hole transfer into the quantum dot, resulting in an unwanted separation of

the charge carriers which is the reason for quenched emission. If this is the case, a perovskite with chlorine composition would provide a wider bandgap and possibly re-establish type I band alignment. Another potential reason for the reduction in radioluminescence is that the (111) crystal facet dominates the quantum dot surface and is preventing lattice matching with the perovskite matrix, as discussed above. In this case, a synthesis would be required such that the (100) crystal facet dominates the surface of smaller quantum dots. This would likely be difficult, but would be beneficial to charge transfer across the interface while allowing for the coupling of quantum-dot-doped perovskite scintillators to silicon-based PMTs detectors.

Le Fin